

DISSERTATION

Compensation of long-range beam-beam interaction at the CERN LHC

ausgeführt zum Zwecke der Erlangung des akademischen Grades eines
Doktors der technischen Naturwissenschaften unter der Leitung von

Univ.Prof. Dipl.-Ing. Dr.techn. H. Aiginger

E141

Atominstitut der Österreichischen Universitäten

eingereicht an der Technischen Universität Wien

Fakultät für Physik

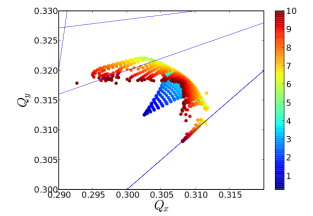
von

Ulrich Dorda

9725240

A-1180 Wien, Czartoryskig. 51

Wien, am 5. Mai 2008



Abstract

Charged particle beams in high energy, high luminosity particle colliders are accompanied by strong and highly nonlinear electromagnetic fields. When two counterrotating beams pass each other these fields give rise to so called “beam-beam interactions” with a wide spectrum of negative consequences for the beam dynamics resulting e.g. in particle loss and emittance blow up.

In the Large Hadron Collider (LHC) such crossings will occur each turn four times “head-on” (once at each interaction point, IP) and fifteen times “long-range” on each side of each IP with a small transverse offset. In order to correct for the resulting perturbations a wire compensator is foreseen.

In the framework of this thesis the tracking code “BBTrack” has been developed and employed to investigate long-range beam-beam interaction and its wire compensation in the CERN LHC (nominal and upgraded). Complementary experimental studies at RHIC at BNL and the CERN SPS were performed allowing experimental insight in the related loss mechanism and benchmarking of the simulation software.

Technical implementations for a pulsed compensator have been studied.

Abriss

Die Teilchenstrahlen in Hochenergiepartikelbeschleunigern sind von einem starken, nichtlinearen elektromagnetischen Feld umgeben. Wann immer zwei Teilchenpakete der gegenläufigen Strahlen einander passieren kommt es daher zu einer als Strahl-Strahl Interaktion bezeichneten elektromagnetischen Wechselwirkung. Diese hat eine Reihe von negativen Konsequenzen fuer die Strahldynamik zur Folge, wie beispielsweise Teilchenverlust oder ein Anwachsen der Emittanz. Im “Large Hadron Collider” (LHC) am CERN werden solche Wechselwirkungen pro Umlauf vier mal frontal (jeweils einmal pro Interaktionspunkt, IP) und 15 mal mit einem kleinen transversalen Abstand auf jeder Seite jedes IPs stattfinden. Im LHC ist für die Korrektur dieser Störungen ein Draht-Kompensator vorgesehen.

Im Zuge dieser Dissertation wurde das Simulationsprogramm “BBTrack” entwickelt und angewandt um diese Strahl-Strahl Interaktion und deren Kompensation im CERN LHC (sowohl in der nominellen als auch in den geplanten weiteren Ausbaustufen) zu untersuchen. Experimente am RHIC (BNL) und am SPS (CERN) wurden durchgeführt um Erkenntnisse ueber die zugehoerigen Teilchenverlustmechanismen zu gewinnen und die Messergebnisse mit Simulationsvorhersagen zu vergleichen.

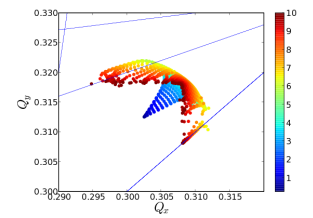
Weiters wurden verschiedene technische Umsetzungen eines gepulsten Kompensators studiert.

Contents

1	Introduction	9
2	Selected topics of accelerator physics	11
2.1	Accelerator descriptions	11
2.1.1	Particles motion	11
2.1.2	Symplecticity	14
2.2	Luminosity	14
2.2.1	Crossing angle	15
2.3	Interaction region	15
2.4	Stability and resonances	16
2.4.1	Intuitive description of Resonances	17
2.4.2	Lie algebra description of Resonances	19
2.4.3	Stability criteria	21
2.5	BBTrack	23
3	Principles of beam-beam interaction and its wire compensation	27
3.1	Kick due to a Gaussian bunch	28
3.2	Head-on beam-beam interaction (HO)	28
3.3	Long-range beam-beam interaction (LRBBI)	30
3.3.1	Linear tune shift, crossing schemes and the PACMAN bunches	33
3.4	Wire compensation of the LRBBI	34
3.4.1	Kick due to a DC-Wire	36
3.4.2	Scaling law	36
4	Super Proton Synchrotron (SPS)	39
4.1	Introduction to the SPS	39
4.2	The SPS BBLRs	39
4.3	General notes on the SPS BBLR experiments	41
4.4	Beam-wire separation scans	43
4.4.1	Experiments at 55GeV	43
4.4.2	Experiments at 37GeV	44
4.5	Wire current scans	45
4.6	Chromaticity scans	46

CONTENTS

4.6.1	Q' scans at $d=6.5\sigma$	47
4.6.2	Current scan at $Q'_y = 33$	49
4.7	1000 turn data	49
5	Relativistic Heavy Ion Collider, RHIC	51
5.1	RHIC	51
5.2	LRBB separation scans at injection energy	52
5.3	LRBB separation scans at 100GeV	54
5.4	BBLR experiments at injection energy	55
5.5	BBLR experiments at top energy	57
5.5.1	MD1	57
5.5.2	MD2	60
5.5.3	MD3	63
5.6	Conclusion	64
6	Large Hadron Collider (LHC)	65
6.1	Nominal LHC	66
6.1.1	Beam-beam interaction of nominal bunches	68
6.1.2	Compensation of LRBBI of nominal bunches	71
6.1.3	Compensation of LRBBI of PACMAN bunches	74
6.2	Upgrade phase 1	75
6.2.1	Low β max	76
6.2.2	Compact	78
6.2.3	Modular	80
6.3	Upgrade phase 2	81
6.3.1	Dipole Zero	81
6.3.2	Large Piwinski Angle (LPA)	83
6.4	Summay of LHC optics	85
7	Pulsed BBLR and related noise issues	87
7.1	Technical challenges	88
7.2	Noise and emittance growth	89
7.3	Pulsed DC-BBLR	90
7.3.1	Noise issues	91
7.4	RF-BBLR	92
7.4.1	Principle and advantages	92
7.4.2	Noise	95
7.4.3	Prototype # 1	96
7.4.4	Prototype # 2	96
7.5	RF characterization of the SPS BBLRS	100
7.6	Measuring phase noise	103



CONTENTS

8	Alternative measures	105
8.1	Electron lens	105
8.2	Crab cavities	106
8.3	Flat beam option	107
9	Summary	109
9.1	Summary	109
9.2	Zusammenfassung	110
9.3	Acknowledgments	111
	Bibliography	112
	Curriculum vitae	115

Introduction

Generally speaking the term “particle accelerator” refers to any kind of device that produces or stores a beam of fast-moving, electrically charged particles. While there are many different kinds of accelerators, this thesis concentrates on high-energy circular accelerators, where ultra-relativistic ($\beta_{rel} \approx 1$) particles are forced by the constant magnetic fields of dipole magnets to move on a closed circular orbit, and, in addition, a sequence of alternating focusing and refocusing quadrupole magnets is used to focus the particle beams.

More specifically this thesis concentrates on an effect specific to high luminosity hadron colliders, where two counterpropagating hadron beams are strongly focused inside a particle-physics detector and brought into collision. The European Organization for Nuclear Research (CERN) in Geneva is presently constructing such a collider - the 27km long Large Hadron Collider (LHC) - which will collide two intense proton beams, each consisting of 2808 bunches, every 25ns at 14 TeV center-of-mass energy. As the two beams share one common beam pipe around the four designed interaction points (IPs), the protons will suffer up to 120 additional so-called long-range or “parasitic” collisions with bunches of the opposing beam (Fig. 1.1). The effect of these long-range collisions limits the dynamic stability of the protons and will likely reduce the beam lifetime.

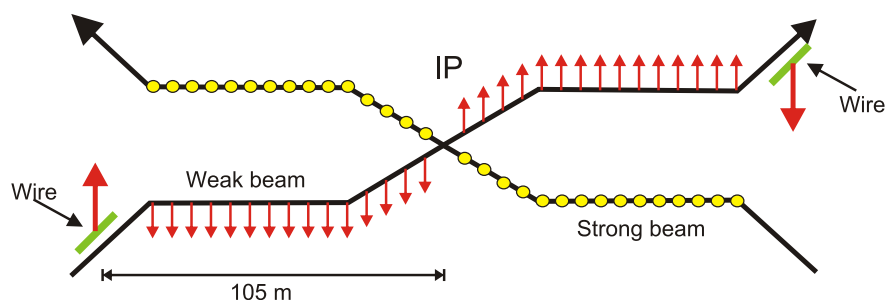


Figure 1.1: In the nominal LHC 16 long-range beam-beam interactions (indicated by the red arrows) will occur at each side of each IP. A wire compensator (green) could cancel their deteriorating effect on the beam stability.

Introduction

This PhD work comprises experimental and theoretical studies on the long-range beam-beam effect and their compensation by wire compensators, aimed at increasing the operating range of the LHC. Such wire compensators are straight, about 2m long wires installed in parallel to the beam inside the beam pipes next to the two high luminosity IPs (CMS & Atlas). The deflecting electromagnetic field of the opposite beam is - within limits - similar to the magnetic field of a current-carrying wire decaying with the inverse transverse distance.

A tracking code “BBTrack” was developed and employed to simulate the impact of long-range beam-beam interaction (LRBBI) on the machine performance and to evaluate the compensation limitations. In the course of my work I also participated actively in ongoing machine studies at the Super Proton Synchrotron (SPS at CERN) and the Relativistic Heavy Ion Collider (RHIC at Brookhaven National Lab, BNL) aimed at gaining a better understanding of the LRBBI itself.

The figures on the top right of each page show the tune footprint in nominal LHC for a compensation current [in Am] identical to the page number and can be watched as a flip-book. Details on this kind of plot can be found in 2.4.1

Layout of this thesis

After a short introduction to accelerator physics concepts related to beam-beam interaction (Ch. 2), a chapter about beam-beam interaction in general follows (Ch. 3). The next two chapters treat experiments performed at the CERN SPS (Ch. 4) and RHIC (Ch. 5), respectively, which were carried out to examine the beam-beam interaction experimentally and to benchmark the simulation code “BBTrack”. In chapter (Ch. 6) the simulated performance of the LHC (nominal as well as phase-1 & -2 upgrade) will be discussed. Chapter (Ch. 7) addresses noise issues and technical possibilities for pulsing the wire compensation at frequencies of a few MHz.

Selected topics of accelerator physics

This chapter starts with a short review of the basics of accelerator physics. In the following the interaction region (IR) design is described with focus on long-range beam-beam related issues. After that instability driving mechanisms and their modelling are introduced. The chapter closes with a short description of the particle tracking code BBTrack, which was developed and employed in the course of this work.

2.1 Accelerator descriptions

The accelerator can be described as a sequence of beam elements (magnets, kickers, beam-position monitors (BPMs), ...) that are placed sequentially along a reference orbit, which describes the path of a charged particle of central design momentum p_0 through idealized magnets. The accompanying tripod of the reference orbit (Fig 2.1) spans a local curvilinear right handed coordinate system (x, y, s) , where the local s -axis is the tangent to the reference orbit. The two other axes are perpendicular to the reference orbit and are labelled x [m] (in the bending plane) and y [m] (perpendicular to the bending plane). The choice of this coordinate system eliminates the effect of the dipoles from the description of motion except for their dispersive part and a weak focussing effect.

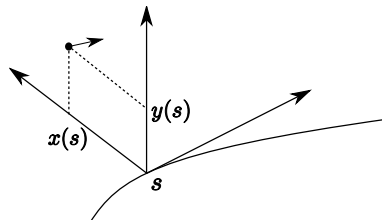


Figure 2.1: The accelerator coordinate system

2.1.1 Particles motion

Under the assumption that a closed orbit exists and the magnet strengths $k(s)$ are periodic (e.g. circular accelerator), the particle motion can be described by a second-order linear differential equation with periodic coefficient

Selected topics of accelerator physics

$k(s)$ - the Hill's equation [1]:

$$x'' - (k - 1/\rho^2)x = \frac{1}{\rho} \frac{\Delta p}{p_0} \quad (2.1)$$

$$y'' + ky = 0 \quad (2.2)$$

where $\rho(s)$ is the local bending radius and $k(s)$ the local focusing strength. Its periodic solution can be written as

$$x(s) = \sqrt{\beta(s)\epsilon} \cdot \cos[\psi(s) + \psi_0] \quad (2.3)$$

$$\psi(s) = \int \frac{ds}{\beta(s)} \quad (2.4)$$

where $\phi(s)$ is the phase advance, $\beta(s)$ is the betatron function and ϵ an invariant of motion at constant energy. The particle motion therefore describes an ellipse in both transverse phase spaces. The emittance is proportional to its area and β characterizes its ellipticity. Often it is beneficial to use normalized coordinates, where the ellipse is transformed into a circle under the boundary condition that the x -value must be scaled only but not mixed with x' (The magnet's kick strength is a function of x only).

$$x \rightarrow \frac{x}{\sigma_x} \quad (2.5)$$

$$x' \rightarrow x' \sqrt{\frac{\beta}{\epsilon}} + x \frac{\alpha_x}{\sigma_x} \quad (2.6)$$

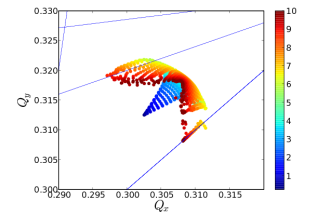
The invariant $J = \epsilon/2$ and phase ψ are commonly referred to as the action angle variables.

Like the solution of any linear differential equation, (2.4) can also be written in matrix form, describing the transport of phase space coordinates (x, x') from one position (β_0, α_0) to another one (β, α) :

$$M(s, s_0) = \begin{pmatrix} \sqrt{\frac{\beta}{\beta_0}}(\cos \Delta\phi + \alpha_0 \sin \Delta\phi) & \sqrt{\beta\beta_0} \sin \Delta\phi \\ \frac{\alpha_0 - \alpha}{\sqrt{\beta\beta_0}} \cos \Delta\phi - \frac{1 + \alpha_0\alpha}{\sqrt{\beta\beta_0}} \sin \Delta\phi & \sqrt{\frac{\beta_0}{\beta}}(\cos \Delta\phi - \alpha \sin \Delta\phi) \end{pmatrix} \quad (2.7)$$

where $\alpha = -\beta'/2$. These transfer matrices are of great use to speed up the tracking of particles through the (almost) linear parts of the machine e.g. the arcs. From (2.7) one can see that a kick in the primed coordinate x' transforms into a change in x after 90 degree phase advance.

Alternatively one can describe an accelerator as a sequence of single elements. These can be defined either as so-called thick lenses of finite length or as so-called thin lenses of zero length with drift spaces (field free regions) in between. In the latter case, the idealized thin element affects the primed coordinates only. In order to improve the accuracy one element



2.1 Accelerator descriptions

is often split into several, cleverly spaced, slices. It is worth noting that in this description a drift is represented by a rather complicated expression. This approach is still reasonably fast and symplectic (see section 2.1.2) by construction.

The quantity

$$Q = \frac{1}{2\pi} \int \frac{ds}{\beta(s)} \quad (2.8)$$

is called the tune. It describes the number of oscillations of a particle in its phase space within one complete revolution around the circular accelerator and will play an important role in the following. We can find the tune Q from the 2×2 1-turn-matrix M_{ring} by computing the eigenvalues λ of M_{ring} : $\lambda = e^{\pm iQ}$.

Once the RF-system has accelerated the bunches to top energy, it is only used to compensate for energy losses and to keep a defined longitudinal bunch shape. As the bunches only fill a fraction of the RF-bucket length a linear approximation of the sinusoidal RF-Voltage is valid allowing a matrix description in the longitudinal phase space: The particles rotate on an ellipse in the $(s-vt)$ - $\delta p/p$ phasespace as well, where $\delta p/p$ denotes the relative momentum deviation from the design momentum.

Deviations of the particle momentum from the design value change the focusing properties of the quadrupoles, causing a coupling of the longitudinal to the transverse plane. One consequence is a tune shift for off-momentum particles referred to as chromaticity. The linear part of the tune shift is called the linear chromaticity Q' :

$$Q' = \left. \frac{\partial Q}{\partial \delta} \right|_{\delta=0} \quad (2.9)$$

It is calculated by:

$$Q' := \frac{1}{4\pi} \oint k(s)\beta(s)ds \quad (2.10)$$

As the particle momentum deviation oscillates with the synchrotron tune, the tune is modulated proportionally. This causes particles to cross resonance lines over and over again, deteriorating their stability.

Furthermore an energy offset results in a modified orbit: $x(s) = x_h(s) + x_i(s)$. The ratio of transverse position shift $x_i(s)$ and the energy offset is called the dispersion D .

$$D(s) = \frac{x_i(s)}{\frac{\Delta p}{p}} \quad (2.11)$$

As a nonvanishing dispersion causes an increased beam size, D must be matched to zero at the IP in order to avoid luminosity loss.

2.1.2 Symplecticity

As any real particle motion obeys Hamilton equations, any description of it, e.g. the transfer matrix, must be consistent with the former. This condition is referred to as symplecticity. Any symplectic map obeys the Liouville theorem, i.e. the phase space volume is conserved as the system evolves. While an arbitrary symplectic map might not be a valid description for a specific part of the accelerator, it always models a physically possible scenario.

For a transfer matrix M the symplecticity condition demands:

$$\tilde{M}SM = \mathbf{S} \text{ where } \mathbf{S} = \begin{pmatrix} 0 & 1 \\ -1 & 0 \end{pmatrix} \quad (2.12)$$

This also applies to nonlinear systems if we identify M with the Jacobian matrix of the map around any particle trajectory, whose elements are defined as $M_{ab} = \partial X_a / \partial (X_0)_b$

In particular in long term tracking studies, where particles are repeatedly iterated through M , symplecticity is of concern. In case the condition is violated, we observe emittance blow-up or shrinkage. During development or utilization of a tracking code, one must keep this in mind e.g. by taking a sufficient number of digits for the transfer matrix elements.

2.2 Luminosity

Apart from the achievable collision energy, the second main characteristics of an accelerator is its luminosity. It allows to compute the occurrence rate dR/dt of interesting events and is given by

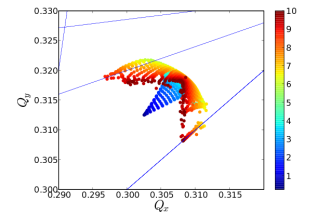
$$\frac{dR}{dt} = L \cdot \sigma_p \quad (2.13)$$

where σ_p is the cross section of the event of interest. Assuming uncorrelated Gaussian profiles in all 6 phase-space dimensions, the luminosity is approximately defined via the relation

$$L = \frac{N_1 N_2 f_{rev} N_b}{4\pi\sigma_x\sigma_y} \quad (2.14)$$

where f_{rev} is the revolution frequency, N_b the number of bunches per beam, σ the transverse spot size at the IP and N_1, N_2 the number of particles in bunch 1 and 2, respectively. For the physics mechanisms to be studied in the LHC an increase in luminosity by a factor of 10 is similar in its discovery potential to doubling the energy.

Furthermore the luminosity should be as constant as possible over time. A very high luminosity at the beginning of the store cannot be used, as



2.3 Interaction region

the detectors need some time to get ready for data taking. As the costly detector electronics must be designed for the highest event rate and might not be able to digest a too high one, luminosity leveling measures might be applied.

Equation (2.14) does not take into account a nonzero crossing angle or the hour-glass effect, which degrade the luminosity. As the choice of the crossing angle is given by long-range beam-beam interaction considerations, this aspect is described in the following.

2.2.1 Crossing angle

In order to increase the luminosity the number of bunches per ring in the nominal LHC was chosen to be $N_b = 2808$ with a 25ns ($\equiv 3.75$ m) spacing. As the separation dipoles are located ≈ 60 m from the IP, this would cause parasitic collisions. To avoid them the two beams collide under an angle θ of $284\mu\text{rad}$ causing a reduction of luminosity

$$L = \frac{N_1 N_2 f_{rev} N_b}{4\pi\sigma_x\sigma_y} \cdot \frac{1}{\underbrace{\sqrt{1 + \left(\frac{\sigma_x \tan \frac{\theta}{2}}{\sigma_s}\right)^2} \sqrt{1 + \left(\frac{\sigma_s \tan \frac{\theta}{2}}{\sigma_x}\right)^2}}_S} \quad (2.15)$$

where S is the so-called luminosity reduction factor. For $\sigma_s \gg \sigma_{x,y}$ S can be approximated by

$$S \approx \frac{1}{\sqrt{1 + \left(\frac{\sigma_s \theta}{2\sigma_x}\right)^2}} \quad (2.16)$$

The term

$$\Theta = \frac{\theta \sigma_z}{2\sigma_x} \quad (2.17)$$

is referred to as Piwinski angle and depends linearly on the half crossing angle and on the ratio of the beam dimensions.

Under the constraint of keeping a certain normalized beam-beam separation, the crossing angle must be increased for decreasing β^* . It may therefore be better to squeeze more strongly in one transverse plane and less in the crossing plane. Such a scheme is called a flat beam option.

2.3 Interaction region

Figure 2.2 shows the optics layout around IP5 in the nominal LHC. Coming from the periodic structure of the arcs, a series of quadrupoles (red bars) perform a parallel-to-point focussing to a small geometric extent but a large divergence at the IP. The black bar indicates the region where the two beams share a common beam pipe and long-range beam-beam interactions can occur. In addition to the focussing, a vanishing dispersion at the IP

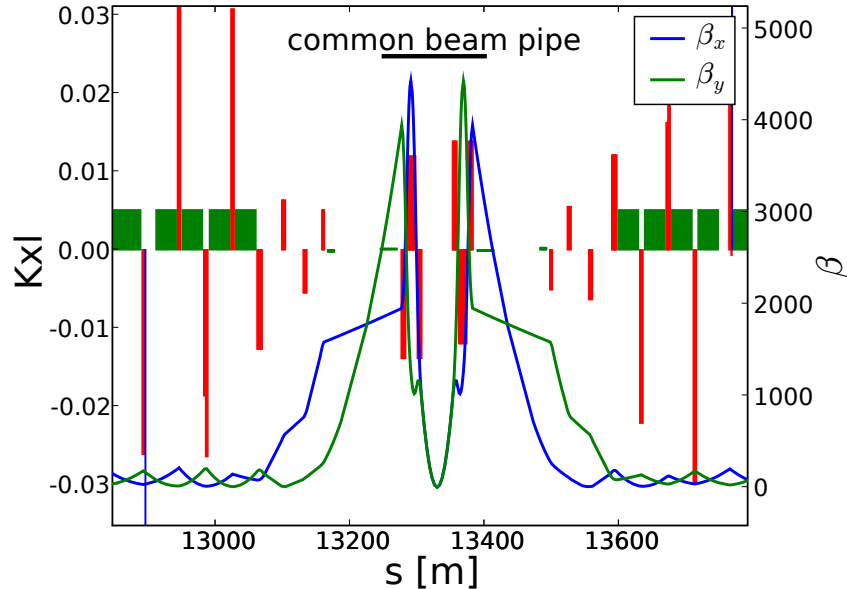


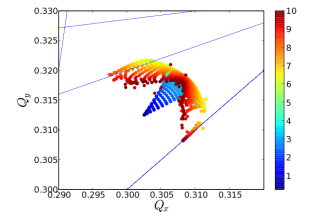
Figure 2.2: Optics layout around IP5 in nominal LHC ($\beta_x^* = \beta_y^* = 0.55$ m). Red bars indicate the location and strength of quadrupoles, green bars those of the dipoles.

must be produced. As the beams are separated horizontally in the arcs, but IP1 features a vertical crossing, an additional orbit crossing bump must be generated. The detectors and the TAS (radiation shield) occupy a distance of about $L^* = 23$ m to both sides from the IP. In this region, no focussing is possible and the beta functions therefore increase quadratically according to $\beta(l) = \beta^* - 2l\alpha + l^2\gamma$, with the minimum value β^* assumed at the IP.

The innermost three quadrupoles are referred to as triplet. It is of great interest to keep the maximal beta function as small as possible as it determines the required triplet aperture. As the beta functions reach very high values in this region, field errors there are the dominating ones at top energy. The effect of the detector's solenoid field is negligible for the particle motion.

2.4 Stability and resonances

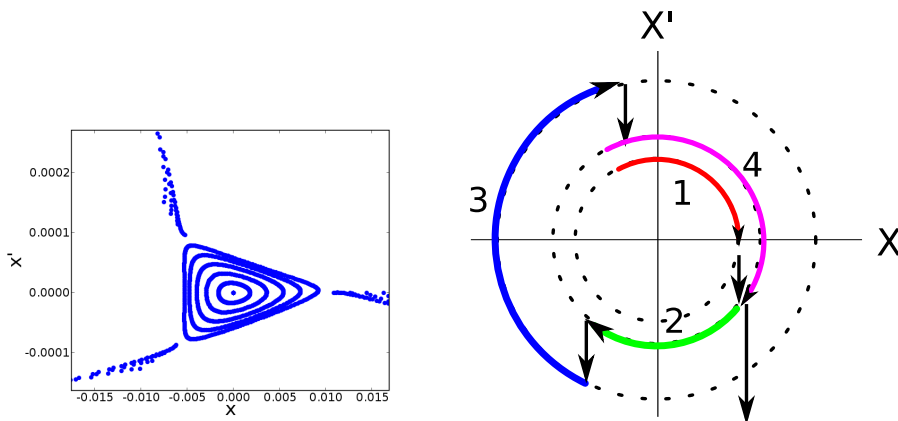
While synchrotron light emission represents a strong damping mechanism in lepton colliders, this is not the case in hadron colliders like LHC. Therefore the latter are more prone to instabilities like the beam-beam interaction.



2.4 Stability and resonances

2.4.1 Intuitive description of Resonances

Any deviation from the perfect guiding field can lead to a resonant excitation of the transverse particle motion and ultimately cause a particle loss. Figure 2.3 illustrates this for the case of a single sextupole in an accelerator with tune close to the third integer. For increasing amplitude the phase space ellipse gets distorted and becomes triangular (Subfigure a). Particles above a certain amplitude are lost along the three separatrices. Subfigure b shows the phase space positions and sextupolar kicks of a particle at tune $Q=1/3$. A similar picture can be drawn for other multipolar orders and resonances.



(a) Motion of particles of varying initial amplitude with base tune close to the third integer in transverse phase space in case of sextupolar fields. For increasing amplitude the tune gets shifted closer towards the $1/3$ resonance causing the ellipses to turn into triangles. Above a certain amplitude particles are lost.

(b) Position of and sextupolar kick on a particle with tune $Q=1/3$ on three consecutive turns illustrating the resonant loss

Figure 2.3: Beam dynamics with sextupolar contributions.

This renders intuitive the resonance condition

$$nQ_x + mQ_y = p \quad (2.18)$$

, where n , m and p are integers, which will be derived in section 2.4.2. Particles with tunes fulfilling this relation may get resonantly excited. If an excited resonance line crosses the region in tune space covered by the core particles, it will cause emittance growth and transport particles to higher amplitudes. It depends on the nonlinearities which of these resonance lines is actually excited. As it will be shown in chapter 3 the long-range beam-beam interaction drives all resonance orders. In order to visualize these resonance conditions and relate the particle tune to them, a so called tune-footprint is drawn. This is a 2D plot where the particle amplitude (x, y) is mapped into

Selected topics of accelerator physics

the tune space (Q_x, Q_y) . Figure 2.4 shows a tune footprint with the design LHC tune. For increasing resonance order the lines become more dense but in general high order ones are also less important.

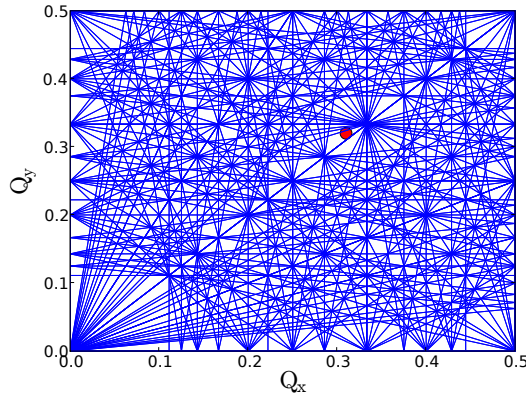


Figure 2.4: Design tune of the nominal LHC in a tune diagram. Resonance lines up to 10th order are drawn.

In a perfect, linear, achromatic machine all particles have the same tune independent of their amplitude. Any accelerator contains multipoles by design (sextupoles, octupoles) or as errors (magnet imperfections, long-range beam-beam interaction), which cause an amplitude dependent tune shift. A general field can be expanded into multipoles as:

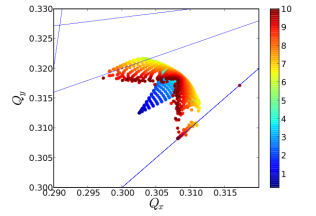
$$B_y + iB_x = B_r \sum_{n=1}^{\infty} (b_n + ia_n) \left(\frac{x + iy}{R_r} \right)^{n-1} \quad (2.19)$$

where R_r is some reference radius. The instantaneous change of position in phase space in polar coordinates (r, θ) of a particle due to a single multipole of n th order is given by:

$$\delta r = \frac{l}{(n-1)!} k_n(s) x^{n-1} \sqrt{\beta_x} \sin(\theta) \quad (2.20)$$

$$\delta \theta = \frac{\frac{l}{(n-1)!} k_n(s) x^{n-1} \sqrt{\beta_x} \cos(\theta)}{r + \Delta r} \quad (2.21)$$

where $k \propto b/(B\rho)$. $\delta\theta$ causes an amplitude-dependent, instantaneous tune change. Individual particles therefore do not stay at constant tunes Q_x, Q_y but are oscillating in tunespace. If there is an excited resonance line within the sampled region, the particle will lock to it and eventually get lost. So even if the tune is not located right on a resonance, it must not be too close to fulfilling the resonance condition. This forbidden tune range next to a



2.4 Stability and resonances

resonance line is referred to as stopband of the resonance and has to be avoided.

The linear tuneshift of a particle performing an oscillation with a given amplitude is calculated by averaging the derivative of the kick over the phases of the particle's oscillation. For a quadrupole with focal length f we find

$$\Delta Q = \frac{1}{4\pi} \frac{\beta^*}{f} \quad (2.22)$$

In a similar way, a nonzero chromaticity causes particles to oscillate in tune space and thus reduces the stability.

2.4.2 Lie algebra description of Resonances

A more accurate derivation of the resonance condition can be obtained using Lie algebra. The one turn map of any accelerator can be described as a composition of successive element maps in the form of nonlinear (lie operators) and linear elements (matrices)

$$M = M_1 e^{h_1} M_2 e^{h_2} \dots e^{h_{N-1}} M_N e^{h_N} M_{N+1} \quad (2.23)$$

where the lie operator “ \cdot ” is defined as $f \cdot g = [f, g]$ with $[\]$ as the Poisson brackets [2] [3]. The exponential operator is defined by its Taylor expansion. Using the similarity relation one can sum all the nonlinear terms at the “front” and combine all the linear elements as

$$M = e^{\bar{M}_1 h_1} e^{\bar{M}_2 h_2} \dots e^{\bar{M}_N h_N} \bar{M}_{N+1} \quad (2.24)$$

where $\bar{M}_n = M_1 M_2 \dots M_n$. Since \bar{M}_{N+1} is a linear, symplectic and stable operator there exists a linear change of coordinates that transforms this operator into a pure rotation $\bar{M}_{N+1} = A R A^{-1}$ where A is the transformation to normalized coordinates and R is a simple rotation. The total one turn map in the new frame will be represented by the same symbol M . Using $g(x_f) = g(e^{f \cdot} x) = e^{f \cdot} g(x)$ this can be written in the form

$$M = e^{\tilde{h}_1} e^{\tilde{h}_2} \dots e^{\tilde{h}_N} R \quad (2.25)$$

where \tilde{h}_n are the functions $h_n(x, y)$ written in terms of the new normalized coordinates. Contracting all the Lie operators (Campbell-Baker-Hausdorff theorem) this simplifies to

$$M = e^{h} R \quad (2.26)$$

Assuming the \tilde{h} are small, h can be approximated by

$$h = \sum_{n=1}^N \tilde{h}_n + \sum_{n,m < n}^N [\tilde{h}_m, \tilde{h}_n] + \dots \quad (2.27)$$

Selected topics of accelerator physics

In the following only the first order terms in 2.27 are kept. Therefore only the phase advance to, and the β function at, the location of the multipole matter, but the sequential order of the elements is neglected.

If one transforms the multipolar Hamiltonian

$$H = H - \frac{q}{p_0} \Re \left[\sum_{n=3}^{\infty} \frac{1}{n} [B_n(s) + iA_n(s)] \cdot (x + iy)^n \right] \quad (2.28)$$

to normalized coordinates and converts to action angle variables, one can find by coefficient comparison the corresponding terms of :

$$h = \sum_{jklm} h_{jklm} (2J_x)^{\frac{j+k}{2}} (2J_y)^{\frac{l+m}{2}} e^{-i[(j-k)(\phi_x + \phi_{x_0}) + (l-m)(\phi_y + \phi_{y_0})]} \quad (2.29)$$

where h_{jklm} are the Hamiltonian coefficients containing the contributions from all the multipoles of order $n = j + k + l + m$, being normal multipoles (B_n) if $l+m$ is an even number, or skew multipoles (A_n) if $l+m$ is an odd number:

$$h_{jklm} = \frac{-q}{p_0} \frac{1}{2^n} \frac{1}{n} \binom{n}{l+m} \binom{j+k}{j} \binom{l+m}{l} \sum_i L_i \beta_{xi}^{\frac{j+k}{2}} \beta_{yi}^{\frac{l+m}{2}} V_{ni} e^{i[(j-k)\phi_{xi} + (l-m)\phi_{yi}]} \quad (2.30)$$

where L_i is the elements length and the perturbation term V_n stands for the multipole coefficients A_n (in case $l+m$ is an odd number) and B_n (in case $l+m$ is an even number) respectively.

In so called “normal-form” coordinates the one turn map is an amplitude dependent rotation represented by an ansatz $E^{H(I)}:R$, where $H(I)$ is a function that depends only on the new action variables and not on the new phases and R is a rotation matrix. Denoting by F the Lie generator that transforms to the normal-form coordinates, the one-turn map in the two frames is related via

$$e^{-:F:} e^{-:h:} e{:RF:} R = E^{H(I)}:R \quad (2.31)$$

Using the Campbell-Baker-Hausdorff up to first order, the two sides are equivalent for

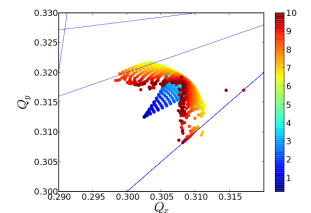
$$(1 - R)F + H = h \quad (2.32)$$

from this we can calculate the generating function F

$$F = \frac{1}{(1 - R)}(h - H) \quad (2.33)$$

Inserting h from eq. (2.29) we obtain:

$$F = \sum_{jklm} f_{jklm} (2I)^{\frac{j+k}{2}} (2I)^{\frac{l+m}{2}} e^{-i[(j-k)(\Psi_x + \Psi_{x_0}) + (l-m)(\Psi_y + \Psi_{y_0})]} \quad (2.34)$$



2.4 Stability and resonances

where the generating function terms f_{jklm} are related to the h_{jklm} of equation (2.29) by the following relation,

$$f_{jklm} = \frac{h_{jklm}}{1 - e^{-i2\pi[(j-k)Q_x + (l-m)Q_y]}} \quad (2.35)$$

If there is a powered multipole field in the machine, the Hamiltonian contains the corresponding h_{jklm} terms. Equation (2.35) illustrates how its effect depends on the particle tune: f_{jklm} diverges if the resonance condition

$$(j - k)Q_x + (l - m)Q_y = p2\pi \quad (2.36)$$

is fulfilled (p being any integer).

2.4.3 Stability criteria

Examining the size and location of the tune footprint allows one to gain an understanding of the causes of beam-particle instabilities but it does not provide quantitative values. The most-straight forward observable in tracking simulations is to examine particle loss (particles exceeding a certain amplitude). As the number of turns that can be tracked is limited to few 100.000s, this criterion turns out not to be sufficiently sensitive. Choosing the Lyapunov exponent (defined later in section 2.4.3) as stability criterion tends to overestimate the impact of the resonances but it still shows the best agreement with experimental data (e.g. Fig. 5.17).

The initial particle distribution must be chosen with care as it alters the simulation results e.g tune footprints. Tracking 6D Gaussian distributions represents the bunch best and especially chromatic effects are modelled accurately but it is rather inefficient, as most particles are located in the stable core, while the border of stability is only coarsely sampled. Therefore alternatively grid-like initial distributions are used.

Lyapunov exponent

The Lyapunov exponent λ describes the rate of divergence of nearby trajectories in phase space. It can be used to detect chaos and to find the dynamical aperture (DA). The Lyapunov exponent is defined as

$$\lambda = \lim_{N \rightarrow \infty} \lim_{d(0) \rightarrow 0} \frac{1}{N} \frac{\log d(N)}{d(0)} \quad (2.37)$$

In the limit of zero initial distance this is equal to the largest eigenvalue of the Nth turn Jacobian matrix, J_{maxEV} :

$$\lambda = \lim_{N \rightarrow \infty} \frac{1}{N} \log J_{maxEV} \quad (2.38)$$

When averaged over long periods of time, the distance d between two trajectories grows linearly in case of regular motion due to amplitude dependent detuning: $d \propto N$. For chaotic motion the distance d between two trajectories grows exponentially. $d \propto e^{\lambda N}$ (Fig. 2.5)

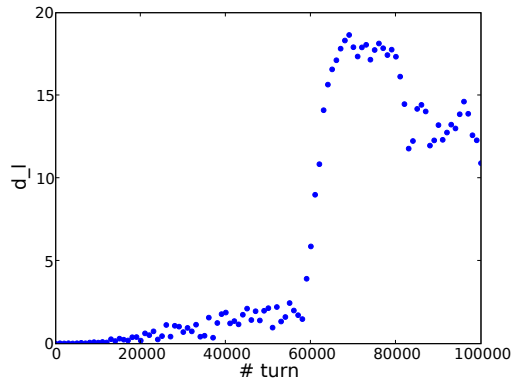


Figure 2.5: simulated distance of two initially close by launched particles. While the smooth increase at low turn numbers indicates regular motion, the sudden increase is taken as a sign of chaos

Frequency maps

Frequency maps allow a very sensitive but rather qualitative evaluation of particle dynamics. Particles are tracked for some few 1000 turns and the tunes at the start and at the end computed with high precision. As the tune should be an invariant for regular motion any change can be taken as an early indicator for chaos [4].

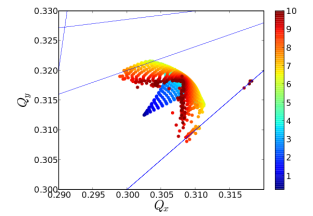
The frequency map needs to be calculated for an on-momentum particle (or a constant off-momentum value with the RF voltage set to zero). Otherwise the synchrotron motion disturbs the picture.

Dynamical aperture (DA)

One can assume that the phase space is divided into two parts: 1) An inner region where almost all particles are stable. As the ever present few chaotic particles are more or less surrounded by a stable region, they cannot escape and thus remain bounded (Nekhoroshev theorem). This domain can be considered stable for infinite times. 2) An outer region where almost all initial conditions give rise to chaotic orbits.

In order to explore the six dimensional phase space, a distribution as shown in Figure 2.6 is launched where each tracked particle has an initial momentum deviation corresponding to 3/4 of the bucket half height (canonical value used for all LHC tracking studies), that is $\delta p = 2.7 \times 10^{-4}$ in the

2.5 BBTrack



nominal LHC at 7TeV.

In order to concentrate the tracking results into one single number, I chose to find the amplitude at which a given percentage of particles, namely 50%, are unstable (indicated by the reddish region in Fig. 2.6). While this may not be accurate in all cases it allows a fair, unbiased comparison between different scenarios.

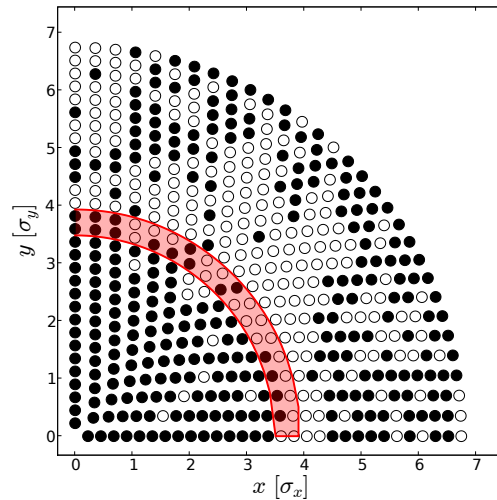


Figure 2.6: Stability of particles in the x-y-plane, black=stable, white=unstable. The reddish region indicates the DA as defined in this thesis.

2.5 BBTrack

In the framework of this thesis the 6D weak-strong tracking code “BBTrack” [5] was developed. In this code, the accelerator structure can either be defined by a sequence of linear transfer matrices and nonlinear elements or by thin lens elements interleaved with drifts of finite length.

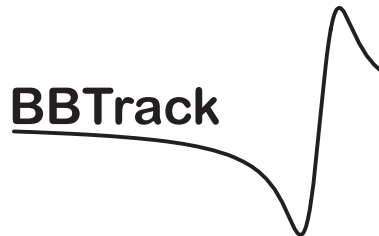


Figure 2.7: The logo of the 6D weak strong tracking code BBTrack

Selected topics of accelerator physics

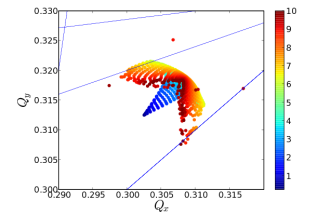
The major steps of the code are:

- Reading-in of the input file defining the accelerator structure and the beam parameters.
- Creation of the initial particle distribution. In case of computation of Lyapunov exponents, for each particle a “twin” particle with slightly shifted coordinates is added. A list of all required actions and their parameters is built (computation of constants, possible contractions of consecutive transfer matrices)
- The particles are tracked in parallel through the accelerator step by step, as this allows implementing elements that require the full bunch distribution to be available, e.g. beam position monitors (BPMs). One processing step can either be a modification of the particle coordinates or another action like the computation of the Lyapunov exponent or a BPM.
- At the beginning of each turn special tasks like a time/turn dependent modification of the sequence can be performed. This allows e.g. adding noise to a wire compensator.
- Finally a basic analysis and the write out of the tracking data are performed.

A collection of postprocessing tools for data analysis and visualization was developed in the Python scripting language. The BBTrack code structure of BBTrack is illustrated in Figure 2.5

There are two types of beam-beam simulations: Weak-strong simulations for the study of incoherent effects (single particle effects) assuming the opposing bunch not to be modified by the interaction (thus referred to as the strong bunch). Strong-strong simulations [6] study the effect of the two beams moving relative to each other (σ and π modes). Almost no accelerator (Tevatron, RHIC, SPS, HERA) has been limited by the strong-strong beam-beam interaction as the associated coherent motion is either Landau damped or can be suppressed by a transverse feedback system. Only in dedicated experiments coherent modes could deliberately be excited. Therefore BBTrack uses a weak-strong approach.

2.5 BBTrack



BBTrack —

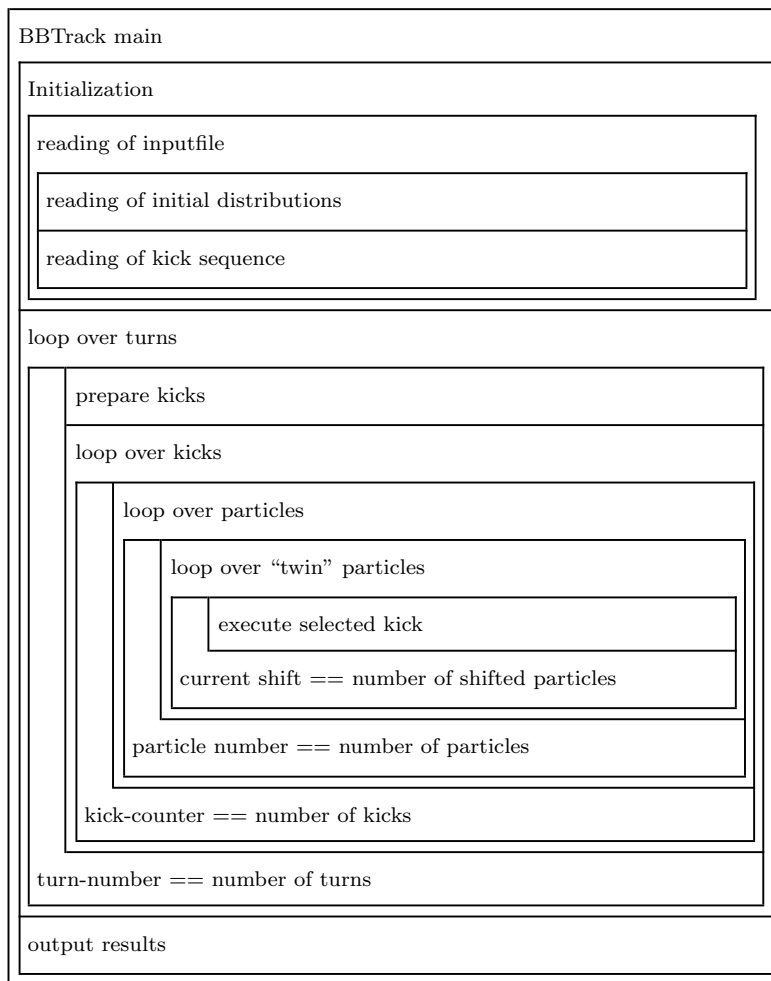


Figure 2.8: The BBTrack code structure

Principles of beam-beam interaction and its wire compensation

The CERN Large Hadron Collider (LHC) is designed for highest luminosity and therefore operates with a large number of bunches at high intensities. Its performance will be limited by the electromagnetic interaction between the charged particle beams and their surroundings causing collective instabilities [7].

One of these effects is the topic of this thesis: The beam-beam interaction. A particle beam is a collection of a large number of charges, which gives rise to a very nonlinear electromagnetic field. At low energies, in the LHC injector chain, the effect on the bunch itself causes emittance blow-up (space charge effect). In LHC at high energy ($\beta \approx 1$, purely transverse fields) the self-effect is negligible but the effect on a passing counterrotating beam becomes an issue. These perturbations are experienced as localized periodic distortions when the two beams pass each other in a common beam pipe next to the IPs. There are two distinct different cases (Fig. 3.1): the head-on beam-beam interaction (HO) and the long-range beam-beam interaction (LRBBI). While the head-on collision is unavoidable, the number and the

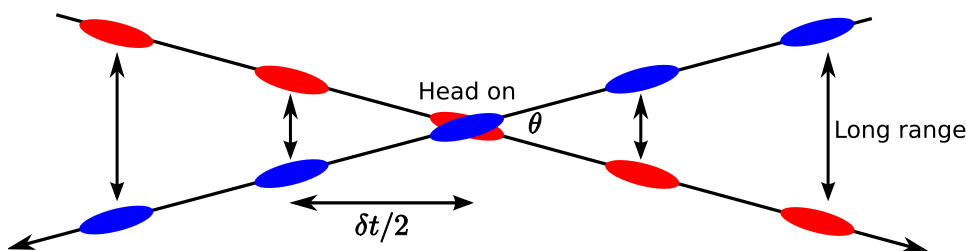


Figure 3.1: Two regions of the beam-beam interaction: Head on and long range. ($\theta_{LHC} \approx 300 \mu rad$). $\delta t / 2$ is half the bunch spacing

strength of long-range interactions is a design parameter (crossing angle θ , bunch spacing, optics layout).

3.1 Kick due to a Gaussian bunch

In case of a LRBBI or low-angle HO the longitudinal extension of the bunch can be neglected. For the transverse charge density we assume a bigaussian distribution (σ_x, σ_y) :

$$\rho(u) = \frac{1}{\sigma_u \sqrt{2\pi}} e^{-\frac{u^2}{2\sigma_u^2}} \quad (3.1)$$

where $u = x, y$. In the bunch reference frame, the resulting transverse electric field is given by (e.g: [8])

$$\begin{pmatrix} E_x \\ E_y \end{pmatrix} = \frac{Ne}{2\epsilon_0 \sqrt{2\pi(\sigma_x^2 - \sigma_y^2)}} \begin{pmatrix} Im \\ Re \end{pmatrix} \left[W \left(\frac{x + iy}{\sqrt{2(\sigma_x^2 - \sigma_y^2)}} \right) - e^{\frac{-x^2}{2\sigma_x^2} + \frac{y^2}{2\sigma_y^2}} W \left(\frac{x \frac{\sigma_y}{\sigma_x} + iy \frac{\sigma_x}{\sigma_y}}{\sqrt{2(\sigma_x^2 - \sigma_y^2)}} \right) \right] \quad (3.2)$$

where $W(z) = e^{-z^2} \operatorname{erfc}(-iz)$, $\operatorname{erfc}(z) = 1 - \operatorname{erf}(z)$ and $\operatorname{erf}(t)$ is the complex error function $\operatorname{erf}(z) = \frac{2}{\sqrt{\pi}} \int_0^z e^{-t^2} dt$ and N is the number of particles per bunch. This must be Lorentz transformed to the accelerator frame, in which the electric and magnetic contribution to the Lorentz force is then identical (Bassetti-Erskine formula [9]), resulting in

$$\begin{pmatrix} F_x \\ F_y \end{pmatrix} = \sqrt{\frac{\pi}{2(\sigma_x^2 - \sigma_y^2)}} \begin{pmatrix} Re \\ Im \end{pmatrix} \left[W \left(\frac{x + iy}{\sqrt{2(\sigma_x^2 - \sigma_y^2)}} \right) - e^{\frac{-x^2}{2\sigma_x^2} - \frac{y^2}{2\sigma_y^2}} W \left(\frac{x \frac{\sigma_y}{\sigma_x} + iy \frac{\sigma_x}{\sigma_y}}{\sqrt{2(\sigma_x^2 - \sigma_y^2)}} \right) \right] \quad (3.3)$$

For round beams $\sigma_x = \sigma_y$ these forces simplify to

$$F_x = -\frac{Ne^2(1 + \beta^2)}{2\pi\epsilon_0} \frac{x}{r^2} \left[1 - e^{-\frac{r^2}{2\sigma^2}} \right] \quad (3.4)$$

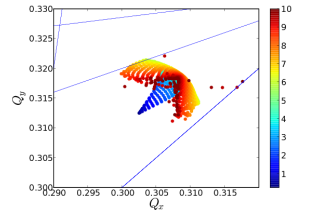
$$F_y = -\frac{Ne^2(1 + \beta^2)}{2\pi\epsilon_0} \frac{y}{r^2} \left[1 - e^{-\frac{r^2}{2\sigma^2}} \right] \quad (3.5)$$

where $r = \sqrt{x^2 + y^2}$. Obviously the beam-beam force causes a nonlinear coupling between the vertical and horizontal plane.

3.2 Head-on beam-beam interaction (HO)

The Head-on beam-beam interaction occurs right at the IP where two counterrotating bunches cross each other with their center transversely aligned. From 3.3 the resulting kick on a particle at position (x, y) can be derived:

$$\Delta x' = \frac{-N_p * r_p}{\gamma} \sqrt{\frac{2\pi}{\sigma_x^2 - \sigma_y^2}} \Im \left[w \left(\frac{x + i * y}{\sqrt{2(\sigma_x^2 - \sigma_y^2)}} \right) - e^{\frac{-x^2}{2\sigma_x^2} - \frac{y^2}{2\sigma_y^2}} \cdot w \left(\frac{x \frac{\sigma_y}{\sigma_x} + iy \frac{\sigma_x}{\sigma_y}}{\sqrt{2(\sigma_x^2 - \sigma_y^2)}} \right) \right] \quad (3.6)$$



3.2 Head-on beam-beam interaction (HO)

$$\Delta y' = \frac{-N_p * r_p}{\gamma} \sqrt{\frac{2\pi}{\sigma_x^2 - \sigma_y^2}} \quad (3.7)$$

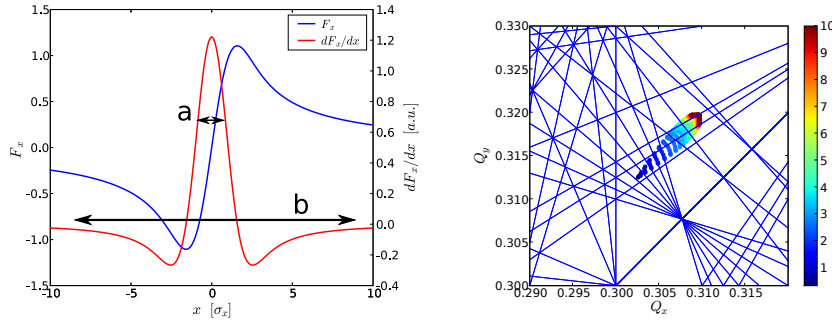
$$\Re \left[w \left(\frac{x + i * y}{\sqrt{2(\sigma_x^2 - \sigma_y^2)}} \right) - e^{\frac{-x^2}{2\sigma_x^2} - \frac{y^2}{2\sigma_y^2}} \cdot w \left(\frac{x \frac{\sigma_y}{\sigma_x} + iy \frac{\sigma_x}{\sigma_y}}{\sqrt{2(\sigma_x^2 - \sigma_y^2)}} \right) \right]$$

or, from (3.5), for the case of round beams:

$$\Delta x' = \frac{2r_p N_p}{\gamma} \frac{x}{r^2} (1 - e^{\frac{-r^2}{2\sigma^2}}) \quad (3.8)$$

$$\Delta y' = \frac{2r_p N_p}{\gamma} \frac{y}{r^2} (1 - e^{\frac{-r^2}{2\sigma^2}}) \quad (3.9)$$

Figure 3.2 a) shows the resulting kick as a function of the particle's transverse offset (blue line). Due to symmetry, zero-amplitude particles do not experience any force. As the kick strength vanishes for higher amplitudes, the head on collision itself cannot cause beam loss. The red line indicates the derivative, which is proportional to the instantaneous tuneshift of a particle. While low amplitude particles sample an almost linear quadrupole-like field (region indicated by a), others sample tune shifts with varying sign. As a parameter indicating the HO strength often the so called beam-beam



(a) Plot of the Head on kick and its derivative \propto tuneshift

(b) Amplitude color encoded Tune footprint due to head on collisions at IP1 and IP5 in nominal LHC. Nominal tune: $Q_x = 0.31$, $Q_y = 0.32$

Figure 3.2: The HO kick and its resulting tune spread

parameter is given. It is the linear tuneshift of a small amplitude particle. For elliptic beams this is

$$\xi_z = \frac{N r_0 \beta_z^*}{2\pi \gamma \sigma_z (\sigma_x + \sigma_y)} \quad (3.10)$$

and for round ones

$$\xi = \frac{N r_0 \beta^*}{4\pi \gamma \sigma^2} \quad (3.11)$$

Principles of beam-beam interaction and its wire compensation

In a colliding beam storage ring the Twiss parameters are affected by the additional quadrupolar focusing of the beam-beam interaction. Like any quadrupole error this 'dynamic beta' effect [10] is enhanced by running near a half-integer or integer resonance and may even enhance the luminosity by providing an additional focusing.

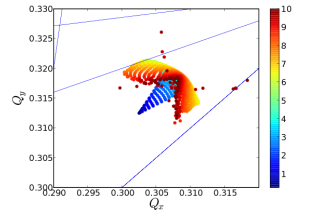
In Figure 3.2 b the tune footprint due to Head-on collision only in nominal LHC is shown. Under the influence of the other beam, the tune of the core of the bunch is moved from $Q_x = 0.31$, $Q_y = 0.32$ down wards, while higher-amplitude particles are hardly affected. Whereas most other perturbations affect the higher amplitude particles the HO changes the dynamics of the majority of particles at the bunch center. It is the main cause of tune spread in the core of the bunch and thus the main cause of filamentation.

In case of large crossing angles and/or longitudinally flat bunches the longitudinal extent of the bunches might become an issue. Particles located in the transverse bunch center in the head or tail of the bunch now collide with the center of the opposite beam with a small offset. To model this situation correctly it might become necessary to split the bunch into several longitudinal slices and collide the single slices with each other [11]. This can be taken into account as proposed in [12] which describes a transformation into a transversely Lorentz-boosted frame. The synchro-betatron resonance excited by the finite crossing angle is assumed to be weak in the accelerators considered ([13], [12])

3.3 Long-range beam-beam interaction (LRBBI)

If the bunches do not collide head-on but with a transverse offset large compared with the beam size, the electromagnetic interaction is referred to as long-range beam-beam interaction. These collisions can be distributed all around the accelerator like in the Tevatron, where the two opposite charged beams move along helices in one common beam pipe all around the ring, or localized like in LHC, where the beams share a common beam pipe only for a limited distance around the particle physics detectors.

The kick due to a single LRBBI can be derived from equation (3.7) by a simple coordinate transformation $u \rightarrow u - L$ where u is x or y and L is the beam-beam separation. This transformation results in a nonzero kick for zero amplitude particles and thus in a changed closed orbit. In a collider this dipole component is corrected for by static orbit correctors. In simulations one subtracts this dipole terms right away and uses for the kick due to a LR



3.3 Long-range beam-beam interaction (LRBBI)

encounter (vertical crossing)

$$\Delta x' = \frac{-N_p * r_p}{\gamma} \sqrt{\frac{2\pi}{\sigma_x^2 - \sigma_y^2}} \quad (3.12)$$

$$\Im \left[w\left(\frac{(x-L) + i * y}{\sqrt{2(\sigma_x^2 - \sigma_y^2)}}\right) - e^{-\frac{(x-L)^2}{2\sigma_x^2} - \frac{y^2}{2\sigma_y^2}} \cdot w\left(\frac{(x-L)\frac{\sigma_y}{\sigma_x} + iy\frac{\sigma_x}{\sigma_y}}{\sqrt{2(\sigma_x^2 - \sigma_y^2)}}\right) \right. \\ \left. - \underbrace{\left(w\left(\frac{-L}{\sqrt{2(\sigma_x^2 - \sigma_y^2)}}\right) - e^{-\frac{-L^2}{2\sigma_x^2}} \cdot w\left(\frac{-L\frac{\sigma_y}{\sigma_x}}{\sqrt{2(\sigma_x^2 - \sigma_y^2)}}\right) \right)}_{\text{constant term subtracted}} \right] \quad (3.13)$$

$$\Delta y' = \frac{-N_p * r_p}{\gamma} \sqrt{\frac{2\pi}{\sigma_x^2 - \sigma_y^2}} \quad (3.14)$$

$$\Re \left[w\left(\frac{(x-L) + i * y}{\sqrt{2(\sigma_x^2 - \sigma_y^2)}}\right) - e^{-\frac{(x-L)^2}{2\sigma_x^2} - \frac{y^2}{2\sigma_y^2}} \cdot w\left(\frac{(x-L)\frac{\sigma_y}{\sigma_x} + iy\frac{\sigma_x}{\sigma_y}}{\sqrt{2(\sigma_x^2 - \sigma_y^2)}}\right) \right. \\ \left. - \underbrace{\left(w\left(\frac{L}{\sqrt{2(\sigma_x^2 - \sigma_y^2)}}\right) - e^{-\frac{-L^2}{2\sigma_x^2}} \cdot w\left(\frac{L\frac{\sigma_y}{\sigma_x}}{\sqrt{2(\sigma_x^2 - \sigma_y^2)}}\right) \right)}_{\text{constant term subtracted}} \right] \quad (3.15)$$

where $w(z) = e^{-z^2} \text{Erfc}(-iz)$ In case of a round beam the kick is given by (here horizontal crossing):

$$\Delta x' = K \left[\frac{x-L}{r^2} (1 - e^{-\frac{-r^2}{2\sigma^2}}) + \underbrace{\frac{1}{L} (1 - e^{-\frac{-L^2}{2\sigma^2}})}_{\text{constant term subtracted}} \right] \quad (3.16)$$

$$\Delta y' = K \frac{y}{r^2} (1 - e^{-\frac{-r^2}{2\sigma^2}}) \quad (3.17)$$

where $K = -2r_p \frac{N}{\gamma}$ for identical charge signs, $r = \sqrt{(x-L)^2 + (y^2)}$ and L is the beam-beam separation in x-direction (center-center). It can be seen that

- the LRBBI strength is a function of the normalized beam-beam separation,
- for small amplitude particles the LRBBI acts like a quadrupole while for higher amplitudes it becomes increasingly nonlinear.
- it drives all orders of resonances.

Principles of beam-beam interaction and its wire compensation

Another interesting, and rather worrisome, aspect is that, in combination with HO, the long-range collisions “fold” the footprint (Fig 3.3), i.e., they give rise to a change of direction of detuning with amplitude. This folding is potentially destabilizing, as resonance islands in this amplitude region can be large.

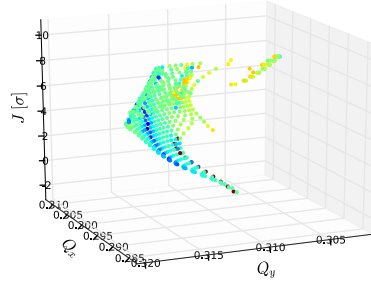


Figure 3.3: Tune-diffusion color encoded tune footprint in the Q_x - Q_y - J -plane. (J is the particles initial amplitude). This case of the upgrade phase 1 optics “low β max” illustrates the folding of the tune footprint due to the combined effect of LRBI and HOI

From the IP to the first quadrupole, the normalized beam-beam separation is constant and fixed by the crossing angle and β^* . The triplet affects the two beams and thus each of its quadrupoles focuses one beam in one plane while defocusing the other beam in the other plane, respectively. Considering both sides of the IP the overall average normalized beam-beam separation remains the same also further out.

Figure 3.4 shows the tunespread due to LRBBIs only in the nominal LHC. While low amplitude particles are hardly affected, larger ones cover a large tune area and lock to resonances

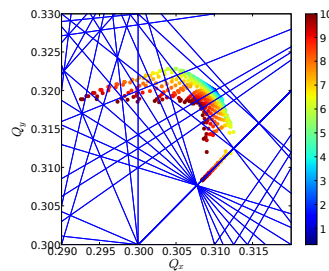
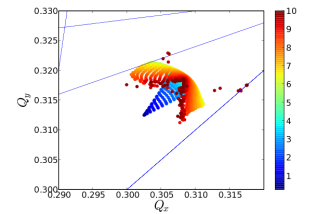


Figure 3.4: Tune footprint due to LRBBIs only in the nominal LHC for a grid like initial distribution in the $x - y$ -plane. The color encodes the particle’s initial transverse amplitude. (IP1 & 5 only)

The long-range beam-beam interaction influences the triplet design in the following regards:



3.3 Long-range beam-beam interaction (LRBBI)

- Finite crossing angle.
- The length of the common beam-pipe must be minimized. Therefore sometimes a so called “dipole first option” is studied where the two beams are separated transversely before being focused.
- Beam position monitors (BPM) cannot be positioned at the locations of the LRBBI as the standart monitors cannot distinguish the two beams. As BPMs have to be placed in between magnets, this is an additional constraint.

3.3.1 Linear tune shift, crossing schemes and the PACMAN bunches

In case of horizontal crossing the linear tune shift due to LRBBI is given by (d in units of σ)

$$\Delta Q_x = \frac{2N_p r_p}{4\pi\gamma\epsilon_x d_n^2} \left(1 - e^{-\frac{d^2}{2}} (1 + d^2)\right) \quad (3.18)$$

$$\Delta Q_y = \frac{-2N_p r_p}{4\pi\gamma\epsilon_y d^2} (1 - e^{-\frac{d^2}{2}}) \quad (3.19)$$

The linear tuneshift of the LRBBI is therefore

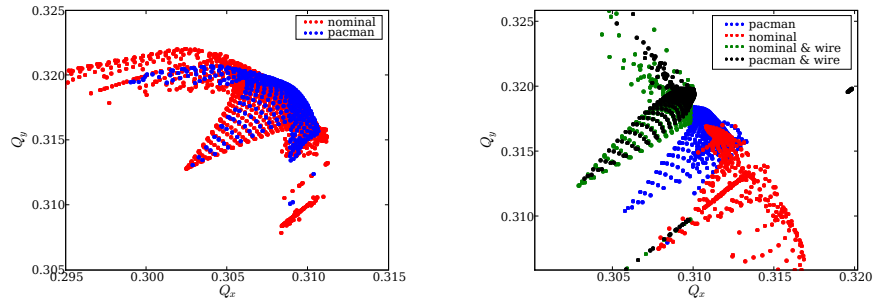
- negative in the crossing plane,
- positive in the orthogonal plane.

Choosing alternate crossing planes (HV) in the two low β^* experiments of the LHC therefore provides a cancellation of the linear long-range beam-beam tune shift. The price to pay is a nonzero vertical dispersion. Figure 3.5 shows the tune footprint in case of HH and HV crossing. An HH-crossing scheme causes an asymmetric footprint that is shifted with respect to the design working point [14] [15]. If all bunches would experience exactly the same LRBBI effect and thus experience the same linear tune shift, the latter could be corrected for.

In the nominal design, the LHC ring is filled with bunch trains consisting of 72 bunches with 25ns spacing. Two trains are interleaved with gaps of varying length. Therefore bunches at the end of a bunch train, so called PACMAN bunches, experience a reduced number of LRBBI. The extreme bunches at the very end of the train experience no LRBBI at all at one side of the IP. As a result these bunches have different orbits and tunes. Figure 3.5a shows that the tune footprint of the extreme PACMAN bunch does not overlap with the one of a nominal bunch in case of an HH-crossing scheme.

A 45 degree hybrid crossing scheme could also minimize the spread, but it would introduce a strong coupling. In order to achieve perfect cancellation and not to be sensible to bunch-to-bunch variations, the same bunches

should interact at the two main IPs. Therefore IP1 and 5 must be geometrically located exactly opposite each other [16].



(a) HV-crossing schemes feature a tuneshift cancellation. The tune footprint of the PACMAN bunch is slightly smaller and centered on the footprint of nominal bunches.

(b) In case of a HH-crossing the tune footprints of nominal and PACMAN bunches are asymmetric and do not overlap. A individually adjusted wire compensator can correct for this

Figure 3.5: Tune footprints for nominal and PACMAN bunches in case of HV and HH crossing

3.4 Wire compensation of the LRBBI

The beam-beam interaction has limited the performance of almost all past and present storage-ring collides and a number of attempts to overcome this limitation have been made [17]. Around 1970 an attempt of 4-beam collisions with charge neutralization at the Orsay DCI [18] failed as small offsets in the centroid positions of the oppositely charged beams were amplified exponentially [19]. In 1975, head-on collisions with a high beam-beam tune shift were simulated in the CERN ISR by two vertically separated copper bars carrying 1000-A of electric current [20]. The ISR experiment showed that resonances of order 10 or higher contributed to the proton beam-beam limit. Since 2001 the Tevatron Electron Lens (TEL) is operational at FNAL. It collides selected antiproton bunches with an electron beam of appropriate shape and strength to compensate for the effect of the head-on antiproton-proton collisions at other locations of the ring [21]. Still so far the TEL is not used in normal physics operation for this purpose.

As the deflecting electromagnetic field of the opposite beam is - within limits - similar to the magnetic field of a current-carrying wire (see section 3.4.1 and Fig. 3.6) one can attempt to compensate for the LRBBI by such a wire. Such a wire compensator is commonly referred to as “BBLR” and was proposed for the LHC in [22].

Figure 3.7 sketches the compensation principle in the nominal LHC. A BBLR is located at each side of each high-luminosity IP to compensate for

3.4 Wire compensation of the LRBBI

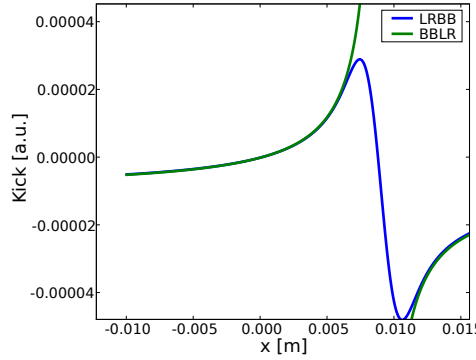
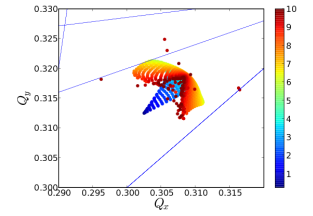


Figure 3.6: A comparison of the LRBBI kick to the BBLR one promises a good compensation efficiency.

the effect of the 15 nearby LRBBIs. The BBLR must be mounted at a

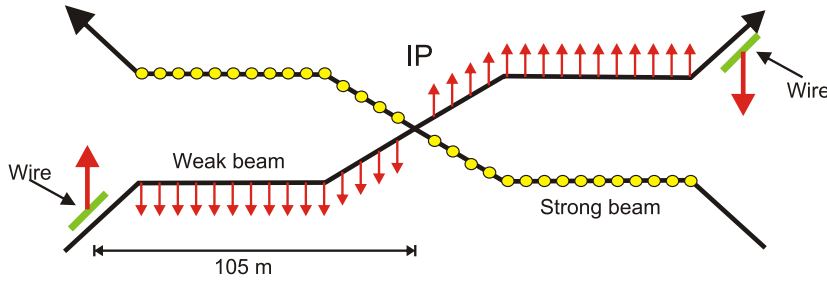


Figure 3.7: Wire compensation in the LHC. The arrows indicate the direction and strength of the LRBB and the wire, respectively.

position fulfilling the following requirements:

- Equal β functions in both transverse planes (or ratio identical to the average of the LRBBIs on the same side of the IP.)
- The β function must be reasonably large to accommodate a wire compensator with finite extensions.
- The average phase advance between the LRBB-IPs and the wire must be minimized
- The wire must be positioned in the shadow of the secondary collimators instead of at the optimal distance (9.5σ). Therefore a wire compensator can only be used to compensate LRBB encounter with transverse separation $L > 7\sigma$. To compensate closer encounters one could think of using an electron lens. As the primary collimators will be positioned at 6σ , the BBLR can safely be put to 9.5σ .

Principles of beam-beam interaction and its wire compensation

- The two beams must be in separate beam-pipes.
- The wire should be positioned at a normalized distance identical to the average beam-beam separation.

3.4.1 Kick due to a DC-Wire

The kick on a particle due to a magnetic field B is given by ($u = \begin{pmatrix} x \\ y \end{pmatrix}$):

$$\Delta u' = \frac{\Delta p_u}{p_s} = \frac{1}{p_s} \left(q \int (v_z \times B) dt \right) \quad (3.20)$$

Like it was argued in the case of the LRBB kick, one can assume that the linear contribution is compensated by other means. Therefore the constant part is to be subtracted and a zero amplitude particle is not affected. One finally finds for a wire with an offset x_w and y_w :

$$\Delta x' = K \left[\frac{x - x_w}{r^2} + \underbrace{\frac{x_w}{d^2}}_{\text{constant term subtraction}} \right] \quad (3.21)$$

$$\Delta y' = K \left[\frac{y - y_w}{r^2} + \underbrace{\frac{y_w}{d^2}}_{\text{constant term subtraction}} \right] \quad (3.22)$$

where $K = -\text{sign}(q) \frac{\mu_0 I}{2\pi B_d \rho}$ and $d = \sqrt{x_w^2 + y_w^2}$. As the BBLR strength depends on the product wire current I times the wire length l , it will from now on be given in units of Am.

The linear tuneshift due to a wire can be computed from its Taylor expansion (wire positioned at d_x, d_y)

$$\Delta Q_x = \frac{K \beta_x}{4\pi} \left[\frac{-2dx_w^2}{(dx_w^2 + dy_w^2)^2} + \frac{1}{dx_w^2 + dy_w^2} \right] \quad (3.23)$$

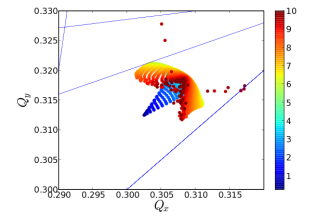
$$\Delta Q_y = \frac{K \beta_y}{4\pi} \left[\frac{-2dy_w^2}{(dx_w^2 + dy_w^2)^2} + \frac{1}{dx_w^2 + dy_w^2} \right] \quad (3.24)$$

The perfect compensation current can be computed by equating the LRBBI kick to the BBLR kick:

$$I_{ideal} = c_0 N n_{par} / l_w \quad (3.25)$$

3.4.2 Scaling law

It is interesting to see how the effect of the BBLR (or LRBBI) scales with energy, separation and emittance. F. Zimmermann suggests in [23] to demand the linear tuneshift to be identical in two comparable cases. Using



3.4 Wire compensation of the LRBB1

$d = n \cdot \sigma$ and $\sigma = \sqrt{\beta\epsilon}$, the tunes shift is given by

$$\Delta Q = \frac{1}{4\pi} \frac{\beta}{f} \quad (3.26)$$

$$\propto \frac{I r_p \beta}{B \rho n^2 \beta \epsilon} \quad (3.27)$$

$$\propto \frac{I}{B \rho n^2 \epsilon} \quad (3.28)$$

It turns out that a change of energy should be transparent as $B\rho$ is directly proportional to γ while ϵ is inversely proportional to it. In case of identical normalized emittances, which is approximately the case for RHIC and LHC, the DA should therefore be the same.

This idea can be expanded to higher order terms yielding the same scaling law.

Super Proton Synchrotron

(SPS)

4.1 Introduction to the SPS

The Super Proton Synchrotron (SPS) at CERN was officially commissioned in 1976 and has served since to accelerate antiprotons, electrons, positrons and heavy ions. From 1981 to 1984 it operated as a proton-antiproton collider (Sp \bar{p} S). It was used as injector for the Large Electron-Positron Collider (LEP) and will continue to do so for the Large Hadron Collider (LHC). In addition, it will continue to provide beams to the fixed target research programs like “CERN Neutrino to Gran Sasso (CNGS)”. The main machine parameters for proton operation are summarized in Table 4.1.

Variable	Value
Machine circumference [m]	6911.5
Momentum at injection [GeV/c]	26
Momentum at extraction [GeV/c]	450
Lattice type	FODO
Tunes (LHC Beam, Q_H/Q_V)	26.185 / 26.13
RF Frequency [MHz]	200.0
RF Voltage at injection [MV]	0.6-0.8
RF Voltage at extraction [MV]	3.0
Synchrotron tune	3E-3
Trans. emittance [μm]	< 10 / < 7.5
Long. emittance [eVs]	0.2
Geom. aperture at 26GeV [σ]	4

Table 4.1: SPS parameters for proton operation in 2007 with LHC type beams

4.2 The SPS BBLRs

In 2002 a wire compensator (BBLR1) with a single wire was installed in the CERN SPS at $s \approx 5170\text{m}$ (Fig 4.1b) as part of a campaign aimed at gaining a

Super Proton Synchrotron (SPS)

better understanding of the long-range beam-beam interaction. By altering its current, it can be used to simulate the effect of a varying number of long-range interactions. As the wire is mounted at a fixed vertical distance from the beam pipe center (beam pipe center - wire center $d=20.27\text{mm}$), the closed orbit of the beam has to be shifted vertically to study the effect of different beam-wire separations. Due to the limited available strength of the adjacent orbit correctors the applied 1, 3 or 5 π orbit bumps can provide sufficient offset only in experiments at up to 55 GeV.

In 2004 a second BBLR2 was installed 3 degree in phase advance downstream allowing compensation experiments. This second BBLR is equipped with 3 wires at 0, 45 and 90 degree in azimuth (Fig 4.1a) to allow crossing plane studies. The whole tank can be shifted vertically to allow a change in the beam - wire edge distance d from 19mm to 24mm without changing d at the BBLR1.

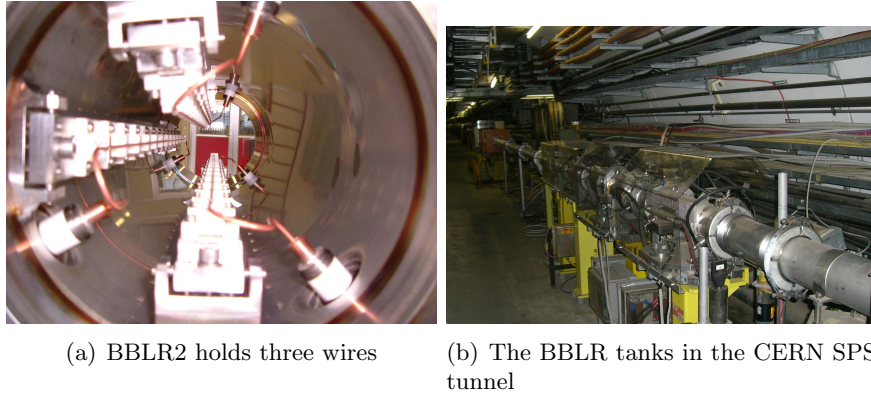
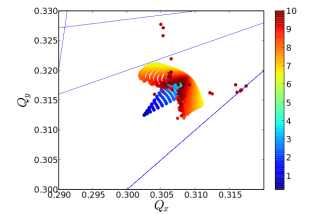


Figure 4.1: The CERN SPS BBLRs

The BBLR wires are made out of hollow copper rods with an outer diameter of 2.54 mm and an inner one of 1.54 mm and they can be powered with a DC current of up to 267A. To dissipate the resulting heat in the wires (760 W), the BBLRs must continuously be water cooled (flow: 0.4l/min). Each BBLR consists of two separate tanks which are powered in series adding up to an effective length of 1.2m. In order to reduce the current ripple of the power converters huge conductivities are installed in series.

The optics functions at the wire locations are listed in Table 4.2



4.3 General notes on the SPS BBLR experiments

Name	BBLR1	BBLR2
l [m]	1.2	1.2
s [m]	5168.6	5170.8
β_x [m]	47.6	54.1
β_y [m]	50.8	44.6
α_x	-1.4	-1.52
α_y	1.46	1.32
D_x	-0.58	-0.61
D_y	0	0

Table 4.2: Optics parameter at the BBLR.

4.3 General notes on the SPS BBLR experiments

While the unperturbed beam lifetime in the SPS is only a few minutes at injection energy (26 GeV), it increases to about one hour at 55 GeV. Figure 4.2 a) shows the timing of a typical SPS machine-development (MD) cycle with BBLR studies: The beam is injected at 26 GeV where it is stored for a few seconds before it is accelerated to a higher energy plateau at 37 GeV. Some MD cycles have another plateau at 55 GeV. The experiments have to be performed within the few seconds available at constant energy.

The initial beam intensity and emittance are given by the injector chain and vary from shot to shot (and thus also the normalized beam-wire separation). An example of the resulting spread in the measurement curves is shown in Figure 4.2 b) where each color corresponds to one identical machine setting. Usually several shots are taken for each setting and the results averaged. During some of the early MDs it was attempted to blow up the emittance in a controlled manner with help of the transverse feedback system or with an injection mismatch, but since this turned out to be very time consuming and inefficient it was not pursued any further.

Taking SPS BBLR MD results and drawing conclusions for the LHC from them, is a delicate issue for several reasons:

- One has to scale the beam energy and beam emittance from the SPS to the LHC.
- While the measurement interval in the SPS is some few seconds, the LHC beam lifetime is expected to be several hours.
- The BBLR imitates the LRBBIs well in the $1/r$ regime of the beam-beam force, but not for small values of the beam-wire separation d as it is being considered for certain LHC upgrade scenarios.
- While the BBLR acts at a single betatron phase, the LRBBIs at the LHC are spread over various phase advances.

Super Proton Synchrotron (SPS)

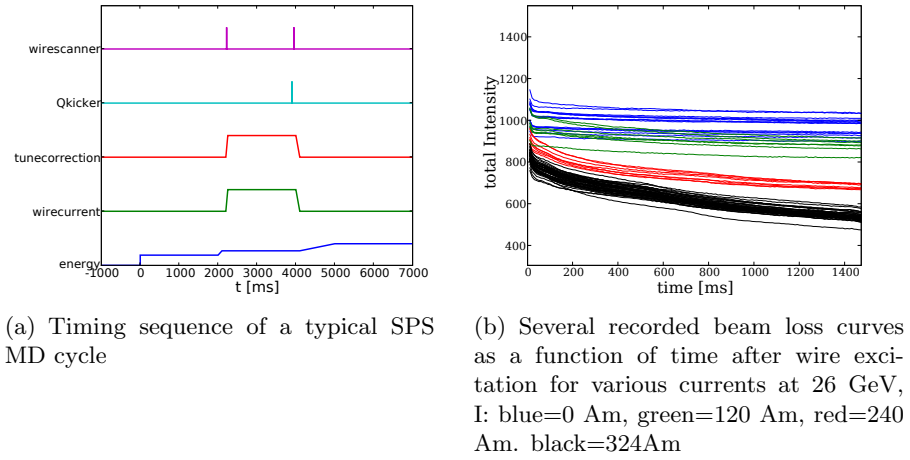
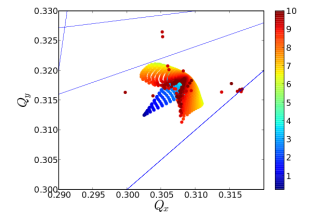


Figure 4.2: Typical MD cycles: Timing and beam intensities

- As there are no HO collisions in the SPS there is no HO-tune related tune spread and no tune footprint folding.

At the beginning of each MD a lot of time was invested to set up the machine properly: Choosing the desired tune, adjusting the beam orbit with special attention to the BBLR locations, setting the chromaticity to a reasonably small value and correcting coupling. Usually it was attempted to operate at the LHC tunes (0.31/0.32), but due to the excited wire in some Mds the tunes approached each other and coupling could not be corrected anymore. Therefore $Q_H = 0.31$, $Q_V = 0.28$ was used instead. The tune was measured continuously with help of the BBQ, and also at the end of each measurement cycle by a tune kick. This allowed cross-checking of the beam-wire distance by comparing with the linear tune change computed according to 3.23.

After injection-filamentation the 4σ -longitudinal emittance ($= 4\pi\sigma_t\sigma_E$) is typically $A_{4\sigma} = 0.4eVs$. For an RF gap voltage of 2 MV at 26 GeV this results in $\delta p/p = 0.4/(4\pi \cdot 0.7 \cdot 26) = 1.7 \times 10^{-3}$. The bunch length at the consecutive 37 GeV plateau depends slightly on the 26 GeV RF-settings. In case of a non-adiabatic RV-voltage jump, particles escape longitudinally from the RF-bucket and are lost during the following acceleration. This effect may cause a smaller longitudinal emittance of the remaining bunch. For $V_{gap} = 2MV$ at 26 GeV and $V_{gap} = 2.6MV$ at 37 GeV, the longitudinal rms bunch length is approximately constant $l_{1\sigma} = 0.7ns$, and the momentum spread is $\delta p/p = 0.4/(4\pi \cdot 0.7 \cdot 26) = 1.2 \times 10^{-3}$.

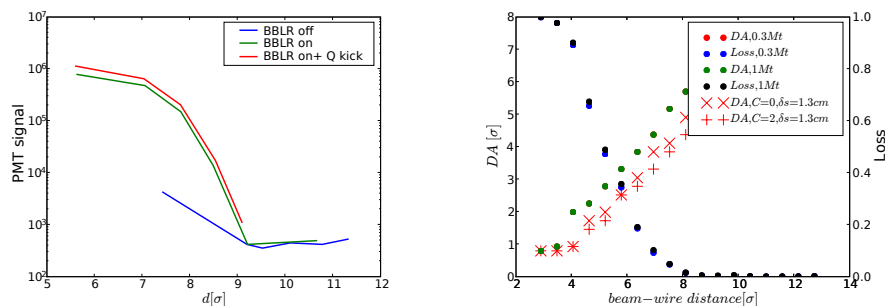


4.4 Beam-wire separation scans

4.4 Beam-wire separation scans

4.4.1 Experiments at 55GeV

The first important results from the SPS BBLRs were obtained from a beam-wire distance scan at 55GeV at a current equivalent to the integrated effect of 60 nominal LHC long-range beam-beam interactions ($300Am = 4 \cdot 15 \cdot 5Am$) at a normalized emittance of $\epsilon = 3.5E - 6$ in 2002 . The tunes were $Q_x = 0.1862$ and $Q_y = 0.1383$. The result is shown in Figure 4.3: A simple



(a) Beam loss signal during a beam-wire distance scan with a wire current equivalent to the integrated effect of 60 long-range beam-beam collisions in the nominal LHC.

(b) Corresponding simulation results from tracking over 300.000 and 1.000.000 turns. The DA is computed from a grid-like distribution in the x-y plane, the loss from a 6D Gaussian one.

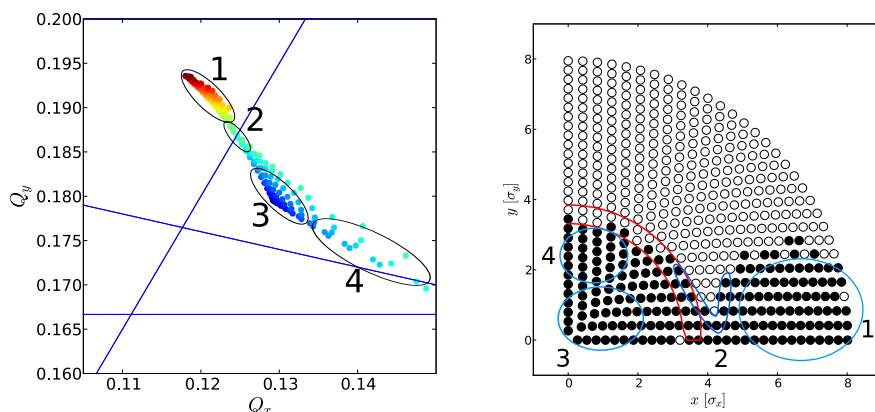
Figure 4.3: Beam-wire distance scan at 55 GeV at $I = 320Am$. The finite lifetime in case of no active BBLR corresponds to the natural limited SPS beam life time. The simulations reproduce the onset of beam loss within the measurement precision.

extrapolation of the experimental results to the LHC yields a beam lifetime of about 20 hours. An error of 10% on the estimate of the actual beam-wire separation changes this conclusion: The lifetime is reduced to 4 hours, which is both unacceptable for physics and defined as the warning level for the quench prevention (quench level roughly corresponds to a lifetime of 1 hour). Figure 4.3 b) presents the pertinent simulations that reproduce the onset of beam loss from a 6D Gaussian bunch within the measurement precision at $\approx 8.5\sigma$. Furthermore it can be seen that it is sufficient to track for 300.000 turns as no significant increase of beam loss is found for a higher number of turns.

Figure 4.4 shows details for a beam-wire separation of $d_y = 10mm = 5.8\sigma$. The DA is indicated by the red framed region in the stability plot. The numbered areas indicate corresponding regions in both plots. Stable low amplitude particles belong to region 3. Region 4 contains particles launched with an initial high y- but low x-amplitude. They are tune shifted

Super Proton Synchrotron (SPS)

and get lost once the 6th order resonance ($m=0, n=6, p=1$ or $m=1, n=5, p=1$) is reached. Region 2 comprises particles with intermediate x and y amplitude that surround the area of the stability drop. Their x and y tune shift add up in a way that they are shifted into the third order ($m=3, n=-2, p=0$) resonance. Finally region 1 are particles with high x amplitude that are tune shifted above the latter resonance. Although these particles are marked as stable here, they will not contribute to the DA as they are separated from the beam core by an unstable region.



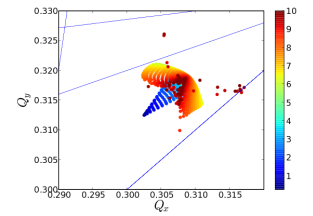
(a) Amplitude color encoded tune footprint of a grid like initial distribution $0-8\sigma$ (stable particles only).

(b) Stability plot. The red framed region indicates the DA.

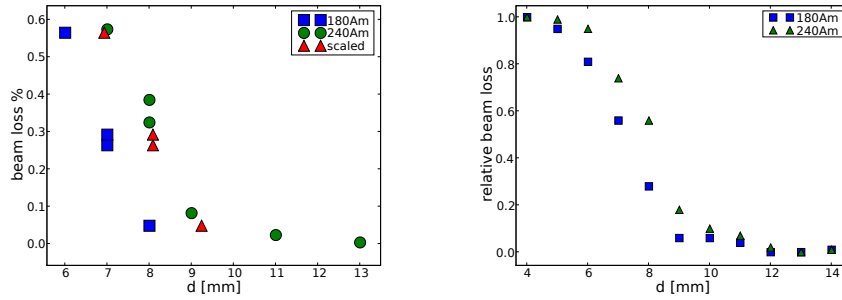
Figure 4.4: Details of the simulation results for $d_y = 10\text{mm} = 5.8\sigma$. Corresponding regions in both plots are marked by numbers.

4.4.2 Experiments at 37GeV

The data obtained in two beam-wire separation scans at 180 and 240Am at $Q=(0.31/0.28)$ is shown in Figure 4.5. For a wire strength of 240Am first small losses are observed at $12\text{mm} \approx 8\sigma$, but a steeper increase occurs at $9.5\text{mm} \approx 6.3\sigma$. This two stage increase is reproduced in the simulations, but the beam loss in the 180Am case is slightly higher than in the experiment, where the onset of beam-loss is found at $d \approx 8.5\text{mm} \approx 5.6\sigma$. Now the scaling law for different BBLR currents at identical energy can be tested. In this case it demands the ratio I/d^2 to be constant: For 240Am we find $240/6.3^2 = 6$ which is close to the value at 180Am: $180/5.6^2 = 5.74$. An attempt to scale the result from these 37 GeV experiments in energy to the 55 GeV one described in the previous section fails.



4.5 Wire current scans



(a) Experimental data and data points scaled scaled from 150A*1.2m to 200A*1.2m

(b) The simulated beam loss reproduces the two stage increase of beam loss at 240Am but overestimates the one at 180Am slightly

Figure 4.5: Experimental and simulated beam-wire distance scan at 37GeV, $\sigma_{y,BBLR} \approx 1.5mm$

4.5 Wire current scans

In order to obtain experimental hints of the viability of the LHC phase-2 upgrade optics proposal “dipole zero” (D0, 6.3.1), current scans at various beam-wire separations were performed at 26, 37 and 55 GeV. The three

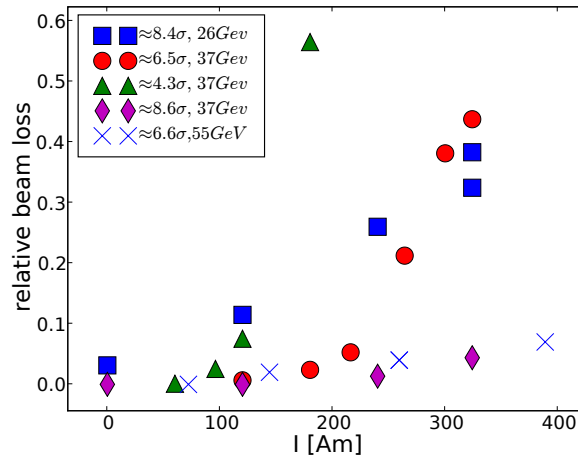


Figure 4.6: Beam loss as a function of the wire current for various beam-wire separations at 26 and 37 GeV at $Q_H = 0.31$, $Q_V = 0.28$

37 GeV data sets shown in Fig. 4.6 are consistent within themselves and match with the data in the d -scan of Fig. 4.5: The 180Am case shows first beam loss at 6.6σ in both experiments. At a large normalized distance, the

Super Proton Synchrotron (SPS)

26 GeV data set shows significantly higher losses already for low current values, which must probably be accredited to the inherently unstable beam at injection energy. The 55 GeV data matches its 37 GeV pendant at low current values but does not show the steep increase at 200 Am.

Figure 4.7 shows the corresponding simulation results and confirms the previous thoughts: While the 37 GeV data is reproduced reasonably well, the 26 GeV data curve is not. The delayed experimental onset of beam loss in the $d=4.3\sigma$ case is not reproduced in the experiment probably because some potentially unstable regions in the 6D phase space were cleaned during the preceding 26 GeV plateau. The 6.5σ data in 37 and 55 GeV show the same differences in both, simulation and experiment. While the 55 GeV data shows a smooth slow increase of beam loss, the 37 GeV data shows distinct slope changes.

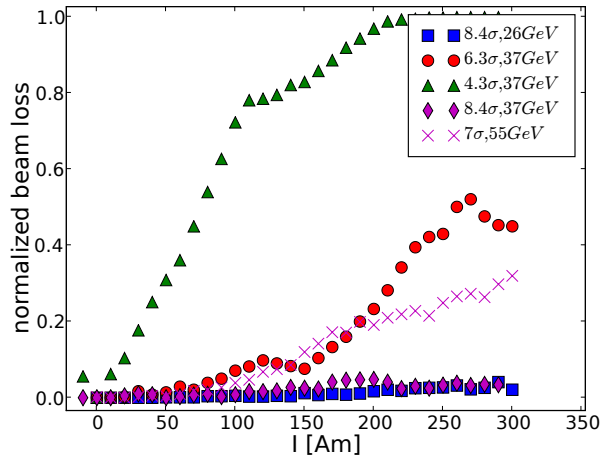
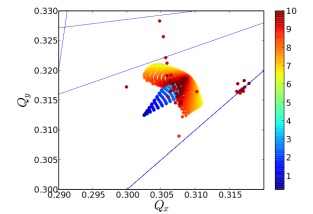


Figure 4.7: Simulation of the Beam loss as a function of the wire current for various beam-wire separations at 26 and 37 GeV at $Q_H = 0.31$, $Q_V = 0.28$

According to the scaling law of equation (3.4.2) two setups should be identical if the ratio $A = I/d^2$ is the same. In order to test this, I choose the data points of the 37 GeV data causing about 7% and 45% beam loss. The data points are obtained by a hands-on interpolation. Table 4.3 shows a reasonable good agreement in this case. Given the implausibly high beam losses in the 26 GeV case, it is not much of a surprise that an attempt to verify the energy scaling fails.

4.6 Chromaticity scans

All experiments mentioned above were performed at low chromaticity $Q' \approx 1$. For nonzero chromaticity, the particles experience a periodic momentum



4.6 Chromaticity scans

I [A]	d [mm]	I/d^3	I [A]	d [mm]	I/d^3
100	6	2.7	270	9	3.33
200	9	2.57	141	6	3.9
300	11	2.479			beam loss: $\approx 45\%$
beam loss: $\approx 7\%$					

Table 4.3: Test of the scaling law for experimental data at 37GeV, showing a relatively good agreement of the different cases.

dependent tune variation which causes the particle tunes to oscillate periodically in the $Q_x - Q_y$ plane and thereby to cross resonance lines over and over again. In case of no wire excitation, only the usual lattice resonances are driven and thus, most resonance lines are harmless, but they become excited once the wire is turned on.

4.6.1 Q' scans at $d=6.5\sigma$

This chromatic effect was studied for a wire excitation of 180Am at $d \approx 9mm \approx 6.5\sigma$. Figure 4.8 shows the experimentally obtained beam-loss data during the vertical and horizontal chromaticity scan at 37 GeV. Obviously the available measurement interval is not long enough to reach a saturation of the beam loss. While in the horizontal case the situation shows an exponential decay and heads for a stable level at a reduced beam current, the vertical beam loss does not show any sign of leveling.

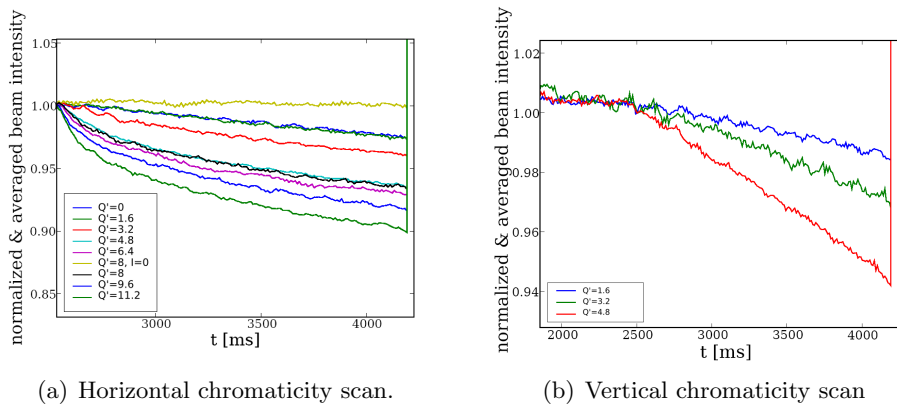


Figure 4.8: Vertical and horizontal chromaticity scan at 37GeV. Data normalized to $t = 2500$ ms.

The available data gives a first hint of the strength of the effect. This is summarized in Figure 4.6.1 together with the results of a vertical chromaticity scan at 55 GeV. In order to confirm that the beam loss is due to a combined effect of the wire and chromaticity, one case of high chromaticity, $Q'=12$, but without BBLR excitation was measured as well. Simulations of

Super Proton Synchrotron (SPS)

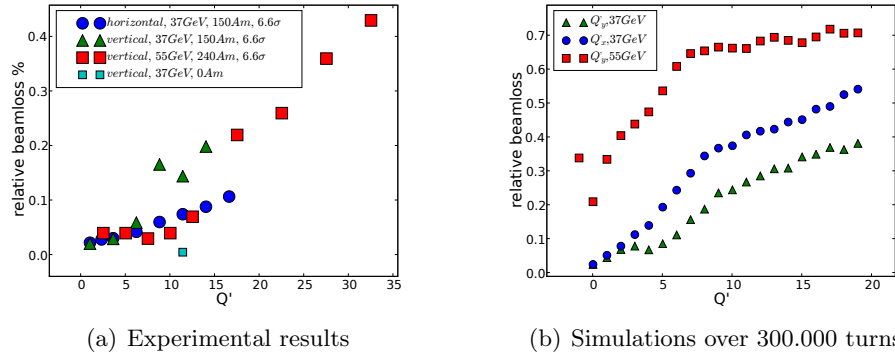


Figure 4.9: Beam loss as a function of the chromaticity for $d=6.6\sigma$ at 37 and 55 GeV for varying wire excitations. Simulations reproduce a strong impact of the chromaticity. A quantitative comparison is not easily possible as the beam loss did not saturate in the few seconds of the measurement interval

6D Gaussian bunches (Fig. 4.6.1b) reproduce a strong chromaticity dependence and also the identical slope of loss versus chromaticity at low Q' values in both transverse planes for 37 GeV. For higher Q' values the simulations cannot be compared as the experimental decay was not completed and time limited simulations are known to be unreliable. The simulations reproduce the smooth increase for the horizontal chromaticity and the peculiar shape for the vertical one at 37 GeV. Again consistent with the experimental wire current scan at 55 GeV (Fig.4.6) the simulations shows again a higher beam loss.

Figure 4.10 details the longitudinal dependence of the particle losses. The logarithmic color encoding in these plots indicates the turn number at which the onset of chaotic behavior is detected. While for $Q'=0$ in subfigure a there is almost no s -dependence and all the particles just above the stability border turn chaotic at similar turn numbers, this is not the case for $Q' > 0$ and the chromaticity induced beam loss can take significantly longer. The particles with a large longitudinal offset in Figure 4.10 are located in the next RF bucket and are again more stable. While the total tune shift of these particles is large, the tune oscillation amplitude is small. This fact illustrates well that it is the tune oscillation which matters and not the total tune shift.

4.7 1000 turn data

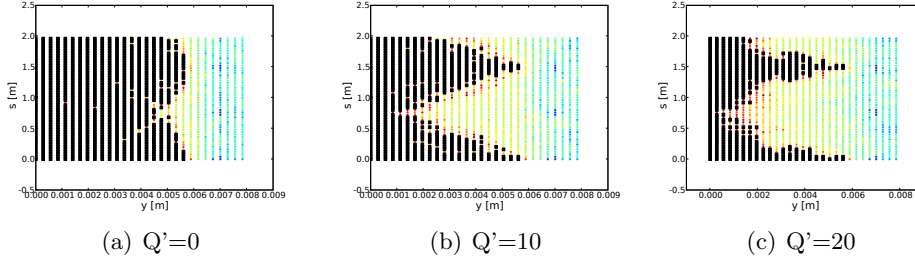
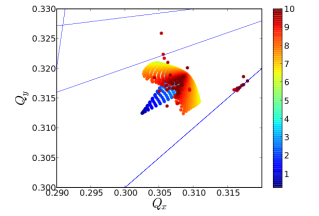


Figure 4.10: Stable (black squares) and unstable (colored dots) particles in the y - s -plane for various chromaticities for $x=0$. The color logarithmically encodes the turn number at which the onset of chaos is detected. Particles with $s > 0.7$ m are in the next RF bucket. An amplitude of $s = 0.2$ m corresponds to $dp/p = 0.00115$ after a quarter synchrotron period.

4.6.2 Current scan at $Q'_y = 33$

Finally a current scan was performed for high vertical chromaticity $Q'_y = 33$ at 55 GeV with a beam-wire separation of $d=6.6\sigma$. Figure 4.11 a compares the result with a scan at low chromaticity. The simulations in subfigure b also reveal the strong chromaticity dependence. The absolute beam loss is higher in the simulations, which might again be attributed to the limited data taking interval.

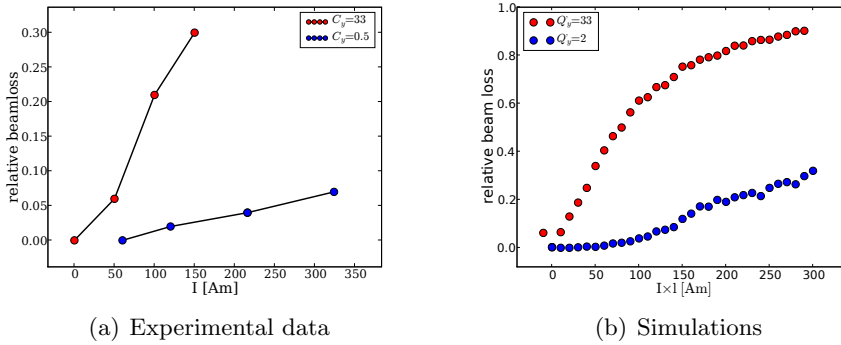


Figure 4.11: BBLR current scan at $Q'_y = 33$

4.7 1000 turn data

During the 37 GeV measurements 1000 turn BPM data was stored. This data was analyzed and compared with tracking data (single element thin lens). Figure 4.12 shows a reasonably good agreement for the phase advances between two adjacent BPMs between experiment and simulation. The same

Super Proton Synchrotron (SPS)

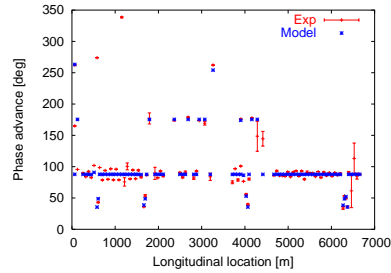
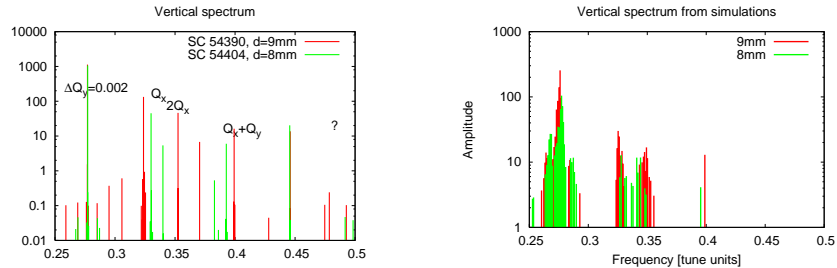


Figure 4.12: Comparison of the phase advances between two adjacent BPMs in experiment and simulation with a wire excitation of 240Am.

data can also be used to find the spectral components. Figure 4.13 shows the experimentally observed vertical spectral lines (a) and the simulated ones (b) for 8 and 9mm beam-wire separation at 240Am. For the simulation a 6D Gaussian bunch horizontally offset by 1mm was tracked over 1000 turns. The main lines appear at the vertical tune (including the linear tune shift due to the wire), and several coupling resonances are also identified among the additional peaks.



(a) Vertical spectrum from experimental data

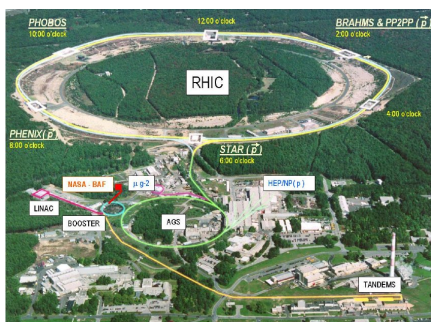
(b) Vertical spectrum from tracking data

Figure 4.13: Spectral components found in experimental and simulated 1000 turn BPM data.

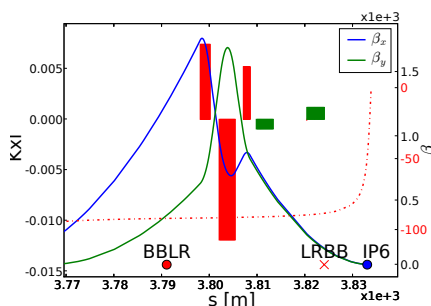
Relativistic Heavy Ion Collider, RHIC

5.1 RHIC

The Relativistic Heavy Ion Collider (RHIC, Fig 5.1a) at the Brookhaven National Laboratory (BNL) in Upton, New York, started operation in 2000. It consists of two independent, superconducting rings (arbitrarily called as "blue" and "yellow") with a 3834m circumference where polarized protons are stored at up to 250GeV or ions at up to 100GeV. The interaction points are enumerated by clock positions, with the BBLR installed close to 6 o'clock (Fig. 5.1b).



(a) The Accelerator chain at BNL



(b) Optics layout: quadrupoles (red bars), dipoles (green bars), β functions and horizontal phaseadvance from the IP (slashed dotted line), position of the BBLR. The LRBB occurs either at the IP or shifted by 9m

Figure 5.1: The RHIC accelerator at BNL and the position of the RHIC BBLR

RHIC is a more suitable testbed for LHC as it is a collider and therefore provides a much longer beam lifetime and better beam instrumentation (as compared to the SPS). The price to pay is an even lower availability and the more difficult operation. Each injection cycle takes a longer time and beam operation must be performed even more carefully such as not to

quench the superconducting magnets.

Due to the chosen bunch spacing and the IP design, the two beams do not experience any long-range beam-beam interactions (LRBBI) in nominal RHIC operations. In order to create a single LRBBI for the machine studies the beams were deliberately separated vertically at IP6 (no collisions in the other IPs) with varying beam-beam separation. In order to have a low phaseadvance to the BBLR-compensator the long-range collision point was sometimes shifted to $s \approx 10m$. There is one wire-compensator installed in each of the two rings 41m from IP6 (Fig 5.1b). Each one is 2.5 m long and can be powered with up to 50A. In order to avoid any current ripple on the BBLR, huge capacitors are placed in series, which limit the current rise-time. The noise was measured to be less than $\Delta I/I < 1.7E - 4$ at 50A.



Figure 5.2: The two RHIC BBLRs before installation

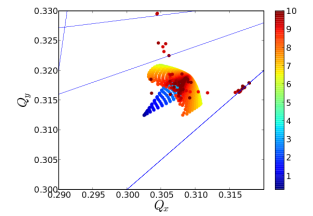
During this thesis I had the chance to actively participate in the BBLR related experiments by proposing the experiments, performing data analysis and personally attending one MD in 2007.

5.2 LRBB separation scans at injection energy

The following section deals with the LRBB experiments performed on 28 April 2005 (RHIC fillnumbers: 06981 and following) with protons at injection energy (24GeV) for a typical bunch intensity of $1 - 2 \times 10^{11}$ p/bunch. At injection energy the β functions at the IP are $\beta_x = \beta_y \approx 10$ m, the ones at the shifted interaction point ($s \approx 10$ m) are $\beta_x = \beta_y \approx 20$ m. For a 1σ -emittance of $\epsilon_x = 1.2E - 7$ mm.mrad and $\epsilon_y = 8.3E - 8$ mm.mrad, the vertical 1 sigma beam size at the IP is therefore 0.9mm. The energy spread is typically 2.9×10^{-3} . The tunes were chosen for the two beams close, mirror symmetric to the (1,-1) resonance. All experiments (e.g. Fig 5.3) show an onset of beamloss at a vertical beam-wire separation $d \approx 7\sigma$. The beam-beam separation is changed by stepwise shifting the closed orbit off one of the beams. After each distance step an exponentially decaying beam loss is observed. The shifted beam tends show more beam loss compared to the remaining one.

The simulations (Fig. 5.4 a) reproduce the behavior qualitatively within the experimental measurement imprecision if the experimental chromaticity of $Q' \approx 2$ is included. Simulations with zero chromaticity show a significantly reduced beam loss. The onset of beam loss is found at 6σ .

Figure 5.5 shows a comparison of the $Q'=0$ to the $Q'=2$ case for particles



5.2 LRBB separation scans at injection energy

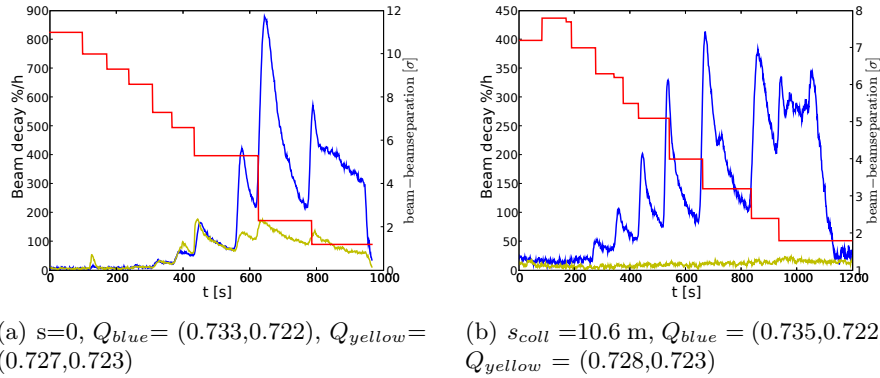


Figure 5.3: Example of an experimentally observed beam loss rate, wire current and normalized beam-wire distance as a function of time. As the effect of the LRBB scales with sigma, there is no difference between the two cases of LRBBI at $s=0$ m and $s=10$ m. The onset of beam loss is found at $d \approx 7\sigma$.

initially launched along the 45° line in the x-y-plane. Particles that do not show chaotic behavior for $Q'=0$ within the tracked 300.000 turns but a higher tune diffusion, turn chaotic for $Q'=2$.

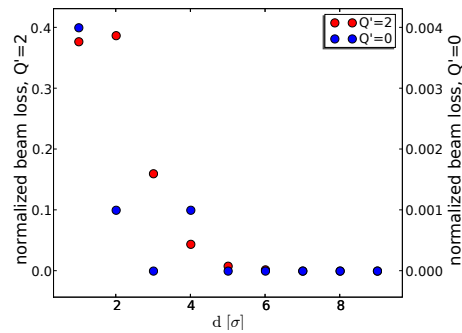
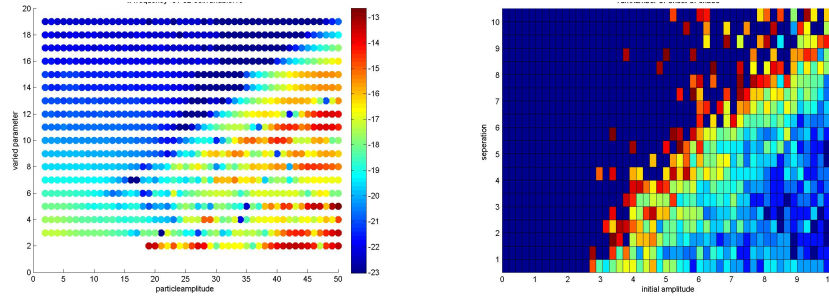


Figure 5.4: Simulations find a stability that depends crucially on the chromaticity. The $Q'=2$ corresponds to the experimental situation and reproduces the onset of beam-loss within the experimental measurement precision.

Relativistic Heavy Ion Collider, RHIC

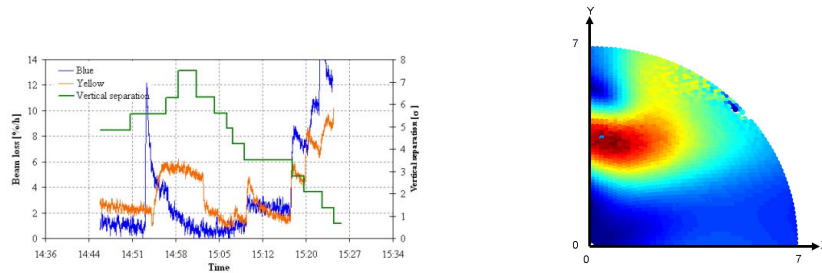


(a) The color encodes the tune diffusion (TD) logarithmically in case of $Q'=0$. (b) The color encodes the turn number of the onset of chaos for $Q'=2$ (dark blue=stable)

Figure 5.5: Comparison of the simulated dynamics of particles along the 45° line in the x-y plane for $Q'=0$ and $Q'=2$ for various beam-beam separations.

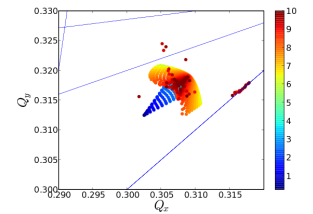
5.3 LRBB separation scans at 100GeV

In 2006 beam-beam separation scans of a single LRBB encounter with beam intensities of the order of 1.5×10^{11} p/bunch were performed with protons at 100GeV. In some experiments beam loss was observed at $d \approx 3\sigma$ (Fig. 5.6a), while in other ones no significant beam loss at beam-beam was found at all. Simulations show an increased Lyapunov exponent (Fig. 5.6) but no chaotic motion is detected.



(a) One of the experiments showing a beam loss at a low beam-beam separation. $Q_{\text{blue}} = (0.69, 0.70)$ $Q_{\text{yellow}} = (0.71, 0.69)$. (RHIC Fill #07807, 03.05.2006) (b) Simulations do not find any beam loss but only regular but increased Lyapunov exponent (color encoded). Here the case of a vertical beam beam separation of 3σ is shown.

Figure 5.6: Effect of a single LRBB encounter at 100GeV in experiment and simulation

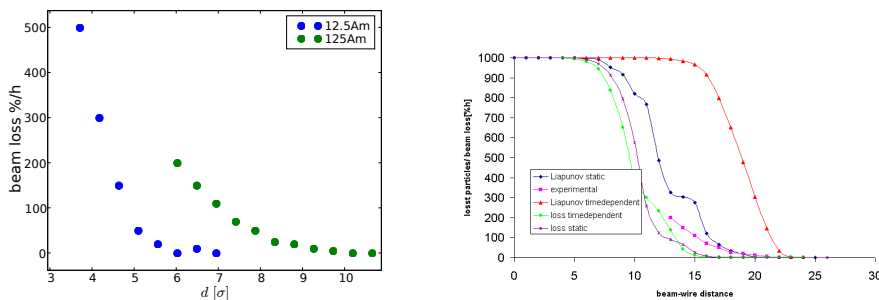


5.4 BBLR experiments at injection energy

5.4 BBLR experiments at injection energy

In 2007 BBLR experiments with fully stripped Gold ions Au^{79+} were performed. Except where the tune measurement system had obvious difficulties to deal with the introduced coupling, the measured tune and orbit followed the theoretical predictions 3.23.

Figure 5.7 a shows the experimental results of beam-wire separation scans at 12.5Am and 125Am at $Q=(0.22/0.23)$. The result for $I \times l = 12.5Am$ is equivalent to the LRBB experiments at injection energy as a bunch current of 2E11 corresponds to $\approx 10Am$. In both cases the onset of beam loss is found at $\approx 6\sigma$. Subfigure b shows simulations using various stability criteria. Using the Lyapunov criterion in simulations of experiments where the beam-wire separation is modified in steps, fails as these sudden changes increase the amplitude dependent detuning stepwise, which is identified as an instability by the Lyapunov criterion. The Lyapunov criterion in static simulations is more sensible than the loss criterion and obviously identifies the onset of beam loss accurately.



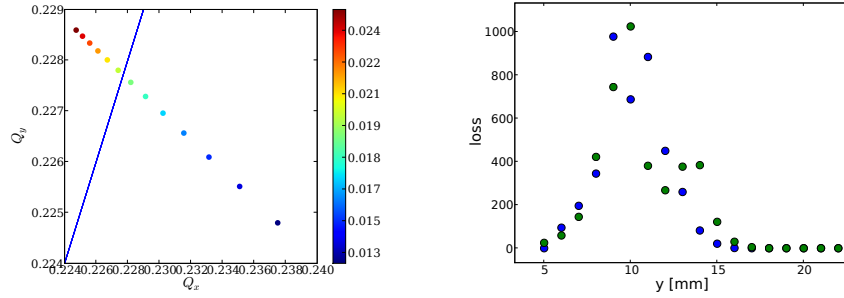
(a) Experimentally observed beam-loss during a beam-wire distance scan at 12.5Am and 125Am.

(b) Comparison of several stability criteria

Figure 5.7: Beam-wire separation scan at injection energy in experiment and simulation allowing a selection of the best suitable stability criterion.

The tune of the bunch core in case of no tune compensation for various beam-wire separations is shown in Figure 5.8 a). The resonance line enhances the loss rate at higher beam-wire separation 15 mm in case of no tune compensation, 12 mm in case of it activated and reduces the additional beam loss in the following step. Subfigure b illustrates the simulated effect of the missing tune compensation during one simulation run where the distance d is changed stepwise. The number of particles that become additionally instable at each step is plotted. As the linear tune shift is negligible at high d , the onset of beam loss occurs at the same beam-wire distance in both cases. For lower values of d the loss shape varies as the linear tune shift

becomes non negligible as particles tunes are shifted towards resonances at a different rate.



(a) Tune of low amplitude particles as a function of beam-wire distance for 125Am. the color encodes the beam-wire separation d
 (b) Simulated effect of the missing tune compensation at 125Am.

Figure 5.8: Beam-wire separation scan at injection energy at $I \times l=125\text{Am}$

Figure 5.9 shows a simulated beam transfer function (BTF). While for high values of d , only frequencies right at the unperturbed betatron tune can be excited, a broad band of lines appear in the spectrum for low separations.

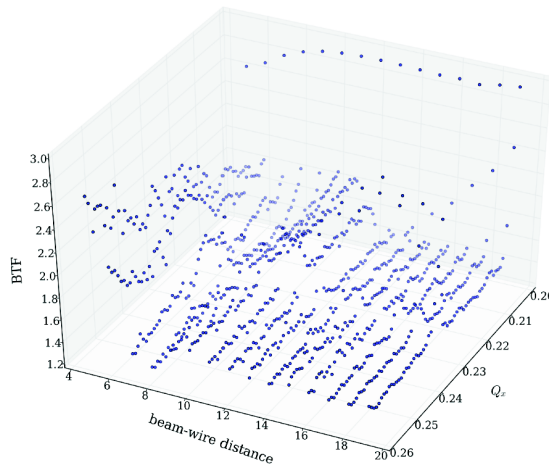
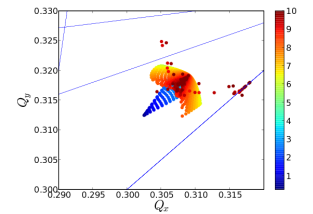


Figure 5.9: The simulated Beam Transfer Function (BTF) for the 125Am d -scan shows the broad band of spectral lines for low values of d



5.5 BBLR experiments at top energy

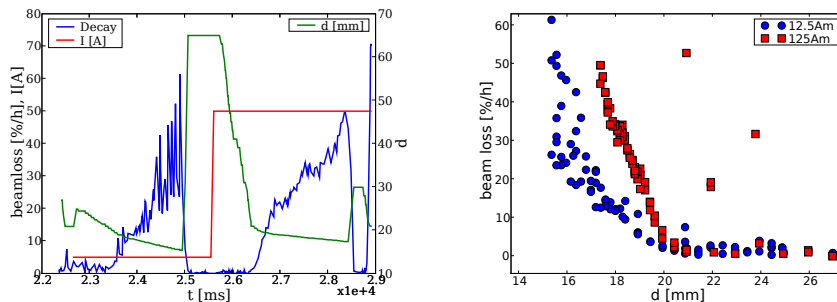
5.5 BBLR experiments at top energy

In 2007 three successful sets of experiments were performed at top energy (100GeV/nucleon). At top energy the β functions at the location of the BBLR are asymmetric: $\beta_x = 1300$, $\beta_y = 400$. As the turn around time (=time between the end of one store to the beginning of the next one) in RHIC is almost one hour, it was attempted to perform a series of experiments within one store probing the same beam several times. While the first experiment is done on a fresh beam, the subsequent ones therefore are performed on an already modified beam.

This fact may explain that the onset of beam loss was found at the same value of d for a wire excitation of 12.5Am and for the following 125Am in the beam-wire separation scans. Re-population of the tails due to a diffusion process seems to slightly counteract this effect in the blue ring.

5.5.1 MD1

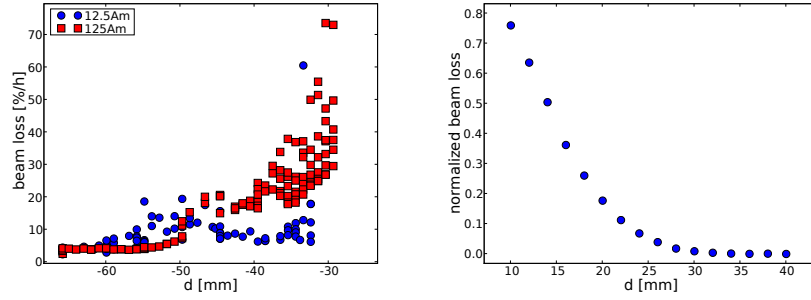
In the first BBLR experiment at top energy (RHIC fill #8609 on the 25 April 2007.), a beam-wire distance scan at 12.5Am was performed followed by one at 125Am. Figure 5.10 a shows the beam loss, the wire current and the wire position in course of the experiment for the blue and yellow ring. Subfigure b shows the extracted beam loss data as a function of the beam-wire separation. Obviously the first 12.5Am scan perturbed the bunches significantly as the onset of beam loss in the following 125Am scan is found at the same value of d . This allows to identify $d=15\text{mm}$ at 12.5Am to be equivalent to $d=20\text{mm}$ at 125Am. For both the blue and yellow beam (see Fig. 5.11 the onset of beam loss at 12.5Am is found at $\approx 7\sigma$).



(a) Beam loss, wire current and wire position as a function of time.

(b) The experimental onset of beam loss for 12.5Am is found at $d \approx 7\sigma$.

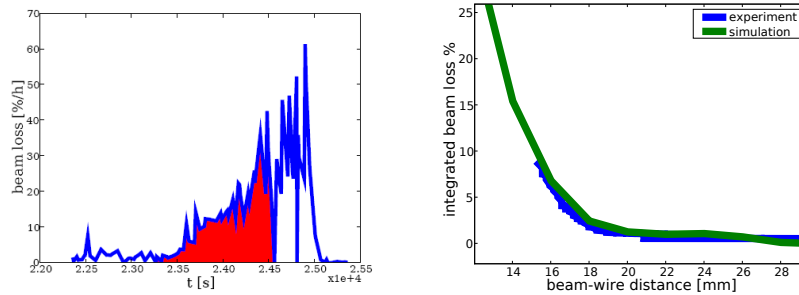
Figure 5.10: Beam wire separation scan in the blue ring at $Q = (0.234/0.226)$ for two different wire currents. The vertical beam size at the BBLR is $\sigma_{y,BBLR} = 3.2\text{mm}$. The 125Am data is obviously obscured by the preceding 12.5Am scan.



(a) The experimental onset of beam loss for 12.5 Am is found at $\approx 7\sigma$ (b) The simulated onset of beam loss is at found at $d=32$ mm as compared to the measured $d=37$ mm

Figure 5.11: Beam wire separation scan in the Yellow ring at $Q=(28.228/29.235)$, The vertical beam size at the BBLR is $\sigma_{y,BBLR}=5$ mm

In order to allow a comparison between simulation and experiments more detailed than the identification onset of beam loss only, another approach was used: Comparison of the integrated experimental beamloss with the simulations as shown in Figure 5.12 a. Subfigure b presents this comparison for the 12.5 Am d-scan in the blue ring. The onset and slope of the beam loss are reproduced correctly. Figure 5.13 shows the tune footprint and stability

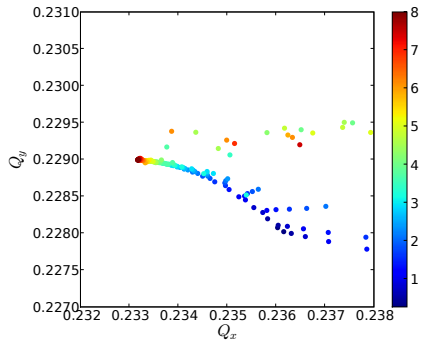
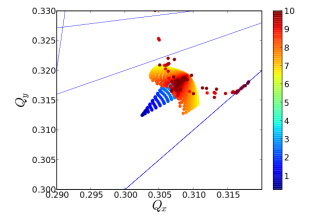


(a) The integrated loss (red area) is used as an additional observable (b) Comparison of integrated beam loss from experiment and simulation for the blue ring.

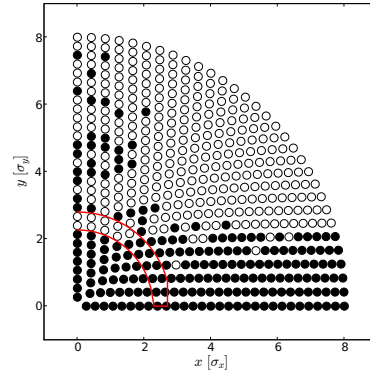
Figure 5.12: The integrated beam loss can be used as additional observable.

plot for two selected d values for the blue ring. As there are no low-order resonances coupling the two transverse planes, the border of stability in the x-y plane is roughly a horizontal line.

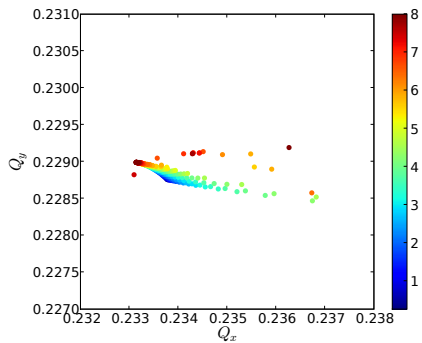
5.5 BBLR experiments at top energy



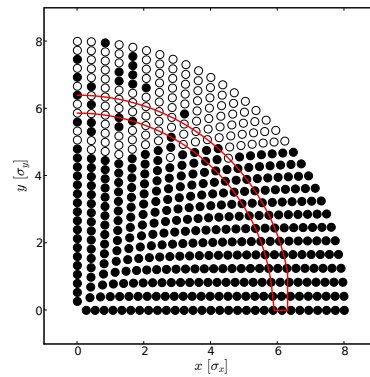
(a) Amplitude color encoded tune footprint for $d = 10mm$



(b) Stability diagram for $d = 10mm$



(c) Amplitude color encoded tune footprint for $d = 20mm$



(d) Stability diagram for $d = 20mm$

Figure 5.13: Tune footprint and stability diagram for two selected cases for the blue ring: 10mm and 20mm ($\sigma_{y,BBLR} = 3.2mm$). As there are no close-by significant resonances the border of stability is roughly horizontal. ($I \times l = 12.5Am$)

5.5.2 MD2

In order to cross check the MD1 results for tune or RHIC-ring specific issues, in MD2 (RHIC fill #8727, 09.05.2007) the d-scan was repeated at exchanged tunes between the blue and yellow ring. Once again the onset of beam loss is reproduced at 7σ in the 12.5Am case in both rings (Fig 5.14).

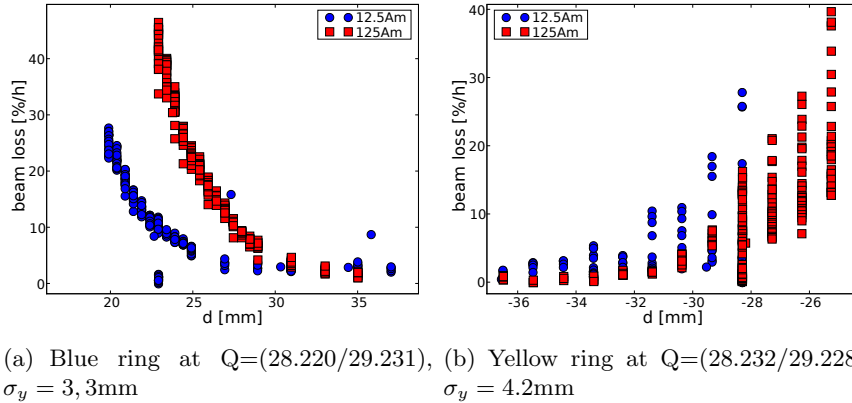


Figure 5.14: Once again the onset of beam loss is found at $d \approx 7\sigma$ in the 12.5Am case. (The beam is at the beam pipe center at 0mm).

Figure 5.15 shows beam profiles in the course of the whole experiment (consisting of a 12.5Am d-scan, a 125Am d-scan, a current and chromaticity scan) as IPM raw data (A) and normalized to a constant background in order to compensate for the varying IPM-gain. It can be seen that the bunch shape remains Gaussian and the beam loss occurs continuously over the transverse beam size. In contradiction to observations in the CERN SPS MDs, no clear cut due to a DA, as required for the scaling law (section 3.4.2), can be found.

Figure 5.16 shows details from the experiment: Subfigure a demonstrates that the beam loss occurs about equally over all bunches and subfigure b shows the measured tune during the 125Am scan that follows the theoretical predictions (eq. 3.23).

Simulations shown in Figure 5.17 a) seem at a first glance to miss the onset of beam loss, but a zoomed view (b) on the integrated beam loss shows a good agreement for the 12.5Am case. The very low integrated beam loss illustrates that the BBLR merely scratches the beam during the 12.5Am scan. The stability criterion of the Lyapunov exponent reproduces the onset of beam loss correctly. The deviation of the simulated beam loss curve from a Gaussian shape in the region -37mm to -27mm is typical for an overestimation of the effect of resonances by the Lyapunov criterion. Such effects can easily be spotted, and replaced by a smoothed curve. This smoothed curve then matches the experimental data.

5.5 BBLR experiments at top energy

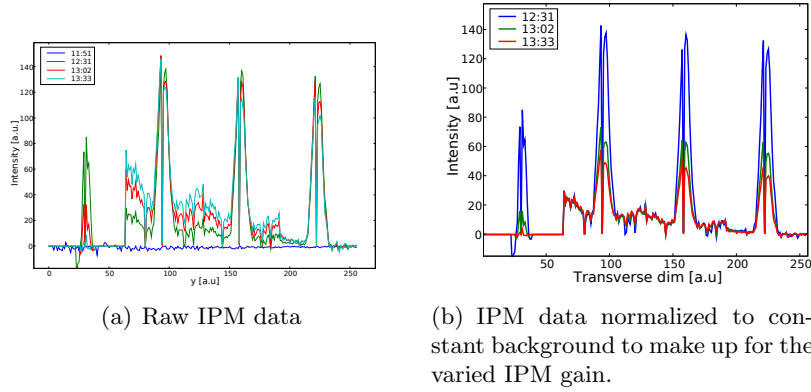
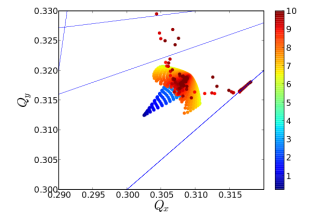


Figure 5.15: Vertical beam profiles in course of the experiment. The Gaussian beam shape is preserved.

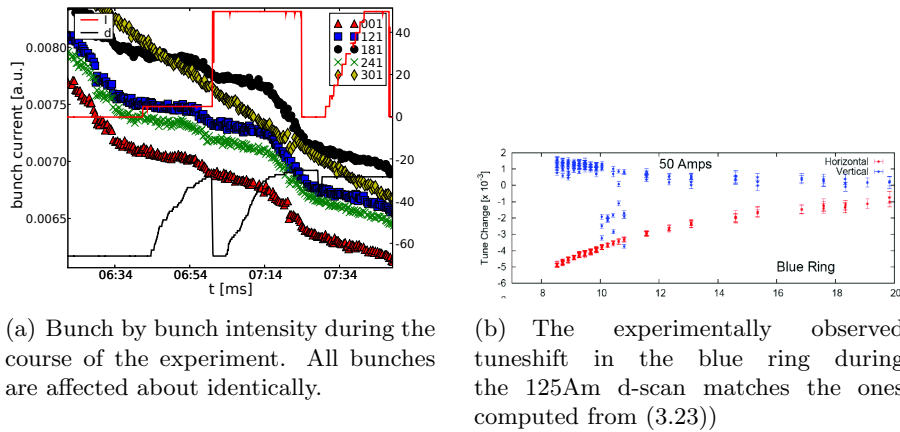


Figure 5.16: Details on the second BBLR MD at top energy

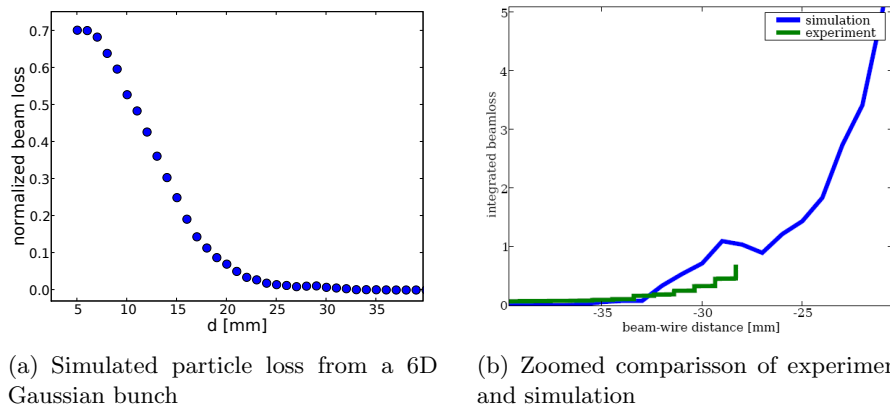
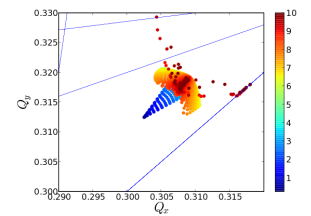


Figure 5.17: Simulations of the beam-wire separation scan during the second BBLR MD at top energy for the yellow beam. The particle loss from a 6D Gaussian bunch as a function of the separation of the 12.5Am wire is plotted. While the effect of a resonance is overestimated by the Lyapunov criterion in this comparison of the integrated loss between experiment and simulation, the onset and general loss shape is well reproduced.

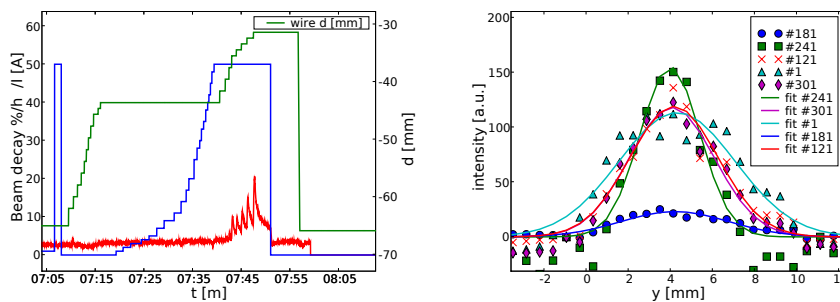


5.5 BBLR experiments at top energy

5.5.3 MD3

The third experiment on the 20 June 2007 (RHIC fill number: 9014) was performed at the end of a physics store with 110 bunches per ring. In order to stay safely off the quench limit of the magnets with this high bunch current, the instantaneous beam loss levels had to be kept low. Unfortunately the nominal loss level was already too high to obtain any valuable data from the blue ring. The yellow beam was operated at $Q=(28.228; 29.235)$ and showed a wide bunch to bunch variation in emittance and bunch intensity. Figure 5.18 b shows the vertical bunch profiles at the beginning of the experiment.

We started with a current scan at a beam-wire separation d that seemed to be 5 times the beam sigma at the time of the experiment. Figure 5.18 a shows the beam loss, the beam current and position as a function of time. No losses were observed up to the maximum current level of 125Am and the beam-wire separation d reduced until losses were measured. Unfortunately an abort-kicker failure caused a magnet quench and prohibited further studies. These obtained results contradict to all the previous ones and the

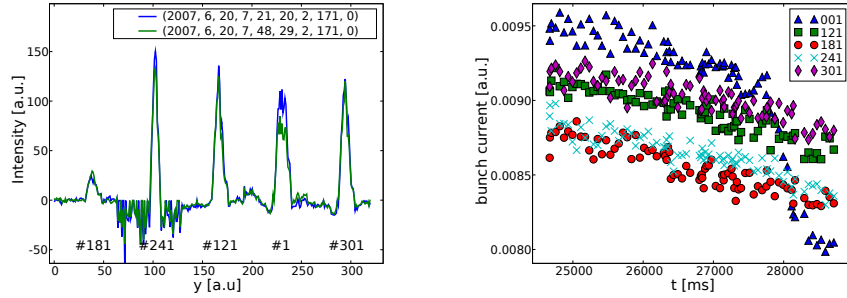


(a) A first current scan at $\approx 5\sigma$ beam-wire separation did not produce any beam loss.

(b) Vertical beam profiles and Gaussian fits at the beginning of the MD at the end of a physics store.

Figure 5.18: Conditions during the third BBLR experiment in the yellow ring.

simulations. As this experiment was performed after a full physics store, the bunches were probably already reduced to the very stable regions as the HO collisions and the lattice nonlinearities already caused potentially unstable regions in the 6D phase space to be depopulated. The beam profiles at the beginning and end of the scans (Fig. 5.19) show rather peculiar beam-shapes and decay pattern. From the 5 bunches monitored by the IPM, only bunch number 1 (which is possibly also affected by the abort gap cleaner) seems to show beam losses.



(a) Peculiar bunch profiles at the beginning and end of the experiment

(b) Bunch-by bunch beam intensity evolution. Only bunch number 1 seems to be affected.

Figure 5.19: Details on the bunch evolution during the current and distance scan in MD3

5.6 Conclusion

The RHIC LRBB and BBLR MDs allowed a very controlled study of the beam dynamics under the very clean conditions of a high energy collider. The LRBB experiments at injections showed an onset of beam loss at a beam-beam separation of $\approx 7\sigma$. These first MDs allowed to confirm the choice of the Lyapunov criterion as stability criterion in simulations. These simulations also showed the strong impact of chromaticity on the beam stability. The LRBB experiments at top energy are not as consistent: Some show beam-loss at low beam-beam separations while others do not. The BBLR experiments at injection and top energy fit the picture again. Simulations proved to reproduce the results and a new way of comparison - the integrated beam loss was identified. The third BBLR MD at top energy was performed at the end of a physics store and showed that the beam is distorted in a not observable manner.

Large Hadron Collider

(LHC)

The mission of the Large Hadron Collider (LHC), which is currently in its final stage of construction at CERN and is scheduled for start up in may 2008, is to find experimental evidence of the Higgs mechanism, to explore the quark-gluon plasma, to perform precision measurements for validating the standard model and to explore new physics frontiers. The LHC is designed to fulfill this goal by colliding hadrons at unprecedented energies (14 TeV in the center of mass in proton-proton collisions, and 5.52 TeV for nucleons in lead ions) and at unprecedented hardron-collider luminosities ($L \approx 10^{34} \text{cm}^{-2} \text{s}^{-2}$).

The LHC (Fig. 6.1) is a synchrotron consisting of a 26.7 km ring where two counter rotating beams collide within the particle physics detectors in four interaction points: ATLAS at IP1 ($s=0\text{m}$), ALICE at IP2 ($s=3332.4\text{m}$), CMS at IP5 ($s= 13329.28\text{m}$) and LHCb at IP8 ($s=23315.38\text{m}$). The remain-

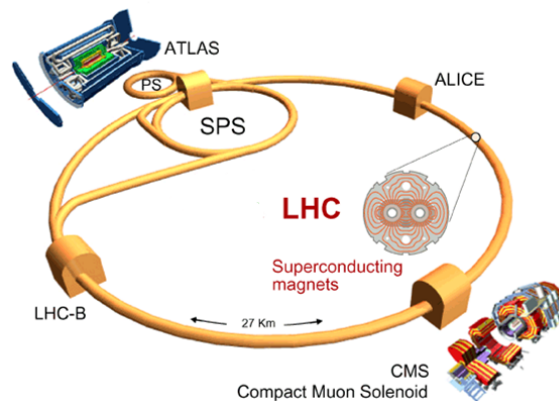


Figure 6.1: The LHC with its two high luminosity particle physics detectors, CMS and ATLAS, and two of its preinjectors (SPS and PS).

ing 4 long straight sections are used for beam collimation (IR3, IR7), RF beam acceleration (IR4) and beam dump (IR6). The 'standard' particles in LHC operation will be protons, but heavier ions such as Pb are foreseen as well. While the choice of protons for both beams allows one to reach higher

Large Hadron Collider (LHC)

luminosities as compared to proton-antiproton colliders (it is very difficult to produce high intensity anti-proton bunches), the price to pay is that more complicated “2-in-1” magnets are required.

The particles are delivered by the CERN accelerator injector chain (source - LINAC - PS Booster - PS - SPS) and injected into the LHC at 450 GeV in several batches. Once both rings are filled, the superconducting magnets are ramped to 8.4T while accelerating the beams to 7 TeV. Finally the two beams are focused (squeezed) and brought in collision at the IPs.

From the 4 detectors in nominal LHC only two (CMS & ATLAS) are high-luminosity/ low- β^* ones and only these contribute significantly to the LRBB effect. As only those two experiments will remain operational in phase 1 and 2 upgrade, just these two will be considered in the following.

6.1 Nominal LHC

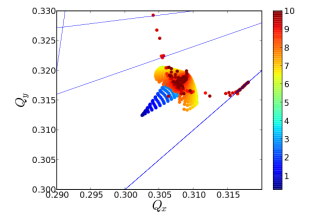
The nominal LHC is designed to accelerate 2808 bunches per ring (25ns bunch spacing) of $\approx 1.15 \times 10^{11}$ p/bunch with a normalized emittance of $\epsilon_n = 3.75\mu\text{m}$. The target rms bunch length at 7 TeV is 7.55cm and the rms energy spread to be $\delta E/E_0 = 1.129 \times 10^{-4}$.

A quadrupole first triplet focuses the two beams to $\beta_x^* = \beta_y^* = 0.55\text{m}$ under a full crossing angle of $\theta_{full} = 284\mu\text{rad}$. The latter causes a geometric luminosity reduction of $F=0.836$ and provides a constant normalized beam-beam separation of 9.5σ in the drift region around the IP ($L^*=23\text{m}$). In order to benefit from an intrinsic compensation of the linear beam-beam induced orbit and tune effects alternating crossing planes at IP1 (vertical) and IP5 (horizontal) are deployed.

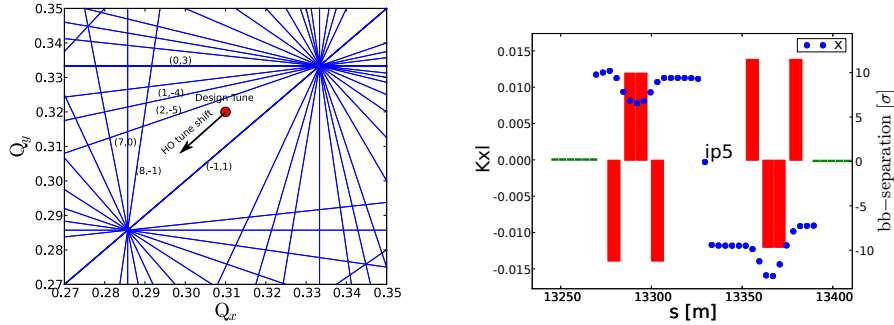
Assuming that the “D1”-dipole at $s \approx 63\text{m}$ from the IP immediately creates a sufficient beam-beam separation, one finds 16 LRBB interactions on each side of each IP at an average normalized beam-beam separation of 9.5σ . In order to accommodate the rise and fall times of various kickers in the LHC and its injector chain, not every 25ns-bucket is filled, but gaps of various length occur. Therefore only approximately half of the LHC bunches are regular bunches, all others are irregular “PACMAN” bunches.

The LHC design tunes are $Q_x = 0.31$, $Q_y = 0.32$, just below the (1,1) integer resonance. While the latter will be a potential threat to particle stability, one finds a large, resonance line free region. The tune of the majority of particles, the ones in the core of the bunch, will be lowered by the head-on related tune shift (Fig 6.2 a). Figure 6.2b illustrates the triplet-magnet configuration and the normalized beam-beam separation d at IP5. From the IP up to the innermost quadrupole the normalized beam-beam separation is constant at 9.5σ . A quadrupole focuses in one plane and defocuses in the other one, causing a variation of d ranging from 6.8 to 12.8σ . As the two beams cross in the vertical plane at IP1, additional beam

6.1 Nominal LHC



steering is required there to undo the vertical separation.



(a) Working point of the nominal LHC in a tune diagram with resonance lines up to 10th order

(b) Triplet strength and normalized beam-beam separation around IP5 (horizontal crossing). The red bars indicate the magnet's quadrupole strength, the green ones the dipole fields

Figure 6.2: Design LHC working point in a tune diagram (a) and optics configuration plus beam-beam separation around IP5 (b).

Figure 6.3 illustrates the crossing scheme. The green and blue line show the reference orbit of beam 1 and 2, respectively. These orbits are defined by the separation dipoles and exhibit no crossing angle. Additional orbit correctors are used to alter the closed orbit around the reference orbit (red line).

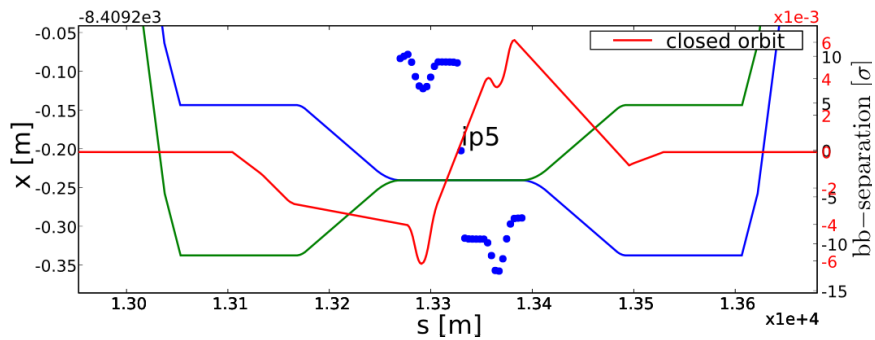


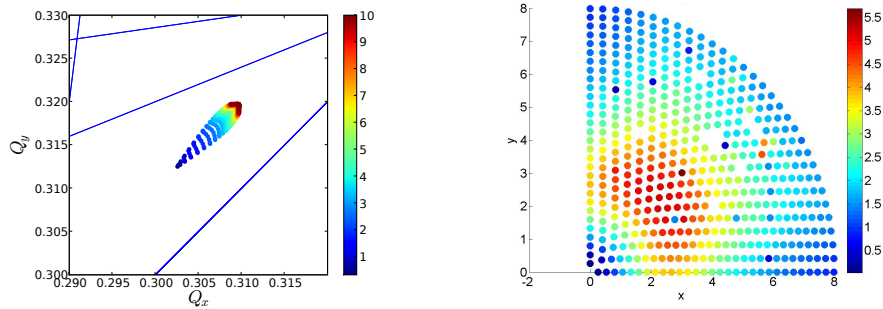
Figure 6.3: Beam-beam separation (blue dots), reference orbit (green for beam 1 & blue line for beam 2) and closed orbit.

The triplet errors taken by themselves cause a DA of $\approx 17\sigma$ (simulated in BBTrack), an effect negligible compared to the LRBBI.

6.1.1 Beam-beam interaction of nominal bunches

Head-on beam-beam effect

Different from the experiments and simulations of the BBLR studies in the CERN SPS and RHIC at BNL shown in the previous chapters, the following studies will have to include the effect of the head-on collisions. Figure 6.4 a shows a simulated amplitude color encoded head-on tune-footprint for the HO related tune-shift, which can be computed according to 3.11 to $\xi \approx 0.008$ for 2 IPs at nominal bunch intensity. Subfigure b depicts the Lyapunov exponent after 300.000 turns for various initial conditions. While there are regions with a higher amplitude dependent tune shift and thus increased Lyapunov exponent, no chaotic motion is found. As expected from the shape of the head-on force the distortions are strongest at $\approx 2.5\sigma$.



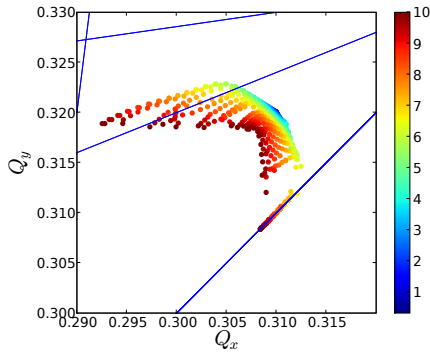
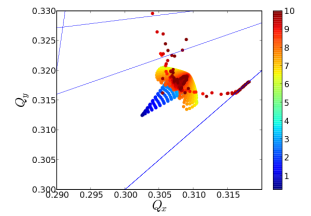
(a) Head-on related tune-footprint in nominal LHC (b) Color encoded value of the Lyapunov exponent shows a chaotic motion and strongest perturbation at $\approx 2.5\sigma$.

Figure 6.4: The effect of the Head-on beam-beam interaction on the beam dynamics: A linear tune shift, an amplitude dependent tune spread and an increased but still linear Lyapunov exponent

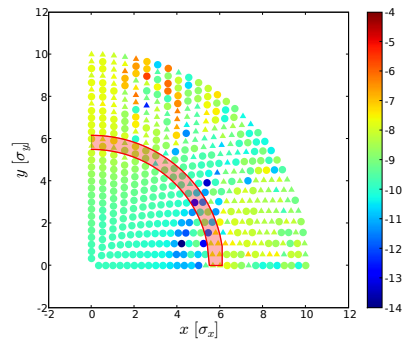
LRBBI

While the H0 collision affects the low amplitude particles, the LRBBI modifies the dynamics of higher amplitude ones and can potentially cause beam loss. Figure 6.5 a shows the amplitude dependent tune shift due to LRBBI. Particles that would be positioned in the stopband of the (1,-1) resonance, lock to it. Subfigure b shows that this causes a finite DA of 5.5σ . The coloring encodes the tune diffusion between the first and second sets of 500 turns. According to this figure a tune diffusion larger than -8 is a sign of chaotic motion.

6.1 Nominal LHC



(a) Amplitude color encoded tune spread due to LRBBI in nominal LHC showing many particles locking onto the (1,-1) resonance

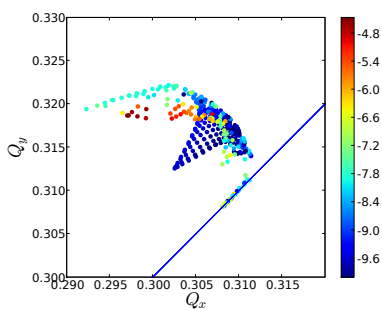


(b) Initially launched particle distribution. Triangles indicate chaotic particles, circles stable ones (inferred from the Lyapunov criterion). The color encodes the tune diffusion and the reddish region the DA.

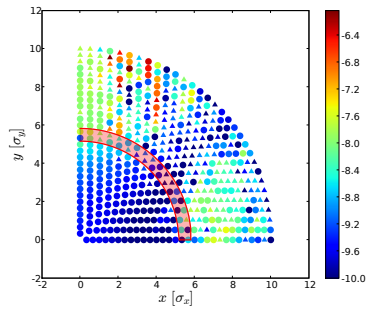
Figure 6.5: Tune footprint and stability due to LRBBI in nominal LHC

HO & LRBBI

Taking both, HO and LRBBI, together causes a tune footprint folding as illustrated in Figure 6.6 a. The color encodes the tune diffusion, which increases where the folding occurs. Subfigure b depicts the same case in the x-y plane showing the DA at 5.3σ . Figure 6.7 tries to illustrate the



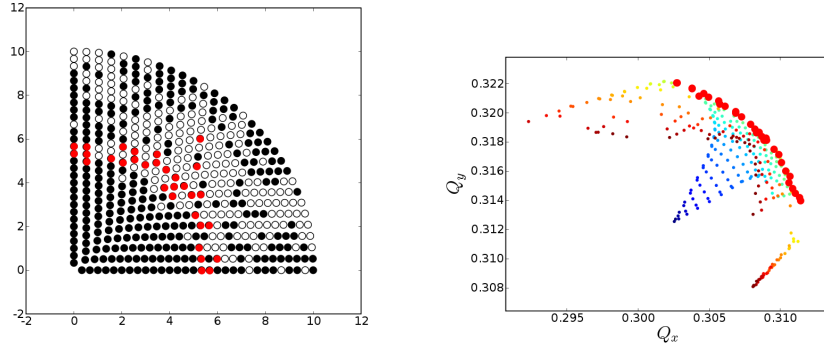
(a) Tune diffusion color encoded tune footprint (all particles shown)



(b) Tune diffusion color encoded stability plot

Figure 6.6: Combined Effect of the LRBBI and HO on the beam dynamics.

correspondence between a particle's position in the tune footprint and its stability. The particles marked red are the same in the two subfigures. In subfigure a they indicate stable particles right at the border of stability, and in subfigure b we find the same particles at the folding edge in the footprint.



(a) Stability diagram with the border of stability highlighted (b) Amplitude color encoded tune footprint (all particles shown)

Figure 6.7: Stability diagramm and tune footprint. The red dots in both figures indicate the same group of particles right at the stability border

In the following the dependency of the stability on various parameters is studied. The first straightforward variable is the bunch current, which changes the excitation strength of the various resonances, but does not alter their relative magnitude. As the LRBBI kick is linearly proportional to the beam-current and the luminosity quadratically, increasing it seems a good parameter to raise in order to enhance the performance (see LHC phase 2 upgrade proposal “LPA” in section 6.3.2).

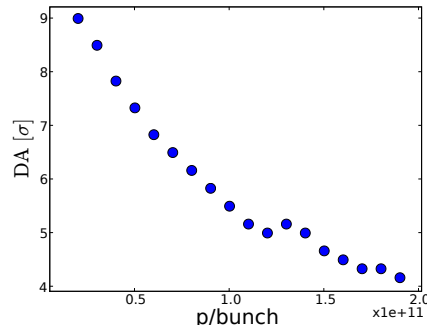
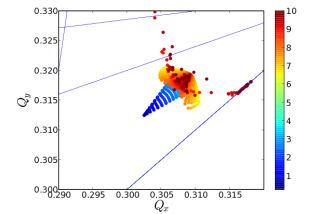


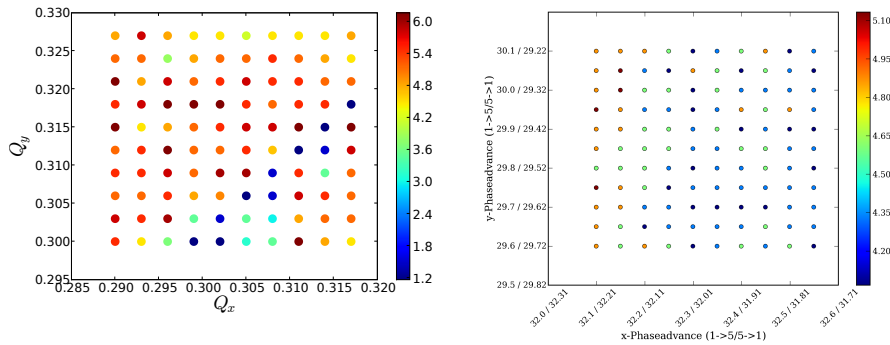
Figure 6.8: Simulated dependence of the DA on the bunch current. The simulation model includes the LRBBI, HO and a typical seed of triplet errors.

Changing the working point causes the particles to experience different resonances. A tune scan around the nominal working point, as shown in 6.9 a, indicates a sufficiently large region with a DA above 5σ . It includes a few cases with a working point above the (1,-1) resonance revealing an equivalent beam-beam performance. It still seems favorable to stay below



6.1 Nominal LHC

the resonance, since in this case the bunch of the core is closer to the main resonance. In principle a suitable choice of the phase advance between IP1 and IP5 can suppress some (but not even) resonances. Subfigure b shows the DA as a function of the horizontal and vertical phase advance. The LHC design one is located close to the lower left corner in a region of comparably good performance. While some general tendencies can be noticed, strong fluctuations result in too high tolerances on the exact settings to benefit from narrow local maxima in practice [24].



(a) DA (color encoded) for a range of working points around the nominal one (0.31/0.32). A sufficiently large region in tune space with DA above 5σ is found.

(b) DA (color encoded) as a function of the x and y phase advance. While a general tendency is found, strong fluctuations occur. The nominal design is located in the lower left corner.

Figure 6.9: Dependence of the beam stability on the chosen working point and on the phase advance between IP1 and IP5

6.1.2 Compensation of LRBBI of nominal bunches

In the nominal LHC the wire compensator can be placed at $s=104$ m, where $\beta_x \approx \beta_y \approx 1760$ m. Figure 6.10 shows the phase advance from the IP to the LRBBI and to the BBLR. As the phase advance is given by $\phi = \int ds/\beta(s)$, it is large from the IP to the first LRBBI but small from one LRBBI to another or to the BBLR. The average phase advance from the LRBBI to the BBLR is an important parameter for the compensation efficiency. It is 3.6° in nominal LHC.

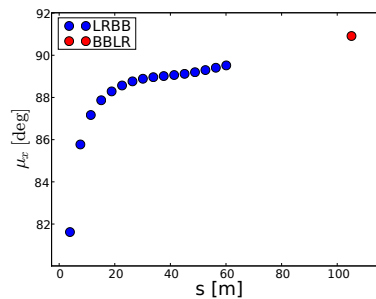
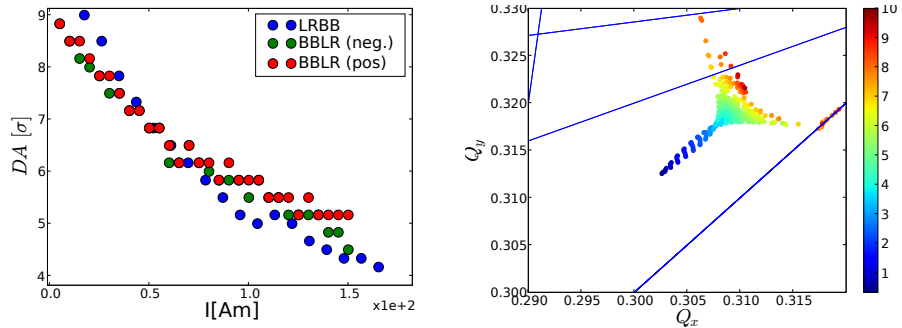


Figure 6.10: Horizontal phase advance from the IP to the LRBBI and the BBLR

HO & BBLR

As opposed to the LRBBI, in simulations a BBLR by itself causes beam loss even for a very small, but nonzero current due to the singularity at the wire center. Figure 6.11 shows simulations of the DA as a function of the excitation wire current in case of the BBLR (both polarities) and the LRBBI. All simulations include the head-on beam-beam interaction. While the singularity causes an enhanced beam-loss for low BBLR currents, the case of a BBLR in compensator polarity exhibits slightly fewer losses for higher currents as no tune footprint folding occurs (In all cases no significant resonance is crossed).



(a) Dynamic aperture as a function of the BBLR current in case of no LRBBI as compared to LRBBI

(b) The amplitude color encoded tune footprint due to HOI and the BBLR at 80Am (compensation polarity) shows no tune footprint folding

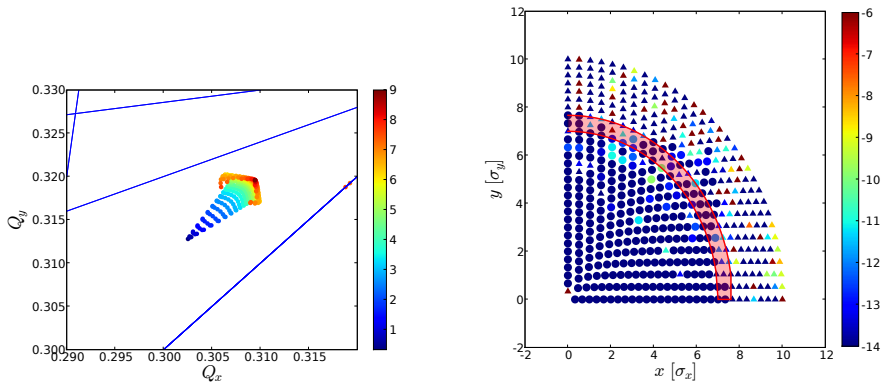
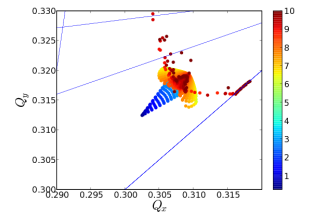
Figure 6.11: The DA as a function of the wire current (a) and the tune footprint at 80Am. The singularity in the field of the wire explains the reduced DA at low wire excitations and the lack of tune footprint folding the increased DA at large wire current as compared to the HOI-LRBBI case.

HO & LRBBI & BBLR

The optimal compensation current for the nominal LHC is computed to 81Am at a transverse offset of the BBLR of $d=9.5\sigma$ assuming one wire per beam on each side of each IP. Figure 6.12 shows that these settings allow reducing the footprint to almost the one of the case with HO collision only. As a consequence the tune of higher amplitude particles stays well off the significant resonances and no tune footprint folding occurs. Subfigure b shows that this translates into a rise of the DA to 7.2σ (to compared with an uncompensated $DA = 5.2\sigma$). Within the stable region, the tune diffusion is reduced by 3 orders of magnitude.

As the beam parameters change during operation and vary from bunch to bunch, it is illustrative to explore the effect of some parameter variations.

6.1 Nominal LHC

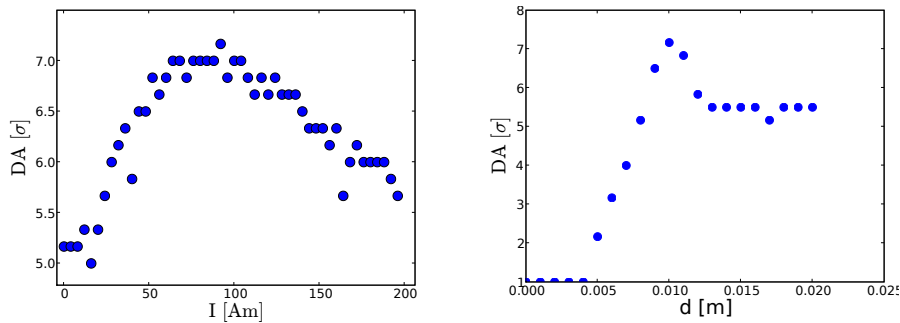


(a) A BBLR at 80Am reduces the tune footprint of the nominal LHC to the footprint of head-on only one .

(b) The tune diffusion color encoded stability diagram does not only show an increased DA, but also a reduced tune diffusion for small amplitude particles

Figure 6.12: Tune footprint (a) and stability diagram (b) for 80 Am BBLR compensation

Figure 6.13 a) shows the DA as a function of the BBLR current. Starting from an uncompensated DA at 5.1σ the compensation increases steadily and reveals a wide good area around the optimal current $I=81$ Am. Subfigure b shows the DA for various beam-wire separations d at constant excitation $I=81$ Am, where a region of effective compensation is found at $\approx 5mm \approx 5\sigma$, with a distinct maximum. The positioning and beam-steering precision is well above this. Beam-size variations will not alter the efficiency as in this case the LRBBI also occurs at modified normalized separations.

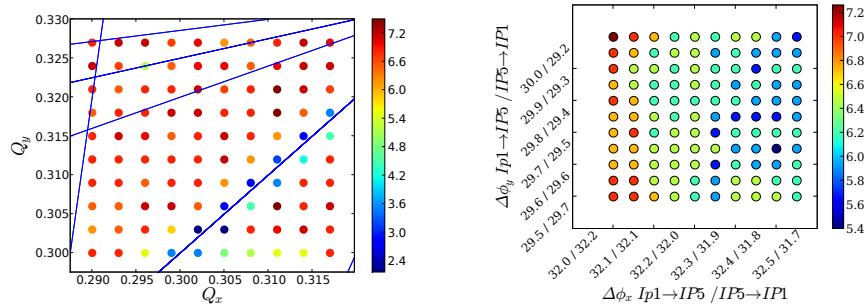


(a) A current scan of the BBLR at 9.5σ shows a wide current region where the compensation is efficient.

(b) The DA as a function of the beam-wire separation d for $I=82$ Am.

Figure 6.13: The DA as a function of the BBLR current (a) and of the beam-wire separation d (b)

Finally the robustness of the compensation with respect to tune and phase advance modification is studied. A tune scan (Fig. 6.14a) shows that the DA is improved for a wide tune region and less fluctuations occur than without compensation (Fig. 6.9 a). The impact of high order resonances almost completely vanishes. Subfigure b shows a phase advance scan. Compared with the uncompensated case (Fig. 6.9 b), the performance is enhanced for all phase advances and due to the resonance suppression the fluctuations are reduced.



(a) A tune scan of the working point shows enhanced stability over a wide region

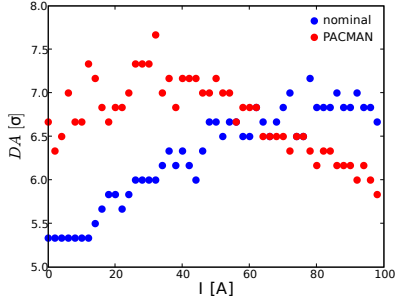
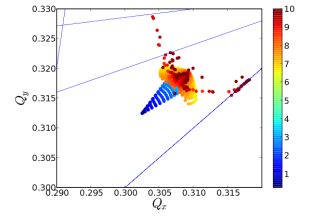
(b) The compensation works for all phase advances and it also reduces the fluctuations.

Figure 6.14: Compensation efficiency for working points around the nominal one in the tune/phase advance-planes

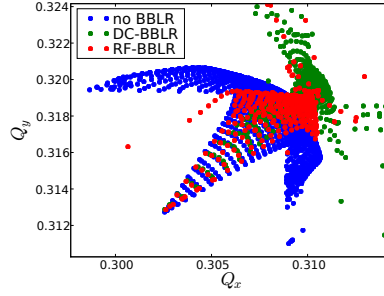
6.1.3 Compensation of LRBBI of PACMAN bunches

PACMAN bunches suffer less LRBBI and are therefore expected to have a better beam-beam performance. The $I=0\text{Am}$ case in the figures in 6.15 shows the reduced footprint and the enhanced DA (6.5σ as compared to 5.1σ for nominal bunches). So far the BBLR performance was presented with respect to the nominal bunches. PACMAN bunches are bunches at the end of a bunch train, that experience a reduced number of LRBBI (in the extreme case no LRBBI on one side of the IP). As shown in figure 6.15a an intermediate DC current level can be found that improves the DA of both, the nominal and the PACMAN bunches. Subfigure b presents the effect of the BBLR on the extreme PACMAN bunch in case of three different current levels: none, optimized for nominal bunches (DC-BBLR, 81Am) and optimized for PACMAN compensation (RF-BBLR).

6.2 Upgrade phase 1



(a) DA as a function of the BBLR excitation current for the extreme PACMAN and nominal bunches. An intermediate current level can improve both.



(b) Footprint of the extreme PACMAN bunch for various BBLR excitations: uncompensated, overcompensated and perfectly compensated

Figure 6.15: Compensation for the extreme PACMAN bunch as compared to a nominal one.

6.2 Upgrade phase 1

Due to radiation damage, by 2013 the whole triplet will need to be exchanged and a new interaction region (IR) scheme with reduced $\beta^* = 25$ cm will be implemented in order to boost the luminosity. In the following, 3 different quadrupole first optics - “Low β max”, “Modular” and “Compact” - as proposed by R. de Maria et al in [25] - are discussed with respect to their beam-beam performance. A fourth option, similar to the low β max one, called “symmetric” was proposed by J.P Koutchouk, E Todesco et al in [26]. In order to keep an average beam-beam separation of $\bar{d} \approx 9.5\sigma$ for the reduced β^* , the crossing angle is increased with respect to the nominal LHC (from $\theta = 284\mu\text{rad}$ to $450\mu\text{rad}$). Given the same magnet technology, the stronger focussing requires a longer triplet and hence introduces more long-range beam-beam encounters (LRBBIs). Their number and other important parameters are summarized in Table 6.1 and Fig. 6.16. A suitable position - because of the increased β function possibly an even better one compared to the nominal scheme- for a wire compensator can be found in all scenarios.

Large Hadron Collider (LHC)

variable	nominal	low β max	Compact	modular
β^* [m]	0.55	0.25	0.25	0.25
#LRBBIs	16	19	22	23
wire @ [m]	104	136	170	160
β_{wire} [m]	1780	3299	2272	3000
σ_{dsep}	1.6	3.6	2.2	2.3

Table 6.1: Parameters defining the long-range beam-beam (LRBB) performance of the nominal optics and the three proposed phase 1 upgrade optics

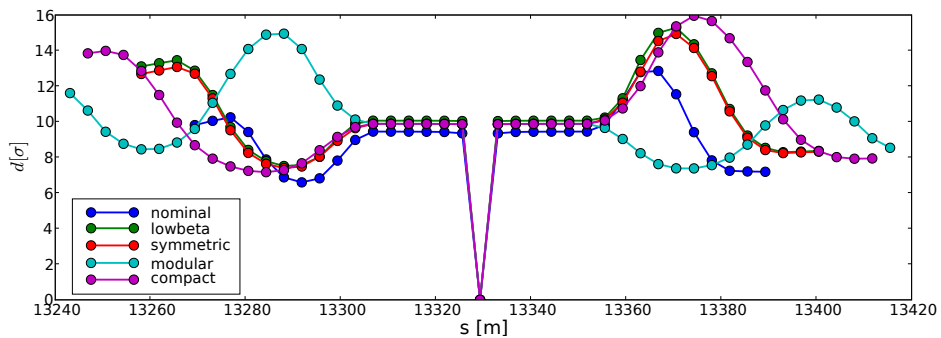


Figure 6.16: Comparison of the normalized beam-beam separation at IP5 for the nominal LHC and four upgrade scenarios. While an increased crossing angle keeps the average normalized beam-beam separation at 9.5σ , the number of LRBBIs is also increased.

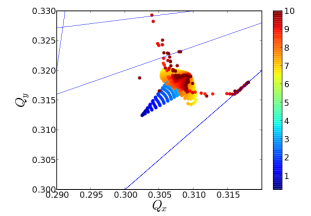
The simulations presented in the following sections proved that the simple criterion of minimizing the number of LRBBIs is a reasonable guide for optimization, and that accordingly the low β -max optics performs best.

6.2.1 Low β max

Like in the nominal LHC optics, this option proposes a triplet focusing scheme. It attempts to make use of the highest possible quadrupole field gradient while still providing some additional aperture margin in the triplet. These choices limit the peak β function in the triplet. As the wire compensator should ideally be placed at locations with identical β functions in the transverse plane, it is to be installed at $s=142m$, where $\beta_x = \beta_y = 3225m$. The resulting rms beam size of 1.25 cm allows for a BBLR with reasonable dimensions.

As shown in the comparison of Figure 6.16 this optics contains a few additional LRBBIs at an increased beam-beam separation. The DA is therefore only slightly lower as compared to the one of the nominal optics: $DA \approx 5\sigma$

6.2 Upgrade phase 1



for 1.15×10^{11} p/bunch (DA $\approx 5.3\sigma$ for nominal LHC). Figure 6.17 shows the tune-footprint and the stability diagram of the low β max optics, which indeed resemble the nominal ones (Fig. 6.6).

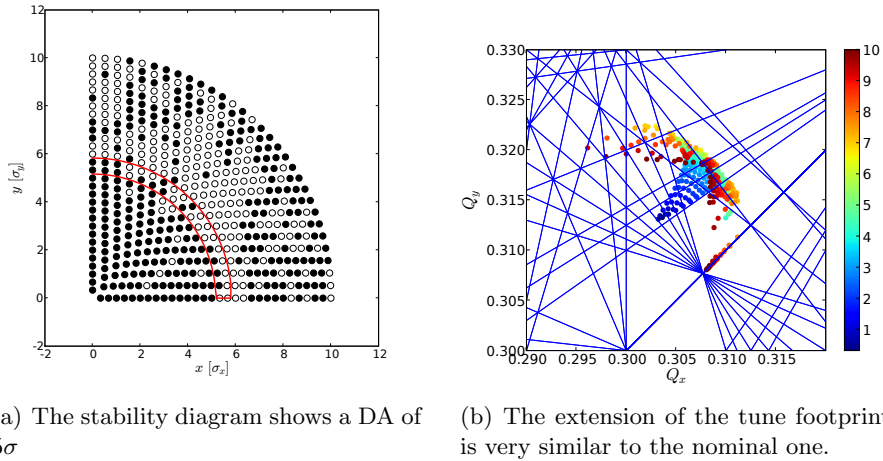
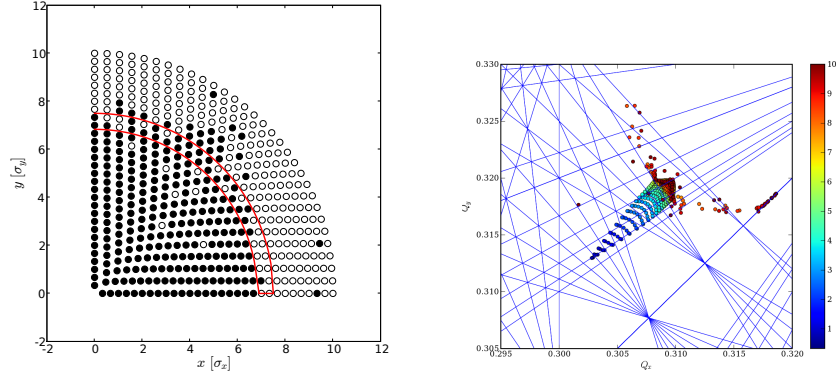


Figure 6.17: Stability diagram and tune footprint of the low β max optics for $1.15 \cdot 10^{11}$ p/bunch.

One of the parameters defining the efficiency of the BBLR is the distance spread of the LRBBI. While σ_d in this case is rather large, the compensation works still reasonable well, reducing the footprint (Fig. 6.18 a) and enhancing the DA to 7σ (subfigure b)

Possibly in parallel to a reduction in β^* , it might be attempted to boost luminosity by increasing the beam current to 1.7×10^{11} p/bunch. In this case, without BBLR, the DA shrinks to 3.8σ .



(a) The stability is enhanced to 7σ .

(b) The tune footprint is reduced to the one of the HO.

Figure 6.18: A wire compensator allows an elimination of the long-range beam-beam tune spread and increase of the DA for the low β max optics with 1.15×10^{11} p/bunch.

6.2.2 Compact

The so-called “compact” optics proposal also features a triplet layout and it uses the lowest possible gradient compatible with tolerable aberrations. Under these constraints it is attempted to minimize the overall length by optimizing the gradient for Q1 and optimizing the lengths of Q1, Q2 and Q3.

In striking discrepancy to its name, the triplet length is increased as compared to the previous case resulting in 22 significant LR encounters. The best possible location for a BBLR is at $s=169m$ with $\beta_x = 2240m$ and $\beta_y = 2260m$. The increased number of LRBBIs lowers the DA to 4.2σ . Figure 6.19 b depicts the large tune spread reaching out to the (2,-5) resonance and the tune folding at 4.5σ . The resulting reduced stability is shown in subfigure a.

Figure 6.20 shows that a wire compensation increases the DA to 6.2σ , which is still higher than the one of an uncompensated nominal optics. The figure also tries to explain what limits the improvement. Red and green dots indicate identical particles in both subfigures. These particles surround the stability droops that indicate the perturbed regions in the tune footprint where the (4,-7) and (6,7) resonance line cross.

6.2 Upgrade phase 1

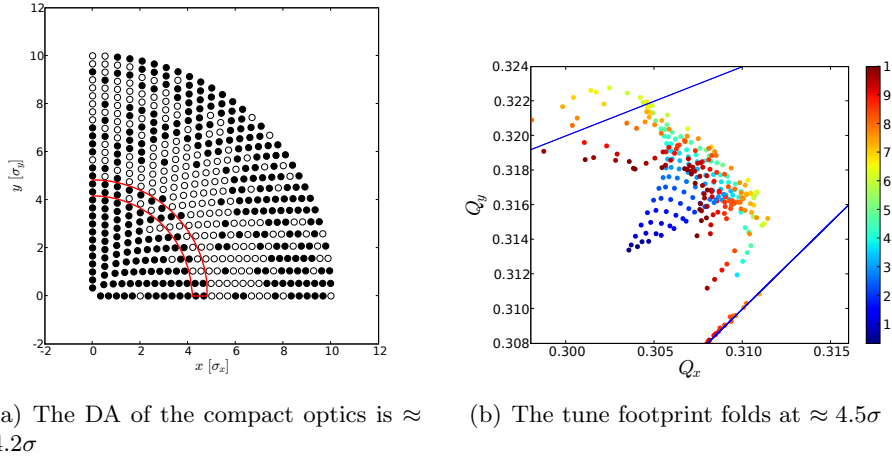
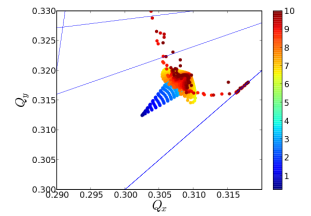


Figure 6.19: Stability diagrams for the “compact” optics without wire compensator for 1.15×10^{11} p/bunch.

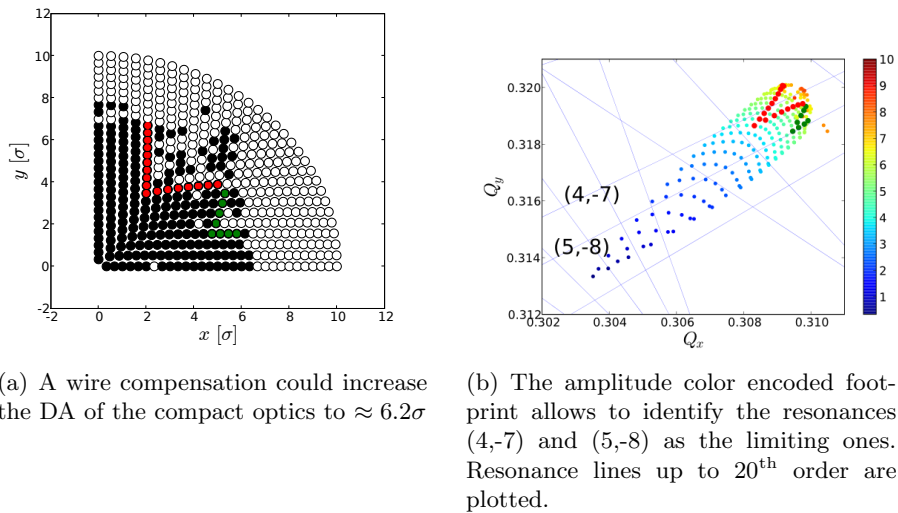


Figure 6.20: Stability plot and tune footprint for the wire compensated “compact” upgrade optics. The red and green dots mark an identical group of particles in the two pictures that surround the stability droops.

6.2.3 Modular

Unlike the optics discussed so far, the “modular” one uses a quadruplet design with magnets of an intermediate field gradient. While all magnets are of the same length, the first two have a larger gradient. This implies either a reduced aperture for the first two modules or reduced aperture margins in the other ones. Figure 6.21a) depicts the layout and beta functions, which now exhibit two local maxima in one plane on each side of the IP. This translates into the variation of the beam-beam separation shown in Figure 6.16. As this optics is even longer than the compact one, there are 23 significant LR encounters per side per IP. A suitable location for the wire can be found at $s=162m$ where $\beta_x = \beta_y = 3200m$. Figure 6.22b) depicts the large tune footprint of the modular optics, where the LRBBI even distorts the very core of the beam and reduces the DA to 4σ .

A wire compensation can increase the DA to 6.1σ .

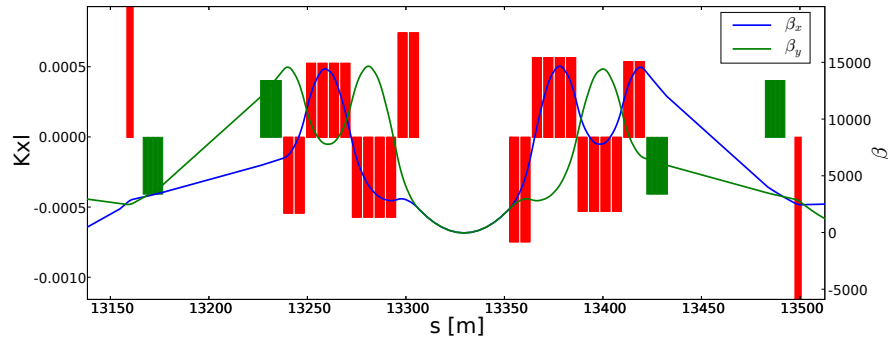


Figure 6.21: Magnet arrangement and betafunctions around IP5. The modular option features a quadruplet.

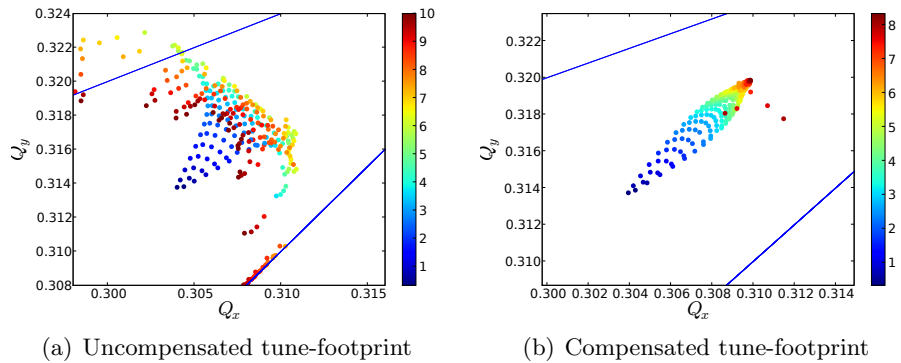
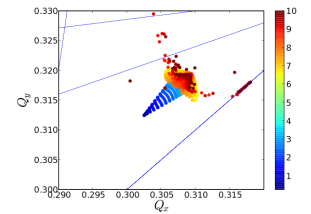


Figure 6.22: Tune footprints in the “modular” upgrade optics with and without compensation for 1.15×10^{11} p/bunch



6.3 Upgrade phase 2

6.3 Upgrade phase 2

LHC upgrade phase 2 is an even more ambitious upgrade that will include a modification of the detectors. Currently two significantly different scenarios are proposed: the “Dipole Zero” (D0) and the “Large Piwinski Angle” (LPA) option. By the time of its realization, possibly a new superconducting magnet technology based on Ni_3Sn will be available allowing for higher gradient quadrupoles.

6.3.1 Dipole Zero

The “Dipole Zero” scenario foresees a further reduction of β^* to about 12cm combined with a moderate increase of the beam current. In order to keep the geometric luminosity reduction loss small, the crossing angle must be reduced. As this would imply an unbearably enhanced long-range beam-beam effect, the installation of an “early separation” dipole (D0) close to the IP is proposed [27].

A full early separation, where the dipole is placed about 2m from the IP in order to separate the two beams before the first LRBB encounter, could operate with zero crossing angle at the IP but is excluded for reasons of radiation and detector integration issues. In case of a partial early separation scheme, which foresees the installation of the dipole at $\approx 6m$, a residual crossing angle at the IP is required. Even for an angle that implies that the LRBBIs up to the D0 occur with a distance d as low as ≈ 5 sigma, the geometric luminosity loss is unacceptable high and crab cavities are required to recover a factor 2-3 in luminosity. Another issue of this scheme is the very short luminosity life time with a high peak luminosity at the very beginning, which the detectors cannot use because the time needed for setup procedures of the detectors and accelerator. Some of this issues may be alleviated by varying the crossing angle during a physics store.

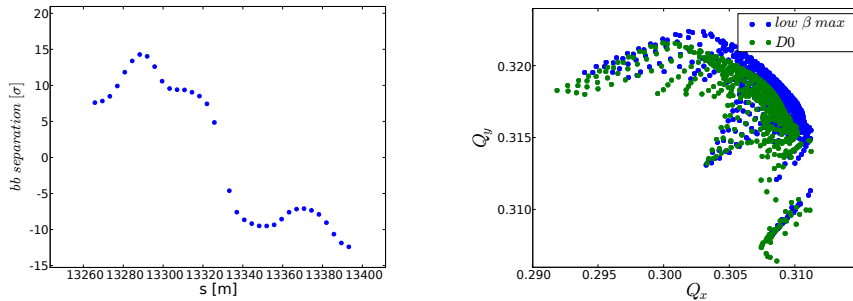
Even at the retracted position of 6 m, the radiation dose is significant and it is doubtful if this scheme is compatible with the detectors, as it may reduce the angular detector acceptance, lead to an enhanced background or complicate the detector maintenance. The designated reduced spot size at the IP causes a large increase of the sensitivity to noise created within the focusing system. As the D0 is part of the latter and its adequate mounting is problematic (in view of a possible interaction with the detector solenoid field) this issue could be important. Finally the supply of cryogenics and power may be questionable.

So far no consistent optics is available for this scheme, but for the purpose of an exploratory study, a D0 dipole was added to the low β max optics. While this allows us to study beam-beam issues related to close encounters, it may not properly address all issues. As mentioned for the phase 1 upgrade, a further decrease in β^* to 12cm would cause an increase of the triplet length

Large Hadron Collider (LHC)

and require a larger crossing angle in order to keep the same normalized beam-beam separation.

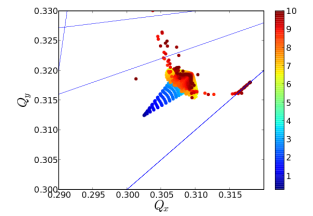
Figure 6.23 a) shows the beam-beam separation of the considered model with one encounter at $\approx 5\sigma$ per side per IP. Subfigure b) compares the resulting footprint with and without the activation of the D0 dipole. Although the footprint appears to be smaller with D0, the stability is worse: Lower amplitude particles are distorted and the tune footprint folding occurs at lower amplitudes. Fig. 6.24 demonstrates that this folding at lower amplitudes indeed reduces the DA already for the nominal beam current of 1.15×10^{11} p/bunch. Simulating with the ultimate intensity of $1.7 \cdot 10^{11}$



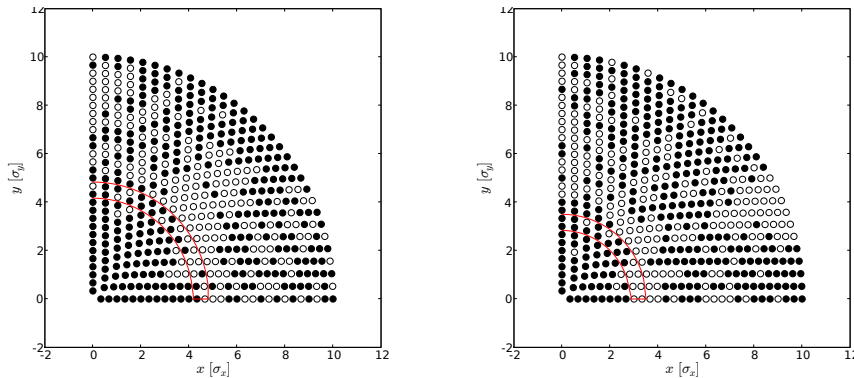
(a) Normalized beam-beam separation in the D0 considered optics model (b) Tune footprint of the low β max optics with and without D0

Figure 6.23: Beam-beam separation and tune footprint for our model D0 option based on the low β max optics with $\beta^* = 0.25$ m and 1.15×10^{11} p/bunch.

p/bunch - as foreseen for this optics - leaves an unbearably small stable region. This matches the experiments at RHIC and the CERN SPS which indicate a drastically perturbed beam-stability already with a single long-range encounter at 6-7 σ separation. In this scenario no wire compensation can be used, since the wire has a finite diameter, only functions in the $1/r$ regime of the beam-beam force and must be placed in the shadow of the collimators at amplitudes above 7σ . Only an electron lens used “as wire” would be an option [28].



6.3 Upgrade phase 2



(a) Stability with nominal beam current, 1.15×10^{11} p/bunch. (b) Stability diagram for the D0 upgrade scenario with $1.7 \cdot 10^{11}$ p/bunch

Figure 6.24: Stability diagram for the D0 option with two different bunch currents: the nominal bunch population (a) and the so called ultimate as foreseen for this scenario (b)

In order to find an acceptable beam-beam separation for the close encounters, a parameter scan was performed. Figure 6.25 shows the results of a stability study considering only the head-on interaction and two long-range encounters per side of each IP at a variable distance. The minimal acceptable beam-beam separation seems to be around 6.5σ .

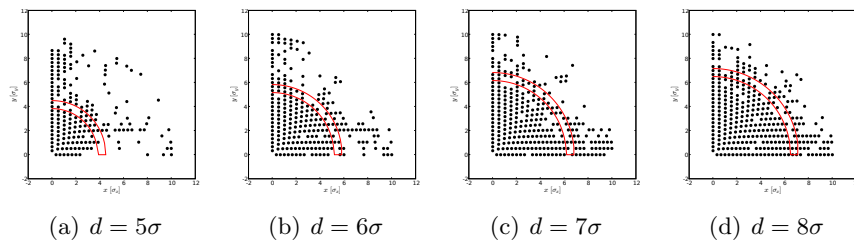


Figure 6.25: Stability diagram for the D0 model with HO and 2 LR encounter per side per IP at 1.7×10^{11} p/bunch and varying separation (crossing angle)

6.3.2 Large Piwinski Angle (LPA)

The second proposed option is the Large Piwinski Angle scheme which foresees to boost the luminosity by increasing the bunch current to $4.9 \cdot 10^{11}$ while halving the number of bunches. The production and collimation of this 2.1 times higher total stored beam current will certainly be challenging.

This approach exploits the fact, that the luminosity is proportional to the square of the bunch population N^2 while the long range beam beam

Large Hadron Collider (LHC)

effect is linearly proportional to it. All in all the scenario causes a LR effect enhanced by a factor of 2.1 compared to nominal LHC which will be compensated by BBLRS. In order to not suffer from the otherwise significantly increased HO tune shift, longitudinal flat and longer bunches are used, which in return reduces the luminosity slightly. The impact of the synchro-betatron resonances, more strongly excited at a large Piwinski angle, is not expected to be a severe issue for the low synchrotron tune of the LHC.

As the optics layout will be very similar to the one of upgrade phase 1 and not too different from nominal LHC, experimental tests can be performed already at the nominal LHC. The wire compensation can be installed without any risk at any time and its effectiveness can be proven already in the nominal LHC. In case crab cavities become indeed operational they can be installed as a complement.

This scenario is studied based on the “low β max” optics and it is well suited for the BBLR compensation scheme as the average beam-beam separation is still 9.5σ . The stability region and the tune footprint plotted in Figure 6.26 show the unacceptably low uncompensated DA at $\approx 3.5\sigma$ without compensation. A wire compensation recouperates a DA of 5.5σ

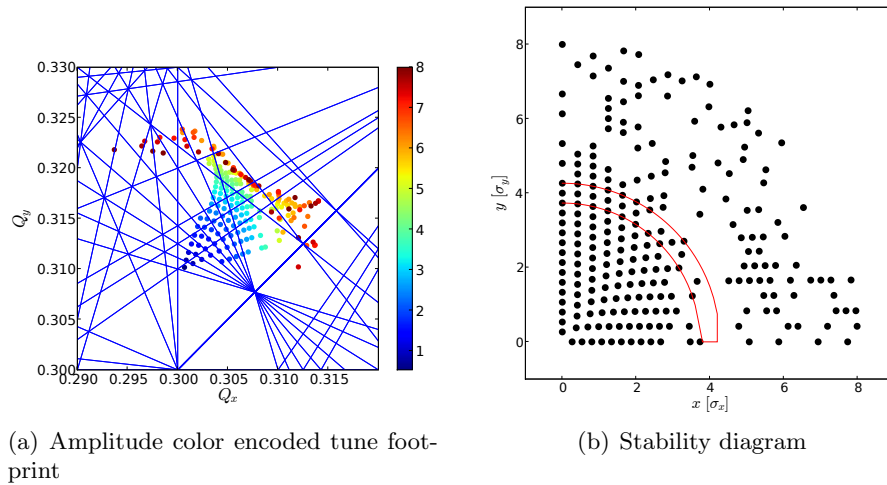
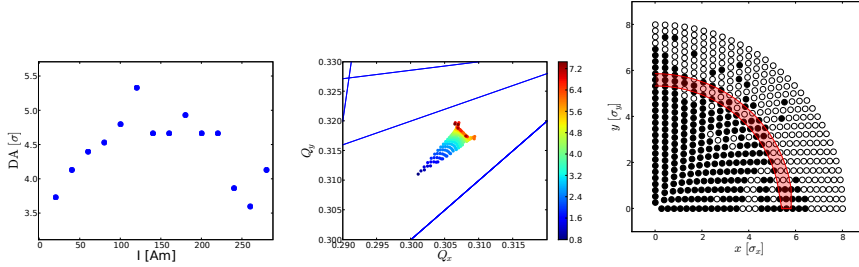
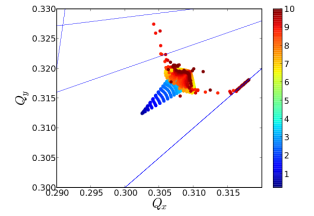


Figure 6.26: Tune footprint and stability diagram for LPA

(Fig. 6.27). The BBLR current scan shows the optimum wire excitation at $I=120\text{Am}$

6.4 Summary of LHC optics



(a) BBLR current scan (b) Tune footprint for (c) Stability diagram for showing optimal compen- I=120Am I=120Am sation at 120Am

Figure 6.27: BBTrack simulations for the “LPA” phase 2 upgrade: BBLR current scan identifying a large current region with efficient compensation (a), the tune footprint (b) and stability diagram (c) at a BBLR current of I=120 Am.

6.4 Summary of LHC optics

Table 6.2 summarizes the long-range beam-beam performance for various LHC schemes in the uncompensated and wire-compensated case. (IP1 and 5 only).

Optics	N_b [10^{11}]	β^* [m]	θ_{full} [μrad]	DA	DA incl. BBLR
nominal	1.15	0.55	284	5.3	7.2
ultimate	1.7	0.55	284	4.5	6.8
low β max	1.15	0.25	450	5	7
low β max	1.7	0.25	450	3.8	6.5
compact	1.15	0.25	450	4.2	6.2
modular	1.15	0.25	450	4	6
“D0 model”	1.15	0.25	450	4.1	-
“D0 model”	1.7	0.25	450	3	-
LPA	4.9	0.25	450	3.5	5.5

Table 6.2: Long-range beam-beam performance of various LHC optics scenarios with and without wire compensator

Pulsed BBLR and related noise issues

In order to perfectly compensate the LHC long-range beam-beam effect for nominal as well as for so-called 'PACMAN' bunches, the wire compensator strength should be adjusted for each bunch individually (Fig: 6.15b).

Each LHC ring is filled with bunch trains each consisting of 72 bunches (25 ns spacing) that are interleaved with empty slots of varying length [29]. For slots longer than 15 buckets (e.g. abort gap) the BBLR should be ramped down to zero current, while for shorter ones intermediate levels must be held to achieve a perfect compensation. In case of the minimal gap length of 8 slots the current needs to be ramped down to half the maximal strength. The ramp rate is determined by the distance between the main collision point and the location where the two beams are finally separated, e.g. the length of the region where LRBBBI occurs. In nominal LHC it is 1/15 of the maximal current in 25ns. A typical ramping pattern is shown in Figure 7.1.

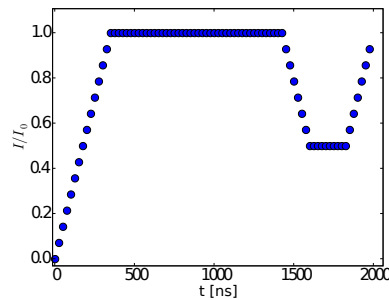


Figure 7.1: A typical ramping pattern required for adjusting the BBLR strength to the bunch pattern in the nominal LHC.

It is important to keep in mind that the compensator strength is required only every 25 ns – the moment when a bunch passes the device – but it can be chosen freely in between. The reference current I_0 depends on the beam current and needs to be adjusted in course of one store, to follow the decaying beam current, for optimal compensation.

7.1 Technical challenges

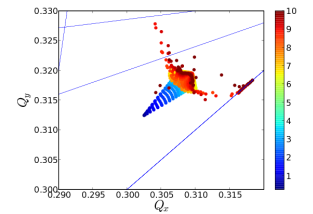
While a DC BBLR is technically a rather simple device, a ramping BBLR is a very challenging one as the following issues must be addressed:

- At the required ramping frequency (0.5MHz) the BBLR represents an inductive load. The impedance (per unit length) for an eccentric coaxial structure is given by [30]

$$Z_0 = \frac{\eta_0}{2\pi\sqrt{\epsilon_r}} \cosh^{-1} \left[\frac{D}{2d}(1 - \phi^2) + \frac{d}{2D} \right] \quad (7.1)$$

where $\eta_0 = 120\pi$, D the diameter of the outer structure, d the diameter of the inner conductor. The radial position of the inner wire is $r = \phi D/2$, where ϕ is a parameter taking values from zero to one. Assuming $D=7$ cm, $d=1$ mm and $r=8.5$ mm for the LHC BBLRs, one obtains $Z_0 = 236\Omega$. The electrical impedance seen at the connectors is given by $Z_{in} = iZ_0 \tan(2\pi/\lambda l)$. For $f = 0.5$ MHz a one meter long wire causes a $Z_{in} = 2.63\Omega$ which corresponds to an inductivity of $L = Z_{in}/(2\pi f) = 840$ nH.

- Due to radiation issues the generator cannot be placed next to the wire but must be located at least 300 m away (either in a protected area underground or on the surface; only passive elements can be placed next to the beam).
- Given the cable length, transmission line effects must be taken into account. The time delay can be dealt with, but reflections on imperfectly matched connections must be taken care of as they distort the beam shape and introduce noise
- As it will shown in Section 7.2, extremely high timing precisions must be met.
- If one used standard 50Ω cables or tried to match the cable impedance to the BBLR impedance, one would need to switch very high power levels $P = Z \times I^2$. As one is not interested in the power, but the current only, low Ω cables must be used.
- In order to dissipate the heat from the BBLRs, it must be actively cooled. The SPS BBLRs are continuously water-cooled, which might pose a risk in the super-conducting LHC.
- In order to adapt flexibly to modifications of the bunch pattern, the device should be freely programmable.

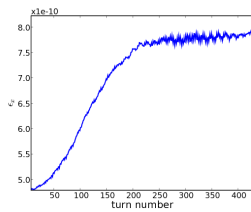


7.2 Noise and emittance growth

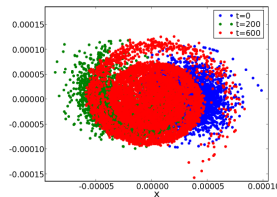
7.2 Noise and emittance growth

In the derivation of the kick due to a DC-wire on the beam (section 3.4.1), it was argued that the linear term $-\text{sign}(q)\frac{\mu_0 I}{2\pi B_d \rho} \frac{x_{wy}}{d^2}$ must be subtracted, as this is in practice done by dipole correctors. This is a valid assumption for a constant/predefined current pattern but it is not in case of random current fluctuations e.g. due to noise. In this case a dipole contribution will remain, which - depending on the frequency of this noise - can cause emittance growth.

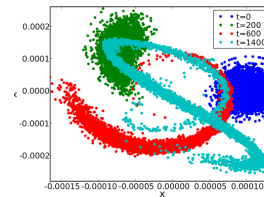
In case of a one-time beam displacement, the amplitude dependent tune spread causes the off-set bunch to filament. Figure 7.2 a shows the bunch emittance in the nominal LHC as a function of the number of turns after a kick, small compared with the beam-size. The bunches are still reasonably well aligned at the IP and the head-on tune spread causes filamentation in about 200 turns. Subfigure b shows the transverse beam distribution for three selected turn numbers. In case of a large kick the bunches do not collide HO at the IP anymore, and the reduced tune spread causes a longer filamentation time (subfigure c).



(a) Bunch emittance as a function of time after a small one-time displacement evolution. In the nominal LHC any small transverse offset filaments within 200 turns (small as compared with the beam size.)



(b) Particle distribution in $x-x'$ -phase space for a small initial offset at different numbers of turns after the offset



(c) Particle distribution in $x-x'$ -phase space for a large initial offset at different numbers of turns after the offset

Figure 7.2: Evolution of the LHC beam after a single kick.

If a transverse feedback is available that corrects this offset before it filaments, the effect of noise can be reduced significantly. While the standard beam-based transverse feedback might not be active at store, a special one could be designed for the BBLR. Namely the current jitter on the wire compensator can be measured with a high precision at turn number N . If one subtracts this error from the applied BBLR signal 3 turns later (=short compared with the filamentation time), the effect can be canceled. The 3-turn delay is chosen as the LHC is designed to run at a tune very close to the $1/3$ integer and a particle returns to almost exactly the same position every

three turns. Simulations proved that this concept is capable to reduce the emittance blow up significantly.

So far the effect of a single, one-time displacement was studied. The effect of continuous noise excitation can be studied in a similar way as the transverse resonant excitation due to multipoles: One needs to relate the frequency spectrum of the noise to the betatron tunes.

In case the noise frequency is an integer multiple of the betatron tune, the contributions will add up coherently. If the frequencies differ such that an averaging takes place faster than the filamentation time, no emittance growth is observed.

Another possible concern is that in case of a linearly ramped BBLR, the synchrotron motion causes particles to sample different time instances of the ramp and they therefore experience an oscillating kick strength. Fortunately the synchrotron tune in LHC is much smaller than the betatron tune. The result is an adiabatic change ([31]) which causes no emittance growth.

Related noise issues were studied in the context of crab cavity studies [32]. Crab Cavities are a type of electromagnetic cavity used to provide an z-dependent transverse deflection allowing to annihilate the effect of a finite crossing angle. Just like in case of the BBLR any crab-cavity rf-phase noise creates a transverse offset at the IP leading to emittance blow up. Figure 7.3 shows the emittance blow up as a function of modulation amplitude for the three experimentally measured sideband frequencies (1 Hz, 1kHz, and 32 KHz) of the KEK crab cavities. Low frequencies lead to very low emittance growth. The LHC betatron tune compares to about 2kHz.

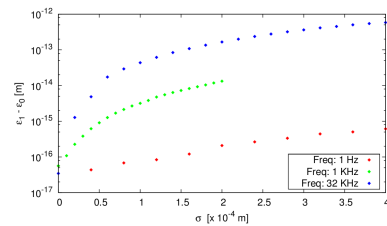
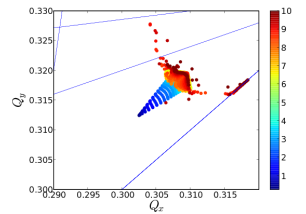


Figure 7.3: Emittance growth due to a periodic offset with different modulation frequencies at two IPs ($\beta^* = 0.25\text{m}$) as a function of modulation amplitude.

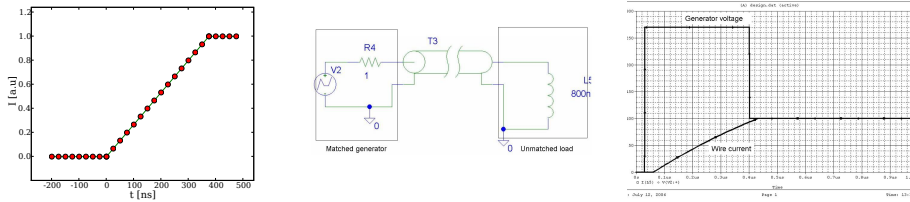
7.3 Pulsed DC-BBLR

Initially the idea was pursued to ramp the current on the BBLR such as to connect two data points in the current-time diagram (Fig 7.1) by straight lines creating linear slopes as illustrated in Figure 7.4 a. Subfigure b sketches the corresponding assembly: A matched power generator, a low ohmic cable and an unmatched BBLR. Low ohmic cabling on the one hand reduces the required power demands drastically and on the other hand implies that the system response to an applied voltage step is dominated by the inductivity of the BBLR. By a suitable choice of the applied voltage level, the characteristic BBLR response $\dot{I} = U/L$ can be used to create a current slope. The ramp



7.3 Pulsed DC-BBLR

shape deviates from a straight line, but small deviations are acceptable as long as they are reproduced on every turn. Once the desired current is reached, the applied voltage is reduced to match the ohmic losses (subfigure c). Reflections on the unmatched BBLR propagate back into the matched power generator where they are absorbed.



(a) DC-BBLR current as a function of time. A DC-BBLR connects the instances when bunches pass the BBLR (markers) by straight lines.

(b) A sketch of the assembly: A matched generator, a low ohmic cabling and the unmatched BBLR

(c) Applied generator voltage and resulting current ramp on the BBLR.

Figure 7.4: Details on the DC-BBLR

7.3.1 Noise issues

In a DC-BBLR the timing error in the turn-on moment of the generator voltage translates linearly into a current amplitude error experienced as noise by the bunches. In order to quantify the required amplitude/timing precision simulations with Gaussian white noise on the BBLRs were performed. As described in section 7.2 the frequency spectrum of the noise is crucial and white noise will only provide a pessimistic estimate. The simulation results in Figure 7.5 show a quadratic dependence of the emittance growth on the noise amplitude. This observation agrees well with theoretical considerations: Starting with a beam of emittance ϵ_0 , one turn later it is given by $\epsilon_1 = \langle (x + \delta x)^2 \rangle / \beta$, where the expectation value is to be taken over all particles). It can be rewritten as

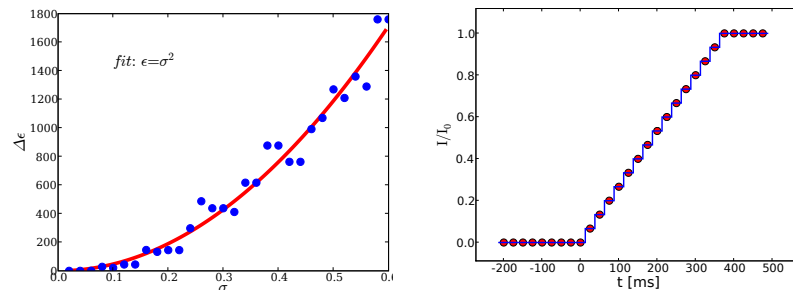
$$\epsilon_1 = \underbrace{\langle x^2 \rangle}_{\epsilon_0} + \underbrace{\langle 2x\Delta x \rangle}_0 + \underbrace{\langle (\Delta x)^2 \rangle}_{\langle \Delta \epsilon \rangle > 0} \quad (7.2)$$

$\langle 2x\Delta x \rangle$ is zero because we assume no correlation between the noise and the unperturbed beam distribution. N turns later, we obtain $\epsilon_N = \epsilon_0 + \sum_{turns} \langle (\Delta x)^2 \rangle$, where the summation over the turns can be interchanged with the computation of the expectation value. The emittance growth is then given by:

$$\Delta \epsilon = N \cdot \sigma^2 \quad (7.3)$$

An emittance growth of $\Delta\epsilon < 10\%$ in 20h is commonly accepted to be tolerable. Such small noise levels are well below the simulation precision but the corresponding tolerance can be extrapolated from the observed scaling. For a pulsed DC BBLR the turn to turn amplitude noise must then be less than 3mA which corresponds to a timing precision of $\Delta t < 0.02$ ns. It turned out that this is beyond the scope of today's high-current switching devices.

At the expense of an even higher current slope, this timing precision can be reduced. If one manages to create a step wise current pattern on the BBLR (Figure 7.5 b), timing jitter is no issue any longer. Each step can be implemented by a separate digital switching unit, which operates faster and more precisely than analog ones.



(a) Simulated emittance growth due to white Gaussian noise on the DC-BBLR in nominal LHC

(b) A step wise approach increases the current slopes but reduces the required timing precision

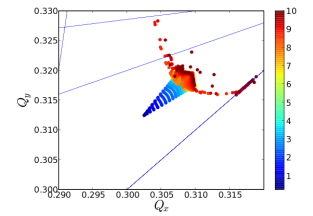
Figure 7.5: Simulations on the effect of noise on a pulsed DC-BBLR (a) and a stepwise approach to reduce the timing precision requirement at the price of an increased current slope (b)

7.4 RF-BBLR

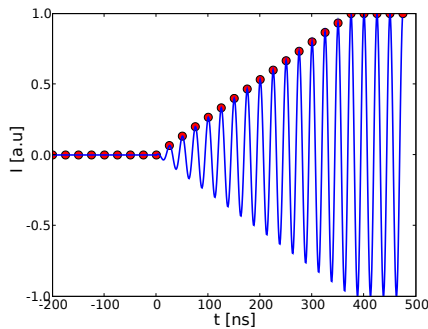
7.4.1 Principle and advantages

An RF-based pulsed BBLR turned out to be the best, technologically feasible solution. As shown in Figure 7.6 the RF-BBLR current follows an amplitude modulated 40 MHz-sine wave (matching the 25ns bunch spacing). In this case the BBLR length is no design parameter anymore, but it represents a $\lambda/4$ resonator at 40 MHz (Figure 7.6 b). The current-slope and the power requirements now depend on the quality of the coupling from the signal generator to the resonator.

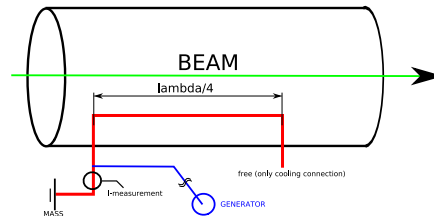
Figure 7.7 shows the various signals involved: A fixed frequency, fixed amplitude sinusoidal signal is mixed with a control signal. The output is connected to the device in the tunnel over a transfer line. In the BBLR a



7.4 RF-BBLR



(a) The RF-BBLR current follows an amplitude modulated 40MHz sinus signal



(b) A RF BBLR represents a $\lambda/4$ resonator

Figure 7.6: Current pattern (a) and schematics of an RF BBLR (b).

resonant build up of the current amplitude occurs, which is described by $I = I_0(1 - e^{-t/\tau})$

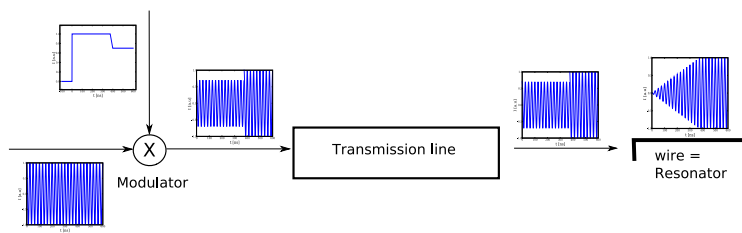


Figure 7.7: Cartoon of signals in various parts of the RF-BBLR system.

The advantages of an RF-BBLR are summarized in the following:

- As it operates as a resonator, the RF-BBLR requires less input power to reach an equivalent strength. Conservatively one can estimate the quality factor Q to be 10, which results in the same factor of reduction in power required from the generator.
- As the electromagnetic field in the RF-BBLR counterpropagates to the beam, the beam samples both, a magnetic and an electric field. This reduces the required current by a factor of 2 and therefore the required power by a factor of 4
- When the beam passes the ends of the RF-BBLR the current amplitude is zero. Therefore any fringe field effects are significantly reduced. As a draw back, this introduces an efficiency reduction due to the transit time factor.

Pulsed BBLR and related noise issues

- As an RF BBLR is based on a resonating structure (Fig. 7.8a) it is very stable in time and should be as reliable as an accelerating RF-cavity
- As it will be shown in section 7.4.2, the sinusoidal current function results in a reduced timing noise sensitivity.
- The RF-BBLR allows the use of a passive circulator in the tunnel close to the beam which dumps reflected waves and keeps them from propagating back into the generator.

All in all, this approach allows to relax the power and precision requirements to a level well within the state-of-the-art of today's RF technology.

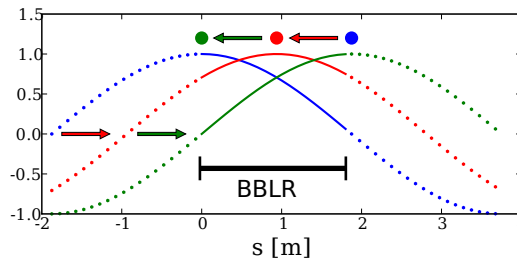


Figure 7.8: The bunch position (dots) and the wave pattern (lines) along the RF-BBLR at three different time instances. As the current vanishes when the bunch passes the ends, fringe field effects are significantly reduced.

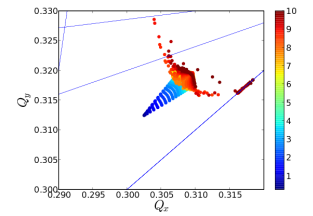
The quality factor Q of a resonant system is defined to be 2π times the ratio of the stored energy divided by the energy dissipated per cycle, evaluated at the resonant frequency. It is a function of material properties and of the coupling strength and defines the achievable power gain and current slope. The external quality factor, Q_{ext} , measures the losses of the external circuit, the unloaded one, Q_0 , that of the resonator and the loaded one, Q_L , that of the whole circuit. When an equal amount of power is dissipated in the external circuit as in the resonator itself, the coupling is said to be critical $Q_{\text{ext}} = Q_0$. An undercritical coupling means that more power is dissipated in the resonator than in the external circuit $Q_{\text{ext}} > Q_0$ and vice versa for overcritical coupling

For the required current slope the quality factor Q must be

$$Q = \frac{\tau\omega}{2} \approx 15\pi \approx 50 \quad (7.4)$$

Assuming critical coupling we therefore need a loaded Q_L of 50 which requires an unloaded Q_0 of 100. The unloaded Q value of a cable resonator is given by

$$Q = \pi/(\alpha\lambda) \quad (7.5)$$



7.4 RF-BBLR

where for a coaxial structure α [N/m] is:

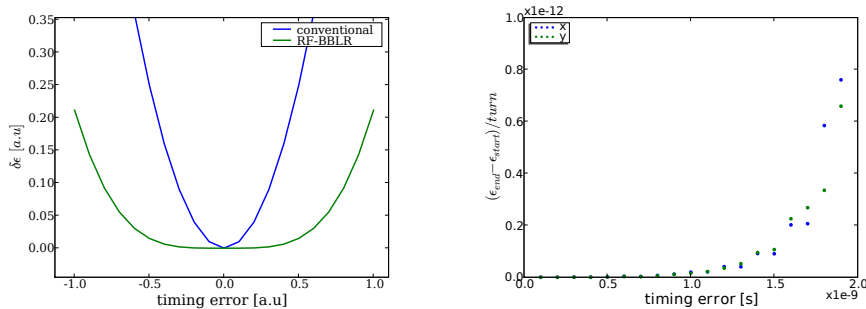
$$\alpha = \frac{\sqrt{\epsilon_r}}{120\pi \ln \frac{D}{d}} \left(\frac{\rho'_i}{d} + \frac{\rho'_o}{D} \right), \quad (7.6)$$

with ρ' the surface attenuation given in Ω/m (o=outer, i=inner) and d the cable diameter in m. For an inner copper rod ($\rho'_i = 2.5 \times 10^{-7} \cdot 1.03\sqrt{40E6} = 0.00163$ [30]) with $d_i = 3$ mm and a beam pipe diameter of $d_a = 5$ cm the unloaded quality factor is $Q_0=771$, which is well above the requirements.

In case of a DC-BBLR, the static magnetic field penetrates the beam pipe and the field pattern is therefore not modified by the surroundings. For the RF-BBLR the electric and magnetic fields are slightly modified by the surrounding beam pipe (proximity effect). Still this is not seen as an issue as a) the effect is very small b) it is possible to use a bigger beam pipe to reduce the effect, c) the fields of the LRBBI are identically modified, and d) the wire shape can be modified to restore a $1/r$ field shape.

7.4.2 Noise

The amplitude precision requirements of an RF-BBLR are identical to the ones of a pulsed DC-BBLR. Due to the sinusoidal current pattern there is no more a linear, but a nonlinear relation to the timing error. At the moment the bunch center passes the BBLR, the derivative of the current with respect to time $\partial I/\partial t$ vanishes. Figure 7.9 a compares the different time-amplitude functions for a pulsed DC-BBLR to the one of an RF-BBLR. Subfigure b shows a simulation reproducing the $(1 - \cos(\delta))^2$ shape ($\delta =$ timing error). The required timing precision is in the order of a few nano-seconds.



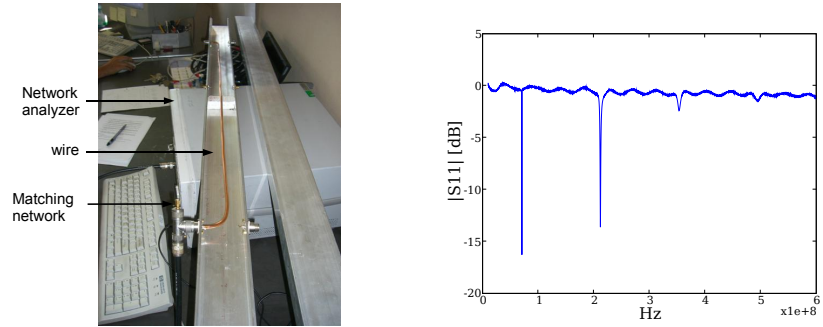
(a) Comparison of amplitude noise due to a timing error in case of RF BBLR and a pulsed DC BBLR

(b) Simulated emittance growth in the horizontal (x) and vertical (y) plane due to a timing error for a RF BBLR

Figure 7.9: Expected and simulated effect of a timing error on a RF-BBLR

7.4.3 Prototype # 1

In order to test the RF-BBLR scheme a first not-to-scale prototype (Fig. 7.10 a) was built and its RF resonator properties were measured. Figure 7.10b shows the measured S11 parameter over a wide frequency range. The



(a) Experimental setup showing the wire and the matching network. (b) Measured S11 parameter revealing the resonant structure

Figure 7.10: Details on the RF-BBLR prototype # 1.

quality factor Q is calculated from: $Q = \omega_0/(\Delta\omega_h)$ where ω_0 is the resonance frequency. $\Delta\omega_h$ is the frequency span between the 3-dB frequency above and below the resonance frequency. As the plot shows the S11 parameter, this corresponds to a signal drop of -3.01dB from the zero line. A loaded quality factor of $Q_L = 252$ is found corresponding to $Q_0 = 504$ in case of critical coupling.

7.4.4 Prototype # 2

Prototype # 2 was built with more realistic dimensions (wire length=177.5cm, Fig. 7.11 a) to obtain the resonance at $f \approx 40$ MHz. An HP-33120A wave form generator is used to generate a sequence of rectangular pulses ($f=25$ kHz. $U=0/1.11$ V max, VDC=-0.6 V, Fig. 7.11 b). A Rhode Schwarz SM300 signal generator provides the required RF-signal ($f=37.4449$ MHz, $U=100$ mV). At the output a -3 dB attenuation damps any incoming waves, which would otherwise pollute the generator and cause signal distortions. The signals are mixed in a “Mini-circuits #15542, Mixer ZFM-2” modulator. The output signal is connected to a T-piece at the BBLR-feeding port. The third, free connection is terminated by a short via a cable with variable length L . Choosing L suitably allows one to change the coupling strength. The oscilloscope at the second BBLR port is coupled weakly capacitively in order not to influence the resonating structure.

7.4 RF-BBLR

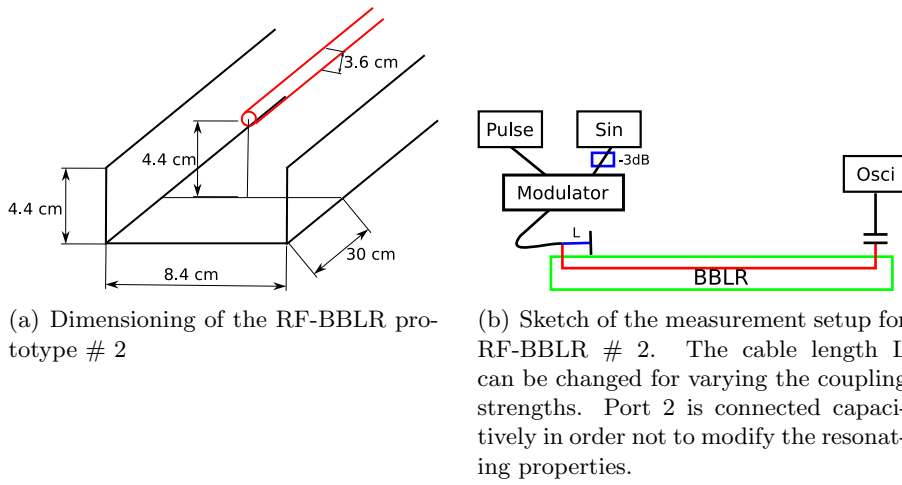
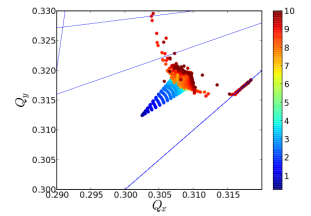


Figure 7.11: Details on the dimensions and on the measurement setup for RF-BBLR prototype # 2. The wire length is 177.5cm

Figure 7.12 shows the measured oscilloscope signal over several periods of the rectangular HP-33120A signal in case of critical coupling. While the desired ramping is reproduced, the ramping time constant is too low and must be adjusted.

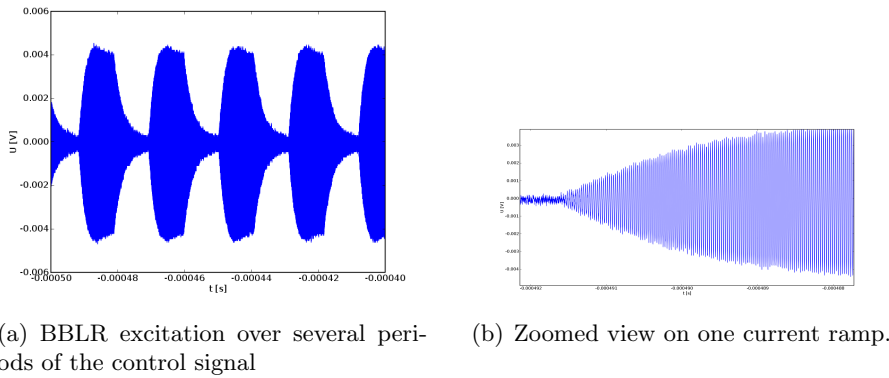
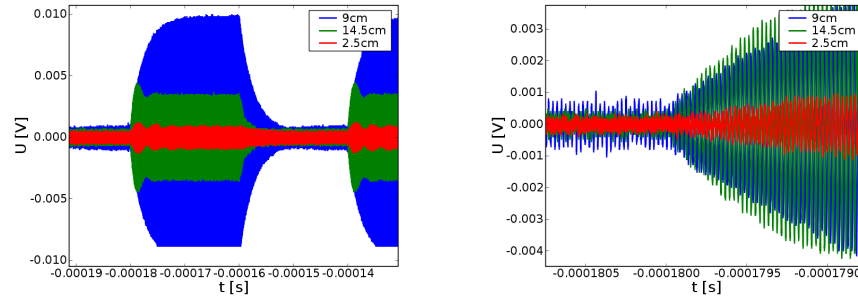


Figure 7.12: Excitation of a critically coupled RF-BBLR. The coupling needs to be adjusted to reach the desired ramp rate

The effect of different lengths L , corresponding to different coupling types, is shown in Figure 7.13 for $L=14.5$ cm, 9 cm and 2.5 cm. The undercritical coupling in case of short L delivers a short rise time at the price of a vanishing resonator gain. With the same power generator signals, overcritical coupling causes a slower rise time with an overshooting. Maximal resonator gain is found for $L=9$ cm. By varying the coupling, one therefore faces a trade off between fast rise times and resonator gain. It is a trade

Pulsed BBLR and related noise issues

off between the power invested during the rise to the power used continuously at flat top. Any overshooting can be suppressed with the help of a more sophisticated control signal generator, that adjusts the control signal accordingly.



(a) An overview shows the various achievable resonator gains

(b) A zoomed view shows the different rise times for the different couplings.

Figure 7.13: Varying the coupling strength provides a trade off between fast rise time and resonator gain.

Once the flat top is reached, the phase relation between the input signal and the BBLR excitation is fixed but during the ramp the phase relation changes as indicated in Figure 7.14 in case of over critical coupling. This needs to be corrected for by a suitable phase adjustment as it is routinely being done in the accelerating RF-cavities. Changing the drive frequency at a given resonator length causes excitation off resonance. Figure 7.15 shows the case of $L=9$ cm for various excitation frequencies.

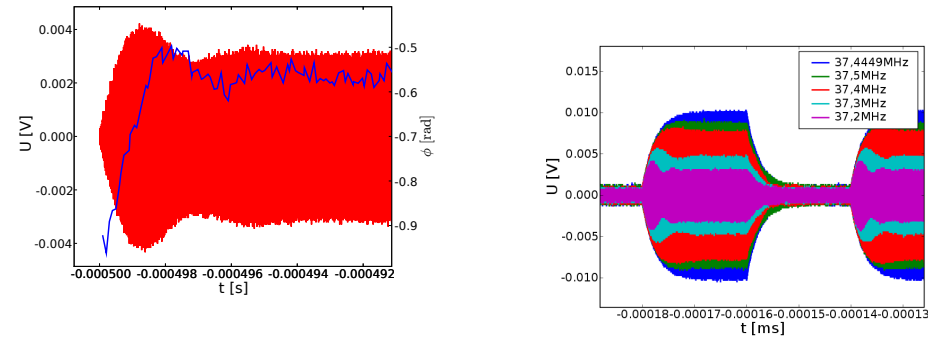


Figure 7.14: Phase relation (blue curve) between the feeding RF and the signal on the RF-BBLR (red curve) in case of overcritical coupling

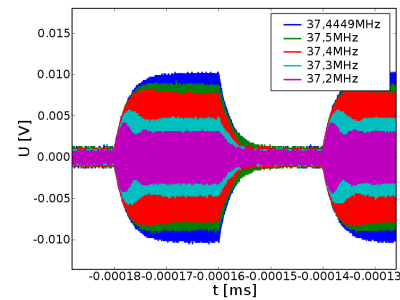
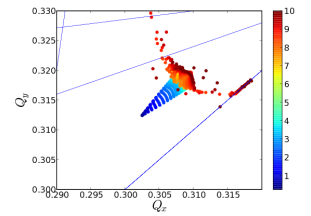


Figure 7.15: Excitation of the RF-BBLR at various drive frequencies off resonance.

A convenient way of characterizing resonant circuits is by measuring the locus of the reflection coefficient S_{11} as a function of the frequency

7.4 RF-BBLR



with help of a network analyzer. In the Smith Chart representation S_{11} describes a circle, whose radius increases with the strength of the coupling to the resonant circuit. Figure 7.16 shows the experimental loci for various coupling lengths. In the same figure the lines $R = X$, $\Im(1/z) = 1$ and $\Im(1/z) = \pm(\Re(1/z) + 1)$ are plotted. The intersection of these lines with the loci (indicated by red dots for the $L=20\text{cm}$ case) allows one to compute the corresponding quality factors [30].

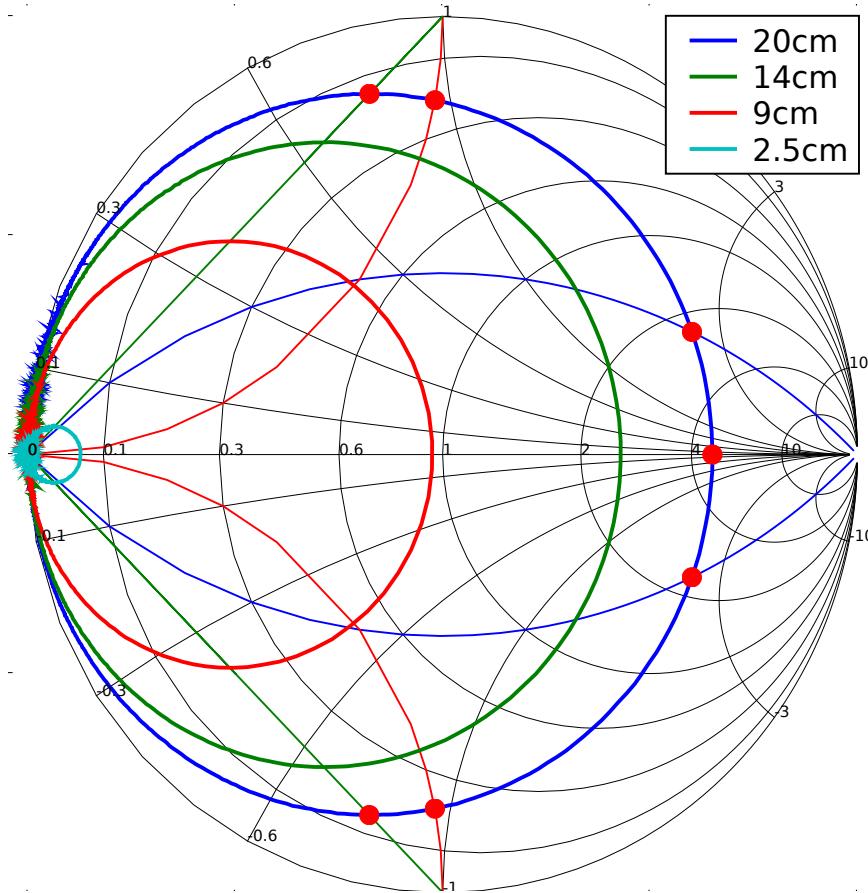


Figure 7.16: Smith chart including the S_{11} loci for various lengths L for $30\text{MHz} < f < 45\text{MHz}$. The intersections with the lines $R = X$, $\Im(1/z) = 1$ and $\Im(1/z) = \pm(\Re(1/z) + 1)$ allows one to compute the various quality factors.

Table 7.1 summarizes the computed quality factors for various lengths L , that fulfill the relation $1/Q_L = 1/Q_0 + 1/Q_{ext}$

Pulsed BBLR and related noise issues

L [cm]	Q_0	Q_L	Q_{ext}
20	428.9	74.7	90.7
14	451	128.3	179.7
9	515.6	263.4	537.2
2.5	688.3	579.6	6183.5

Table 7.1: Quality factors for various coupling lengths L . Critical coupling occurs at approximately $L=9$ cm, where the loaded and the external Q are about identical

In order to damp higher harmonics ($2n+1$), which can also be excited, one can either use a frequency dependent coupling network. Seen from the RF-BBLR, this network must act like a short at 40 MHz but be matched at other frequencies. Alternatively one can use ferrites, which damp increasingly strongly with increasing frequency.

A quality factor of 50 can couple up to 25 bunches and cause coupled bunch instabilities. A feedback system, similar to the one in ordinary RF cavity, can be used to measure the beam induced signal and adjust the generator output such that the sum signal (beam induced + generator) adds up to the design value. Like this the quality factor seen by the beam is reduced while the electrical one remains unchanged.

7.5 RF characterization of the SPS BBLRS

The BBLRs installed in the CERN SPS were characterized with respect to their RF-characteristics. In order to do so, a coaxial cable was installed that links the surface to a serial connection of two BBLR tanks installed in the SPS tunnel (Fig. 7.17a). This setup allows one to measure the beam induced signals on the BBLR during SPS operation. It turned out that one deals with two coupled resonators - the BBLR itself (mismatched to coaxial cable, short in length and thus short period) and the long coaxial cable resonator, which can be influenced by modifying the termination at the surface end.

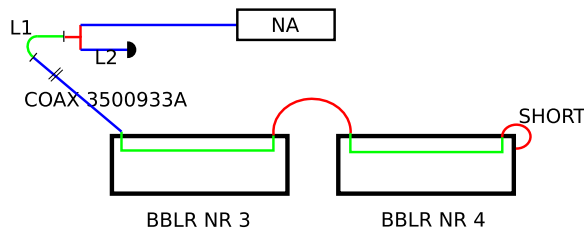
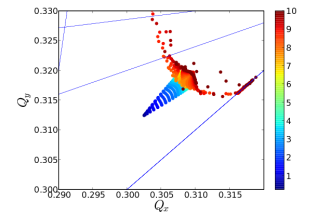
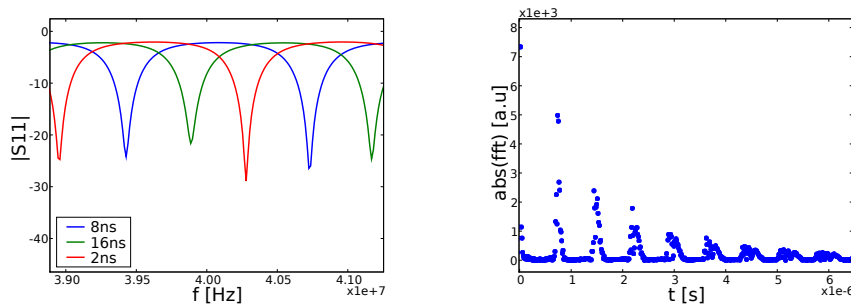


Figure 7.17: Two SPS BBLR tanks connected in a superelectrode like setup to measure the RF-properties of the CERN SPS BBLRs. A cable of varying length $L2$ allows to shift the resonance.



7.5 RF characterization of the SPS BBLRS

At first the BBLRs and the connection network is characterized without circulating beam in the SPS. In order to do that, the top end of the coaxial cable is connected to a T-piece. One of the two ports is terminated by a short over a variable length $L2$, the other one connected to a network analyser. Fig. 7.18 a shows the measured S_{11} parameter of the structure. A suitable choice of $2L$ allows to shift a resonance to $f=40\text{MHz}$. The lowest resonance is found at $f = 1.3\text{MHz}$, which indicates a resonator length identical to the one obtained from the FFT signal. The quality factor is 110 which is sufficient to allow a resonant excitation of the beam by a low-power signal generator.



(a) — S_{11} — as a function of frequency for various resonator length extensions L . For a suitable choice the resonance can be shifted to 40 MHz

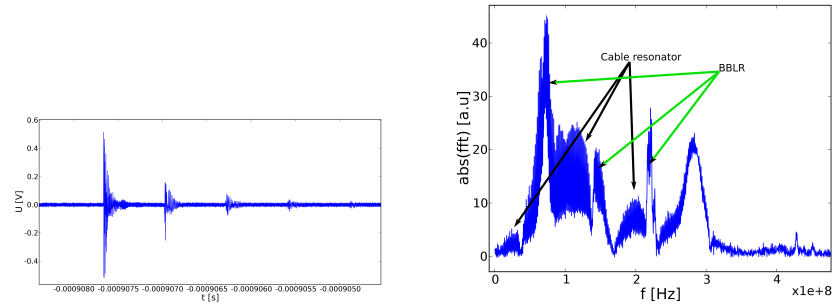
(b) FFT of the spectrum showing the periodic reflections. Due to multiple reflections at the BBLR, the signal broadens.

Figure 7.18: $|S_{11}|$ as a function of frequency (a) and the FFT (b).

Finally the beam-induced signal on the BBLR is measured. As there is only a BBLR on one side of the beam, only information on the longitudinal excitation can be obtained. Figure 7.19 shows the measured signal from a single bunch passing. Subfigure a shows the signal in the time domain where several reflections are identified. The spacing corresponds to the time it takes the signal to travel twice the coaxial cable length. The increasing width of one pulse is a result of multiple reflections in the BBLR resonator. Subfigure b shows the Fourier transformed signal where the contributions from the BBLR and the long coaxial cable are indicated. As an attempt to shift the distinct minimum at 40MHz by extending the resonator on the surface failed, it is concluded that this minimum is caused by the BBLR resonator.

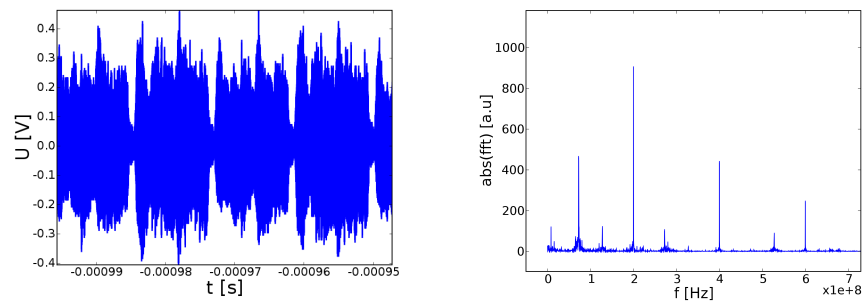
In another case the signal induced by a bunch train with 25ns spacing was measured (Fig. 7.20). As expected from the previous measurement, no spectral component at 40 MHz is found.

Pulsed BBLR and related noise issues



(a) Induced signal as a function of time (b) The Fourier transformed signal shows a distinct minimum at 40 MHz.

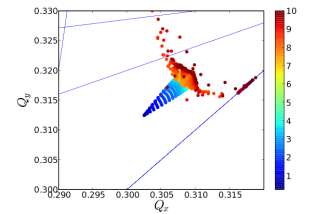
Figure 7.19: Signal due to a single bunch passing measured at the surface



(a) In the time domain, the separate bunch trains are clearly seen.

(b) Due to the minimum at 40 MHz in the BBLR, no signal is measured at this frequency for a 25 ns spaced bunch train.

Figure 7.20: Signal caused by a bunch train with 25 ns spacing in time (a) and frequency domain (b).



7.6 Measuring phase noise

7.6 Measuring phase noise

Before installation of an RF-BBLR in LHC, it must be tested for its timing jitter in the laboratory. Measuring these tight timing tolerances in the time domain is almost impossible and one must perform a phase noise measurement instead. While jitter is a time domain measure of the timing accuracy of the oscillator period, phase noise is a frequency-domain view of the noise spectrum around the oscillator signal at f_0 . For a given frequency offset Δf , the latter is given by the ratio of the power in a 1-Hz bandwidth around the offset frequency $f + \Delta f \pm 1Hz$ to the total power of the carrier. In order to measure these sidebands accurately the main carrier must be suppressed.

In case of the RF-BBLR the, phasenoise at an offset of 11kHz (=LHC revolution period) is of importance. To measure this, the signal from the signal generator is split in two. While one part is connected straight to the LO input of a mixer, the other one is delayed by exactly 1 LHC revolution period before going to the mixer's RF input. The signal at the output of the mixer is the autocorrelation between the two signals evaluated at the delay time. The jitter is the Fourier transformed output.

Usage of an optical fiber for the delay would introduce too much jitter from the electro-optical converters and a lumped LC-delay line would require too many elements (there should be one LC-section for each length of $\lambda/10$). Quartz filters with sufficient group delay at 40 MHz or surface acoustic wave devices seem promising.

Alternative measures

The BBLR is not the only measure for counteracting the impact of beam-beam interactions which is currently under study. In the following three other beam-beam compensation schemes are briefly discussed.

8.1 Electron lens

An electron lens (EL) consists of an electron beam that counterpropagates the stored beam over a length of a few meters. Two such devices are installed in the proton-antiproton collider Tevatron (in this case commonly referred to as “Tevatron Electron Lens”, TEL). The 2m long TEL provides up to 6A electron current each with an rms beam radius about 0.66 mm. The maximum kinetic energy of the electrons is 15 keV.

An EL can be used like a BBLR for compensation of LRBBI. While being technically much more complicated and possibly more prone to noise, it also allows compensation of LRBBI encounters with low beam-beam separation [28]. Alternatively the electron beam can be aligned with the stored beam and a head-on tune spread compensation can be attempted [21]. The TELs were primarily installed for this second purpose but they are not yet used in daily operation. The head-on beam-beam interaction is of special concern in the LHC phase 2 upgrade scheme “LPA”, where intense bunches of 5×10^{11} protons each are collided. Instead of the currently proposed approach (longitudinal flat beams) to reduce the head-on effect, an EL could be used as an attractive alternative. Finally an electron lens can be used as a fast switching quadrupole to mitigate the tune and orbit variations of PACMAN bunches. The TELs are actually employed in the mode of operation at the Tevatron, where the tune compensation of individual PACMAN bunches and a resulting beam lifetime improvement were successfully demonstrated.

Figure 8.1a) shows how much the tune footprint in nominal LHC could be reduced by the combined effect of a BBLR and an EL. Like for the RF-BBLRs, one of the main concerns is noise causing emittance growth [33]. Subfigure b shows the emittance growth due to random transverse positioning errors of the electron beam. The fit function allows one to extrapolate a $\approx 1\mu m$ precision requirement in order to keep the emittance growth over

Alternative measures

20 hours below 10%.

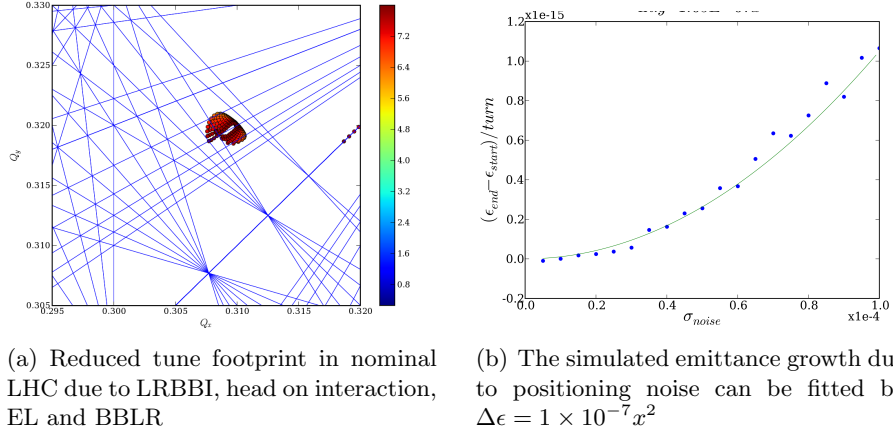


Figure 8.1: BBTrack simulations on the effect of an electron lens for head-on beam-beam compensation in nominal LHC

8.2 Crab cavities

Crab Cavities are a type of electromagnetic cavity used to provide a z-dependent transverse deflection allowing to avoid the geometric luminosity loss due to a finite crossing angle (Fig. 8.2). Such a device is currently in operation in the electron/positron collider KEKB but it has never been tested in a hadron machine. The tilt can either be only local (with crab cavities at both sides of the IP) or global (the bunch is tilted all round the accelerator).

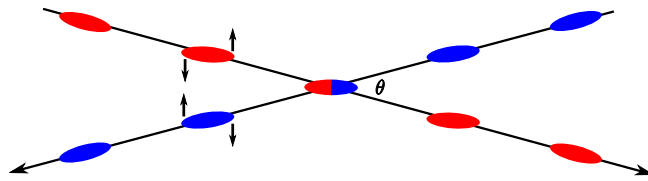
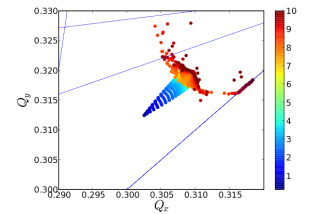


Figure 8.2: Crab cavity operation principle

In BBTrack the effect on a particle passing the device is given by

$$\dot{p}_x = -\frac{\partial H_{crab}}{\partial x} = -\frac{q\hat{V}}{p_s} \sin\left(\Phi_s + \omega\frac{s}{c}\right) \quad (8.1)$$

$$\dot{p}_s = -\frac{\partial H_{crab}}{\partial s} = -\frac{q\hat{V}}{p_s} \cos\left(\Phi_s + \omega\frac{s}{c}\right) \left(\frac{\omega}{c}\right) \cdot x \quad (8.2)$$



8.3 Flat beam option

The chosen frequency defines the required size (cost, space requirement) of the device but also the deviation from the desired linear $s - \Delta x$ relation.

Once again, one of the major concerns is noise causing emittance growth as indicated in Figure 7.3 showing the simulated emittance growth caused by a noisy crab cavity with a frequency spectrum as measured in actual crab cavities at KEKB [32]

8.3 Flat beam option

Another interesting approach to reduce the LRBBI effect while not losing much geometric luminosity is the application of flat beams at the IP ($\beta_x^* \neq \beta_y^*$). Choosing the larger beta function in the crossing plane improves the geometric overlap of the two beams and it causes a smaller beam size at the location of the LRBBI encounter and thus an increased normalized beam-beam separation. Following earlier proposals for a 50 TeV Hadron Collider [34], this was proposed for an LHC upgrade in [35] and then shown to be possible also with the nominal LHC triplet design by adjusting quadrupoles upstream of the triplets converting the present horizontal/vertical into a V/H crossing scheme [36].

Summary

9.1 Summary

The long-range beam-beam interaction will be the ultimate performance limitation of the CERN LHC. The effect itself and one approach to overcome this limitation – the wire compensation (BBLR) – were studied in experiment and simulation.

In course of the thesis the versatile, weak-strong particle tracking code “BBTrack” was developed and employed. Compared to other existing tracking codes it a) features a large variety of initial particle distributions, b) accepts two different accelerator descriptions (thin lens, transfer matrix or a combination of the two) c) is designed to be easily extensible d) contains a variety of special elements like the BBLR, an electron lens, a feedback system or a crab cavity. e) allows time/turn dependent modifications of the element’s parameters (e.g. for noise studies). f) features various different stability criteria.

A series of experiments at the CERN SPS and RHIC at BNL were planned, performed and analyzed in order to get an experimental understanding of the effect of the long-range beam-beam interaction (LRBBI) and the wire compensator (BBLR) on the beam. Furthermore the obtained results allowed to benchmark the simulation code BBTrack.

The BBLRs in the CERN SPS were used to mimic LRBBI of varying strength with different normalized beam-wire separations at 26, 37 and 55 GeV proton beam energies and chromaticity. While the fast repetition rate of the CERN SPS allowed to scan a large parameter space within a reasonable time, the superior beam lifetime of RHIC was used to perform some special LRBBI and BBLR studies with higher precision. Apart from some few exceptions the simulations match the experimental data quite well.

With these experimental results in mind, the LRBBI-performance of the LHC and the compensation efficiency were studied. This was done for the nominal LHC optics design as well as for the various LHC phase one and two upgrade scenarios. For the LHC phase one upgrade the so called low β max optics was found to be preferable. It is shown that a wire compensator enhances its beam-beam performance significantly to a level well above the one of the nominal uncompensated LHC design. While

Summary

the upgrade phase 2 option “dipole zero“ is not compatible with a wire compensator and faces some serious beam-beam issues, the ”large Piwinski angle“ scheme relies on it and a compensated performance is found which is approximately equivalent to the one of the uncompensated nominal LHC.

While an intermediate DC current level on the BBLR can be set that enhances the performance of all bunches, nominal as well as PACMAN bunches, a pulsed BBLR can be adapted and compensate each bunch independently. The operational jitter tolerances of such a pulsed BBLR device were identified and it was found that a linearly ramping pulsed DC-BBLR using nowadays state-of-the-art technology cannot fulfill the tight tolerances. Therefore an alternative concept based on RF technology was developed. The idea behind this approach is to use the BBLR as a resonator allowing for a low power consumption and enhanced timing stability. A prototype was built and successfully characterized.

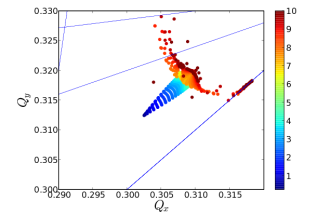
9.2 Zusammenfassung

Wegen der weitreichenden Strahl-Strahl Interaktion (long-range beam beam interaction, LRBBI), werden der Leistungsfähigkeit des CERN LHC Grenzen gesetzt sein. Dieser Effekt und eine Möglichkeit diese Limitation zu überwinden – die Drahtkompensation (BBLR) – wurden in Experiment und Simulation studiert.

Ein Teil der Arbeit war die Entwicklung und Anwendung des vielseitigen Simulationsprogramm ”BBTrack“. Im Vergleich zu anderen tracking-codes bietet es einige Vorteile:

- Es erlaubt eine grosse Anzahl an unterschiedlichen Anfangsverteilungen zu simulieren.
- Es akzeptiert zwei unterschiedliche Beschleunigerbeschreibungen (”dünne Linsen“, Transfermatrizen) und auch deren Kombination.
- Auf Grund seines modularen Aufbaus ist es leicht erweiterbar.
- Es enthält eine Reihe spezieller Elemente wie den Drahtkompensator, eine Elektronenlinse, ein Feedbacksystem und crab cavities.
- Es erlaubt zeitabhängige Modifikationen der Elementparameter, was z.b. für Rauschuntersuchungen nützlich ist.
- Es bietet unterschiedliche Stabilitätskriterien.

Eine Reihe von Experimenten am CERN SPS und RHIC am Brookhaven National Lab (BNL), New York, wurden geplant, durchgeführt und ausgewertet, um experimentelle Erkenntnisse über den Effekt der LRBBI



9.3 Acknowledgments

oder der BBLR auf den Strahl zu gewinnen und die Messergebnisse mit Simulationsergebnissen zu vergleichen.

Die im CERN SPS installierten BBLRs wurden verwendet, um den Effekt von LRBBIs nachzuahmen. Während die hohe Repetitionsrate des CERN SPS es erlaubte, einen großen Parameterraum (variabler Stärke, unterschiedliche normierten Draht-Strahl Abständen, 26 & 37 und 55 GeV, verschiedenen Chromatizitäten) innerhalb kurzer Zeit zu sampeln, wurde die überlegene "beam lifetime" des RHIC genutzt um einzelne LRBBI und BBLR Studien mit höherer Präzision durchzuführen. Abgesehen von einigen wenigen Ausnahmen stimmten die Simulationen mit den experimentellen Daten überein.

Aufbauend auf diesen experimentellen Studien wurde die LRBBI Performanz (=Stärke der und Resistenz gegenüber den negativen Effkten der LRBBI) und die Effektivität der Drahtkompensation im CERN LHC in Simulationen studiert. Diese Untersuchungen wurden sowohl für die nominelle LHC Optik als auch für die vorgeschlagenen, unterschiedlichen LHC upgrade Szenarios durchgeführt (Phase 1 und 2). Für die LHC Upgrade Phase 1 wurde die sogenannte "low-beta-max"-Optik als die beste Wahl identifiziert. Es wurde gezeigt, dass ein BBLR die LRBBI Performanz über das Niveau der nominal, unkompensierten Opik heben kann. Während die Upgrade Phase 2 Option "dipole zero" nicht mit dem Kompensator kompatibel ist und gravierende LRBBI Probleme hat, beruht deren Alternative – das "large piwinski angle" Szenario – auf dem Kompensator, der eine LRBBI Performanz aquivalent zum unkompensierten nominalen LHC ermöglicht.

Während auch ein mittleres BBLR-Gleichstromniveau sowohl die Performanz von normalen als auch von PACMAN-bunchen verbessert, kann eine gepulste BBLR angepasst werden und daher jeden bunch individuell optimieren. Die Jittertoleranz einer solchen gepulsten Einheit wurde bestimmt und es wurde erkannt, dass eine linear interpolierende BBLR basierend auf state-of-the-art Technologie diese Anforderung nicht erfüllen kann. Daher wurde ein alternatives Konzept entwickelt, das auf Hochfrequenztechnologie basiert. Die zu Grunde liegende Idee ist, die BBLR als Resonator zu betreiben und so eine erhöhte Timingstabilität bei gleichzeitig reduzierter Leistungsaufnahme zu erreichen. Ein solcher Prototyp wurde konstruiert und erfolgreich getestet.

9.3 Acknowledgments

Firstly I want to thank my parents who nourished my interest in science and enabled me to go to CERN. Together with my siblings they provided a constant encouragement and kept me grounded all the time.

I was lucky to find support from two great supervisors: Dr. F. Zimmermann from CERN proofed to be an endless source of ideas and a role model

Summary

in his fascination for the topic. He allowed me to profit from his large network of collaborations and enabled me to visit a large number of other Labs and to participate in various workshops and conferences. Prof. H. Aiginger and Dr. Poljanc from the Atominstitut der Oesterreichischen Universitaeten (Vienna University of Technology) supported me during the whole thesis in an exceptional way and especially encouraged me in the harder times. I want to thank Dr. Benedikt for his encouragement during the work.

Dr. J. Pasternak, the first of my two office mates, showed a great patience when explaining me the very basics of accelerator physic, but became a good friend. Despite his own different work background Dr. T.K. Meinschad, my second office mate, was a great discussion partner. He became a good friend and made the time in the office an enjoyable one.

I want to thank T. Kroyer and F. Caspers for the great collaboration on the RF-BBLR. I want to acknowledge the work of the RHIC BBLR team. J. Wenninger, R. Calaga and R. Tomas helped greatly during the execution of the SPS BBLR MDS.

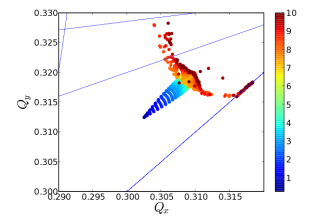
During my stay there I had the chance to come to know many interesting people. Amongst them I want to especially thank S. Bonacini, A. Koschik, T. Kroyer, R. de Maria and M. Mücke who helped me in endless discussions.

Bibliography

- [1] R. Willeken, “Methods of beam optics,” *Desy notes 88-114*, 1987.
- [2] A. Chao, “Lecture notes on topics in accelerator physics,”
- [3] E. Forest, *Beam dynamics - a new attitude and framework*. Harwood academic publishers, 1998.
- [4] *Frequency map analysis and particle accelerators*, 2003.
- [5] U. Dorda, “BBTrack - A weak-strong long-range beam beam interaction simulation code.”, <http://ab-abp-bbtrack.web.cern.ch/ab-abp-bbtrack>.
- [6] F. Z. M.P. Zorzano-Mier and, “Simulations of coherent beam-beam modes at the Large Hadron Collider,” *Phys. Rev. Spec. Top. Accel. Beams*, vol. 3, no. 4, 2000.
- [7] A. Chao, *Physics of collective beam instabilities in high energy accelerators*. New York: Wiley, 1993.
- [8] M. Furman, “Compact complex expressions for the electric field of 2-D elliptical charge distributions,” Tech. Rep. CBP-41. LBL-34682. PEP-II-AP-93-34, Lawrence Berkeley Nat. Lab., Sep 1993.
- [9] M. Bassetti and G. Erskine, “Closed expression for the electrical field of a two-dimensional Gaussian charge,” Tech. Rep. CERN-ISR-TH-80-06, CERN, Geneva, 1980.
- [10] D. Sagan, “The dynamic beta effect in CESR,” *16th Biennial Particle Accelerator Conference, Dallas*, 1995.
- [11] K.Hirata, H. Moshhammer, and F. Ruggiero, “A symplectic beam beam interaction with energy change,” *Part. Accel.*, vol. 40, pp. 205–228, 1993.
- [12] K. Hirata, “Who is afraid of a crossing angle?,” p. 4 p, Jul 1994.
- [13] K. Cornelis, W. Herr, and M. Meddahi, “Proton antiproton collisions at a finite crossing angle in the SPS,” May 1991.

BIBLIOGRAPHY

- [14] D. Neuffer and S. Peggs, “Beam-beam tune shifts and spreads in the SSC - head on, long range, and PACMAN conditions,” Tech. Rep. SSC-63, SSC, Berkeley, CA, Apr 1986.
- [15] W. Herr, “Features and implications of different LHC crossing schemes,” Tech. Rep. CERN-LHC-Project-Report-628, CERN, Geneva, Feb 2003.
- [16] W. Herr, “Consequences of periodicity and symmetry for the beam-beam effects in the LHC,” Tech. Rep. LHC-Project-Report-49, CERN, Geneva, Aug 1996.
- [17] F. Zimmermann, “Beam-beam compensation schemes,” in *CARE-HHH-APD Workshop on Beam Dynamics in Future Hadron Colliders and Rapidly Cycling High-Intensity Synchrotrons*, 2005.
- [18] J. L. Duff, M. Level, P. Marin, E. Sommer, and H. Zyngier, “Space charge compensation with DCI,” Tech. Rep. LAL-RT-80-07, Paris 11. Lab. Accel. Lineaire, Orsay, Jul 1980.
- [19] Y. Derbenev, “The collective instability of the compensated colliding beams,” Tech. Rep. IYAF-72-70, Akad. Nauk Novosibirsk. Inst. Yarn. Fiz., Novosibirsk, Oct 1972.
- [20] E. Keil and G. Leroy, “Effects of a non-linear lens on the stored proton beam in the ISR,” *IEEE Trans. Nucl. Sci.*, vol. 22, pp. 1370–3. 4 p, Mar 1975.
- [21] V. Shiltsev, Y. Alexahin, V. Kamerdzhev, G. Kuznetsov, X. Zhang, and K. Bishofberger, “Experimental demonstration of compensation of beam-beam effects by electron lenses,” tech. rep.
- [22] J. Koutchouk, “Principle of a correction of the long-range beam-beam effect in LHC using electromagnetic lenses,” Tech. Rep. LHC-PROJECT-NOTE-223, CERN, Geneva, Mar 2000.
- [23] F. Zimmermann, “Scaling of diffusive aperture with wire current.” jul 2003.
- [24] W. Herr, “Consequences of phase advance differences between IPs on beam-beam effects.” CERN, LCU seminar, mar 2007.
- [25] R. de Maria, “Layout design for final focus systems and applications for the LHC interaction region upgrade,” Tech. Rep. LHC-PROJECT-Report-1051, CERN, Geneva, 2007.
- [26] J. Koutchouk, L. Rossi, and E. Todesco, “A Solution for Phase-one Upgrade of the LHC Low-beta Quadrupoles Based on Nb-Ti,” Tech. Rep. LHC-PROJECT-Report-1000, CERN, Geneva, Apr 2007.



BIBLIOGRAPHY

- [27] J. Koutchouk and G. Sterbini, “An early beam separation scheme for the LHC luminosity upgrade,” Aug 2006.
- [28] F. Zimmermann, P. Lebrun, T. Sen, V. Shiltsev, and X. Zhang, “Using the Tevatron Electron Lens (TEL) as a wire and other TEL studies at FNAL,” Tech. Rep. AB-Note-2004-041, CERN, Geneva, May 2004.
- [29] O. Bruening, P. Collier, P. Lebrun, S. Myers, R. Ostojic, J. Poole, and P. Proudlock, *LHC Design Report*. Geneva: CERN, 2004.
- [30] F. H.Meinke, *Taschenbuch der Hochfrequenztechnik*. Springer Verlag, 3rd. ed., 1968.
- [31] Landau and Lifshitz, *Mechanics*, vol. 1. Butterworth-Heinenann, 3rd ed., 2000.
- [32] K. Akai, R. Calaga, U. Dorda, K. Ohmi, K. Oide, R. Tomas, and F. Zimmermann, “Small angle crab compensation for LHC IR upgrade,” Tech. Rep. CERN-LHC-PROJECT-Report-1042, 2007.
- [33] U. Dorda, W. Fischer, V. Shiltsev, and F. Zimmermann, “LHC beam-beam compensation using wires and electron lenses,” Tech. Rep. LHC-PROJECT-Report-1023, 2007.
- [34] S. Peggs, F. Pilat, and M. Syphers, “Flat Beams in a 50 TeV hadron collider,” no. PAC97, 1998.
- [35] T. Sen, J. Johnstone, N. Mokhov, W. Fischer, R. Gupta, and J. Qiang, “US-LARP progress on LHC IR upgrades,” no. CERN Yellow report, 2006-08.
- [36] S. Fartoukh, “Prospective for flat beam optics.” LHC MAC no. 19, jun 2006.

Curriculum Vitae

Dipl. Dipl. Ing Ulrich Dorda

Personal Information

Name	Ulrich Dorda
Address	Czartoryskig. 51, 1180 Vienna, Austria
Telephone	+43 1 479 53 62
Email	ulrich@dorda.net
Date of Birth	10. Mai 1978
Citizenship	Austria
Marital status	single
Military service	fulfilled



Education

04.2005 - now	Doctoral studies at CERN/Technical University of Vienna, Austria. Topic: "Compensation of long-range beam-beam interaction at the CERN LHC", scheduled defense: June 2008.
10.2000 - 04.2005	Study of Technical Physics at the Technical University of Vienna, Austria. Specialization in solid state physics. Graduation with honours. Diploma thesis topic "Characterization and Simulation of non-volatile charge-trapping memories"
09.1997 - 06.2003	Study of Electrical Engineering at the Technical University of Vienna, Austria. Specialization in telecommunications. Graduation with honours. Diploma thesis topic "A time domain description of atomic excitation and relaxation processes"
09.1988 - 05.1996	Grammar school; BG 19, Gymnasiumstrasse, Vienna (emphasis on classical studies),

Work experience

04.2005 - 04.2008	PhD student at CERN, Geneva. Working on accelerator beam dynamics (long-range beam-beam interaction) including development and application of simulation software and performing accelerator experiments.
05.2004 - 12.2004	Diploma thesis at Infineon Technologies, Munich. Characterization and simulation of Flash memory cells.
07.2003 - 09.2003	Trainee at CERN, Geneva
07.2000	Trainee at the mobilcom Austria, Vienna (mobile phone company)

Skills and Qualifications:

Languages	German: Mother-tongue, English: fluent, French: basic
Computing	Linux, Windows, Office, Latex, MAD-X
Programming	Python, Fortran, VBA, Matlab, Sage
Driving licence	passenger car

Interests

Sport	Touring skiing, skiing, mountaineering, basketball
Other	Travelling, Music